Characterizing cellular heterogeneity of colonic neoplasia

By

Cherie' Rose Scurrah

Dissertation

Submitted to the Faculty of the

Graduate School of Vanderbilt University

in partial fulfillment of the requirements

for the degree of

DOCTOR OF PHILOSOPHY

in

Cell and Developmental Biology

May 14, 2021

Nashville, Tennessee

Approved:

Christopher Wright, D. Phill.

James Goldenring, Ph.D., MD

Keith Wilson, MD

Andrea-Page McCaw, Ph.D.

Ken Lau, Ph.D.

To my parents Jeffrey Steven and Kimberly Ann Scurrah.

Mom, your strength is unparalleled.

Dad, you are the reason behind everything I am and do.

With you behind me, we will always come in "clutch".

ACKNOWLEDGMENTS

I may be the one getting the PhD, but to do this it takes a village. To the people who doubted me, the ones that encouraged me, and the individuals who had a hand in this work, I thank you. Without you, this would not be possible.

I first need to thank my mentor, Dr. Ken Lau. I could not ask for a better graduate school mentor. From the good days and bad, I never once second-guessed my choice for a mentor. From the bottom of the heart, thank you for it all. I would like to thank my committee members: my chair Dr. Christopher Wright, Dr. James Goldenring, Dr. Keith Wilson, and Dr. Andrea-Page McCaw. To my chair Dr. Wright, I am grateful for your guidance and for always answering my calls. To Dr.'s Goldenring, Wilson, and Page-McCaw, thank you for providing me support, feedback, and perspectives to make me a better scientist. From one-on-one meetings to group meetings, each of you wanted me to succeed, and for that, I am grateful.

To the Lau Lab, past and present, there is not enough space to thank each of you, but your feedback and contribution to my graduate work does not go unnoticed. I appreciate you all; thank you. I do need to thank the "OGs" of the Lau Lab: Sun Wook, Chuck Herring, Joey Simmons, and Amrita Banerjee. You four were the first ones to join the Lau Lab, and I am grateful for you showing me the way and laying the foundation that this lab was built on. A special thanks to Joey Simmons, the backbone of the lab. Thank you for being my first mentor in the lab and showing me the ropes from day 1. Amrita Banerjee, thank you for being the role model I needed in the lab to excel in science, but I am also appreciative for our friendship. Paige Vega, thank you for always coming in clutch, but especially this last year when my life got turned upside down. To the many undergraduates and high school students I mentored over the years, thank you for teaching me while I was teaching you.

I am also grateful for the collaborative atmosphere that Vanderbilt provides. To the Coffey, Goldenring, Goettel, and Choi labs, thank you for your advice, encouragement, and guidance throughout my graduate training. A special shout out to Nick Markham from the Coffey lab for collaborating closely on my tumor models. I am fortunate to have been a part of the Cell and Developmental Biology Department, the Epithelial Biology Center, and the Initiative for Maximizing Student Diversity these past years. The individuals apart of these groups; thank you for your guidance and support. I also want to thank my writing group that virtually met almost every week through 2020, Cait Kirby, Schyler Chambers, Ky'Era Actkins, and Megan Minarich.

I want to acknowledge the funding sources that have supported my graduate training: Initiative for Maximizing Student Diversity (IMSD) Grant (5R25GM062459), Vanderbilt Institute for Clinical and Translational Research Grant (VR14586), Molecular Microbial Pathogenesis Training Grant (5T32AI007281), and R01 Diversity Supplemental (R01 DK103831-02S1). Additionally, the shared resources from the Vanderbilt DDRC, Flow Cytometry Core, TPSR, and DAC were essential to this work. Finally, over the years, I have been blessed with teachers that without their influence, I may have never pursued

a Ph.D. Dr. Wu at Fullerton College; thank you for sparking my interest in research and allowing me my first research opportunity. Mrs. Hart and Mrs. Torres, teachers at my elementary school, The Intensive Learning Center, thank you for instilling study habits that set me up for success throughout my schooling. Your influence at such a young age was vital.

Outside of my academic endeavors, I am blessed to have the most wonderful friends and family. To the Tuesday lunch crew, Maria Agostini, Karin Bosin, and Susan Qualls thank you for serving as a sounding board. To my lifelong friends in California and the new ones I have made in Tennessee, thank you for the support and memories, the quick get-a-ways, the holiday dinners, and celebrations. To my mother and father-in-law, Frank and Juanita Vallejo, thank you for helping us move to Tennessee to start this long journey and for everything you have done for your son and me in the past, present, and future. To my other half, Frank Vallejo, Jr., your support, advice, love, and ability to always keep me centered are instrumental to my success here. Thank you for being my rock through this journey and I am excited to see where life takes us next. To my sister Shannon Lee and my brother-in-law Andrew Merritt, thank you for your continued support.

None of this would have been possible without my parent's constant love and support. Life is hard. Life away from mom and dad is even harder. Momma, Kimberly Ann Salas Scurrah, thank you for picking up the phone nearly every day on my way home to chat. Thank you for your words of wisdom and your unconditional love. This last year has been one heck of a chapter in the book of the Scurrah’s, but despite it all, you continue to fight

with grace and pose. Momma, you are the strongest woman I know. Thank you for being an inspiration to me.

Lastly, to my daddy, Jeffrey Steven Scurrah. As I was writing my thesis, you went to be with the Lord, but I already had my first acknowledgments draft. That first draft is italicized. *I seriously would not be here without you. I am forever grateful for the dedication, drive, and perseverance you instilled in me from such a young age. From math and spelling flashcards on our Lakewood house's living room steps to the countless hours spent on the soccer field and exposing me to the vast unknown nature has to offer-the fishing, hiking, camping, and everything in between. It was you that lit that spark of curiosity that turned into a burning passion to explore how this world works. Without your guidance and love, this absolutely would not have been possible.* I know you are proud, but I will never stop striving to make a difference in this world in your name.

TABLE OF CONTENTS

LIST OF FIGURES

LIST OF TABLES

Table Page

PREFACE

This dissertation is structured into six different chapters as outlined in the table of contents but centered around the single-cell analysis of colorectal cancer. Chapter I provides relevant background knowledge on colonic epithelial and immuno-biology and their roles in homeostasis and cancer. Chapter II provides background information on techniques used throughout this work. Chapters III-IV are recreated from published literature, denoted by the citations at the beginning of each chapter. Briefly, they touch on how we have developed and applied technologies (DISSECT) to analyze colonic epithelial tissue on the single-cell level in both humans and mice, providing a better understanding for more rare cell populations. Chapter V is adapted from a manuscript in preparation when this dissertation was submitted and touches on how non-stem and stem cell-driven colon tumors retain characteristics of the tumor cell-of-origin. Lastly, Chapter VI provides a summary and future directions directly related to chapter V. Figures, tables, and corresponding legends from chapters III-IV are recreated from the relevant publications stated in the beginning of respective chapters. Figures, tables, and legends in chapter I, II, and VI are original. Figures in chapters I and II were created by utilizing BioRender.com.

Chapter I

BACKGROUND

THE COLONIC EPITHELIUM IN HEALTH AND CANCER

Colorectal Cancer

Incidence, diagnosis, and therapy

Colorectal cancer (CRC) is the third most diagnosed cancer and the third leading cause of cancer mortality in the United States (1). Increased surveillance has decreased CRC rates over 50, but incidences under 50 have increased by over 2% each year between 1992 and 2012 (2). Increased onset under 50 could be due to changing diet resulting in a perturbed microbiome. Therefore, experts have suggested that screening begins before the age of 50, especially if there is a family history or pre-existing gastrointestinal disease (3).

Although most CRC diagnosis is through colonoscopy, approximately 90% of individuals are symptomatic at diagnosis indicative of advanced disease and a lack of compliance to screening (2). The only curative treatment is surgical resection of the primary tumor. Often this is the only course of action available to CRC patients with stage 1 and, typically, stage 2 disease (4). In stage 3 CRC, where there is metastasis to local lymph nodes, resection

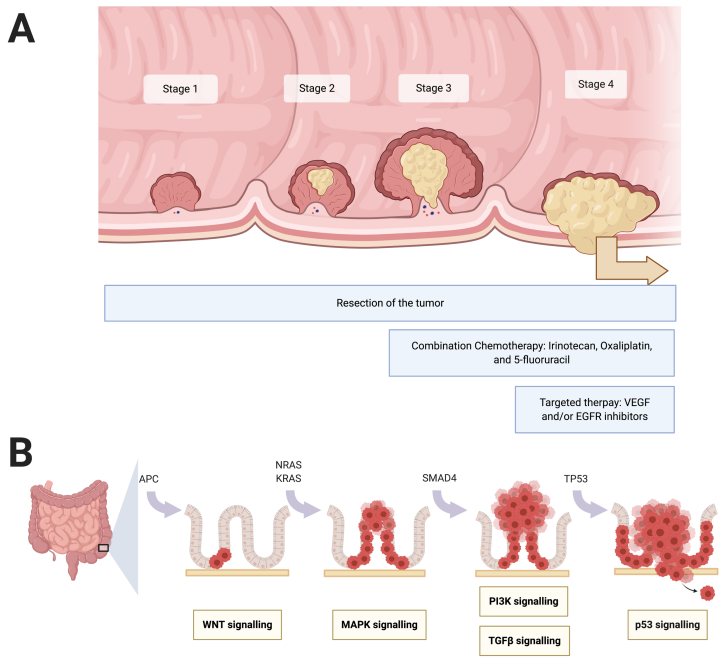

Fig 1.1. Overview of colorectal cancer progression and treatment. A) Basic staging and progression of CRC with their respective treatment options. B) The majority of CRC is MSS initiating with an upregulation of Wnt signaling through APC mutations. Over time tumor progression is worsen through the acquisition of additional mutations. *Figure created with biorender.com*

precedes adjuvant chemotherapy, which can include a combination of three major drugs and/or their derivatives-- Irinotecan, Oxaliplatin, and 5-fluorouracil (Fig 1.1A). Irinotecan binds irreversibly to topoisomerase I inducing double-stranded breaks due to topoisomerase's inability to unwind DNA (5). Oxaliplatin causes crosslinking of DNA, inhibiting DNA repair and synthesis (5), while 5-Fluoruracil leads to fluorinated pyrimidines, which initiates DNA-directed cytotoxicity (6). In Stage 4 CRC, defined by a presence of distant metastasis, resection of affected organs precedes adjuvant chemotherapy and possibly targeted therapies (Fig 1.1A) (7)**.** There are two approved targeted therapy categories—(a) VEGF and (b) EGFR inhibitors, which target angiogenesis through tyrosine kinase or RAS/RAF signaling pathways, respectively (8). While biomarkers for anti-VEGF are lacking, individuals with certain KRAS or BRAF mutant tumors cannot receive anti-EGFR therapy (9–11).

In rare cases (approximately 5%), immunotherapy can treat CRC and, compared to targeted therapy, results in better patient survival (12–14). Specifically, T cells' presence within colorectal tumors is a critical determining factor in whether or not immunotherapy will be beneficial. For instance, typically, the immune regulatory molecule programmed death-ligand 1 (PDL1) binds the immune checkpoint protein programmed cell death protein 1 (PD1) on T cells. PD1 acts as an immune checkpoint guarding against autoimmunity through promoting apoptosis of antigen-specific T cells and inhibiting T cell cytotoxic activity while reducing apoptosis of regulatory T cells. PD1 checkpoint therapy takes advantage of these mechanisms by inhibiting PD1 resulting in increased T cell cytotoxic activity (13). While there are clinical trials underway to determine the efficacy of

immunotherapy and similar therapeutic combinations in CRC, there is a dire need to improve our fundamental understanding of how CRC develops to develop better treatment strategies and improve CRC survival rates.

Classifying Colorectal Cancer

There are three ways to classify colorectal cancer (CRC): (a) analyzing epigenetic modifications, (b) Tumor Node Metastasis (TNM) staging, and (c) microsatellite status.

Epigenetic modifications

Epigenetic modifications are extra-genetic modifications that affect gene expression by altering DNA accessibility and chromatin structure (15). Examples include acetylation, histone modifications, and the most common modification, methylation. In 1999, Toyota *et al*. introduced the idea of analyzing CpG islands' methylation as a means to classify tumors (15–17). CpG islands are DNA regions that contain a cytosine nucleotide followed by a guanine nucleotide. A panel of five islands is analyzed and used for classification (15). However, this classification is not well accepted because other classification methods, such as microsatellite instability and TNM stage, need to be considered to witness any meaningful associations.

TNM staging and microsatellite status

Within the clinic, CRC classification occurs through TNM staging, which takes into account three significant characteristics of the tumor: the primary tumor (T), regional lymph nodes (N), and distant metastasis (M). These are analyzed on a scale to determine tumor staging and treatment options (18). Utilization of TNM staging occurs in conjugation with the tumor's microsatellite status resulting in two categories of tumors: microsatellite instable (MSI) and microsatellite stable (MSS). MSS tumors make up about 85% of all CRCs (19). MSS tumors initiate through an upregulation of WNT signaling via adenomatous polyposis coli (*APC*) mutations, followed by secondary epidermal growth factor receptor (*EGFR*), transforming growth factor-beta (*TGFB)*, and tumor protein P53 (*P53)* mutations (Fig 1.1B). Commonly known as the Vogelgram, this carcinogenesis pathway was established in 1990 and served as the foundation for other carcinogenesis pathways (20).

On the other hand, MSI tumors exhibit genetic hypermutability due to a deficient DNA mismatch repair system and account for up to 15% of all CRCs (21). The mismatch repair (MMR) system includes six proteins (MLH1, MSH2 MSH3, MSH6, PMS1, and PMS2) that interact to identify and repair DNA base mismatches and mutations. The most common deficiency in this system is hypermethylation of MLH1 promoters resulting in 1000s of mutations found within MSI tumors compared to 100s found in MSS tumors. MSI tumors are commonly associated with an influx of immune cells not seen in MSS tumors allowing a successful therapy response from immune therapy. Nonetheless, MSS tumors can also exhibit an influx of immune cells; therefore, immunoscore may be a better tumor

classification method than microsatellite status. Immunoscore analyzes immune cells' presence, specifically T cells, within various tumor regions to determine therapy response (22).

Colon biology

The colon is the second most distal region of the gastrointestinal tract. Luminal contents from the small intestine pass through the cecum and empty into the colon until the contents exit via the rectum. While the small intestine is primarily responsible for nutrient absorption, the colon is responsible for fluid absorption (23).

There are four layers throughout the gastrointestinal tract: the serosa, muscular layer, submucosa, and mucosa. The outermost layer is the serosa which contains connective tissue called the adventitia. The serosa besieges the muscular layer and includes inner circular and outer longitudinal muscle interspaced with intermuscular space (23). The muscular layer surrounds the submucosa layer, a connective tissue layer containing blood and lymphatic vessels, nerves, and glands. The innermost layer is the mucosa, which lines the digestive tract's lumen and consists of lamina propria, basement membrane, and epithelium. The lamina propria is a thin layer of connective tissue comprised of immune cells and fibroblasts surrounding the basement membrane (24). The basement membrane is an extracellular matrix composed of collagen and laminin fibers that support the intestinal epithelium, which lines the colonic lumen (24). The

epithelial layer is a unilaminar layer of polarized cells connected by junctions and focuses our investigation (24).

The intestinal epithelium is a rapidly renewing tissue layer such that the lining is replaced every two to three days in mice and three to five days in humans (25). Within the colonic epithelium, there is a cellular hierarchy with stem cells residing at the crypt's bottom (26–28). As cells move up the crypt, stem cells differentiate into more progenitor and transit-amplifying cells, ultimately giving rise to fully mature absorptive and secretory cell types (Fig 1.2) (26–28). Although cell fate largely depends on intrinsic qualities, extrinsic factors can also influence cell specification (26–28). For instance, cell position in the crypt or microenvironmental factors, such as microbes, neighboring immune, and epithelial cells, can influence cell fate.

One of the defining characteristics that can influence cell fate is the dynamic signaling environment within the colon. There is a high presence of Wnt and Notch signaling at the bottom of the crypts, decreasing toward the crypts' top (Fig 1.2A). Conversely, at the top of the crypts, Bone morphogenetic protein (BMP) and Hedgehog (Hh) signaling are relatively high and decrease towards the bottom of the crypts (Fig 1.2A) (29,30). This complex signaling environment determines the cellular composition within their range of influence. Precisely, an increase of Wnt and Notch signaling results in more stem cells, while a decrease in Notch signaling alone or in addition to the decline in Wnt drives cells towards a secretory cell fate. On the other hand, a reduction in Wnt and an increase in

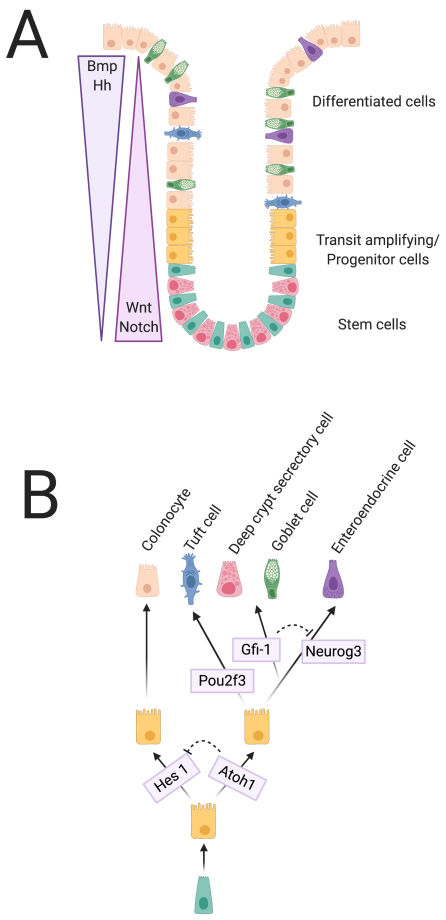

Fig 1.2. Overview of the colonic crypt make up. A) Basic cellular and signaling make-up of the colon. B) Transcription factors that play a role in colonic epithelial cell differentiation. *Figure created with biorender.com*

Notch signaling drive absorptive cellular fate (31). In the context of these three cell populations, I will touch on their function, characteristics, and how cell fate determination.

Stem Cells

Stem cells are undifferentiated, non-polarized cells capable of giving rise to differentiated cell types. Multipotent stem cells can give rise to the entire complement of differentiated lineages of the colonic epithelium. They are defined by two principles: a) self-renewal and b) multipotency (32). Although the debate of the "true" identity of an intestinal stem cell is ongoing, the fate of the stem cell is determined by two interdependent principles: a) signaling niche relative to the cell and b) population equilibrium through neutral drift (27,33). Stem cells will divide symmetrically but leave their immediate niche due to mitotic pressure. This movement exposes cellular progeny to a different signaling environment driving them toward a different cell fate. Cells that remain in the immediate niche maintain their stem cell nature primarily due to the Wnt signaling ligands from the surrounding microenvironment and neighboring cells. These intimate interplays allow for the maintenance of stem cells while also differentiating and replenishing apoptotic cells. There are two significant stem cell populations within the homeostatic colonic epithelium: crypt base columnar cells and the quiescent '+4' stem cell.

Crypt base columnar cells

Crypt base columnar cells (CBCs), discovered by Leblond, Cheng, and Bjerknesare, are found at the bottom of the crypts (34). They are actively dividing cells and give rise to the majority of the colonic epithelial cells. They express leucine-rich repeat containing G protein-coupled receptor 5 (LGR5), an R-spondin receptor that plays a role in canonical Wnt signaling. A single-cell study by Biton *et al.* demonstrated several subpopulations of intestinal stem cell populations, termed ISCI, ISCII, and ISCIII, within a continuum of proliferative and differentiation states. In particular, ISCIIIs are more proliferative, resemble transit-amplifying cells, and possess major histocompatibility complex class 2 (MHCII) antigen presentation capabilities (35).

+4 cells

On the other hand, a more quiescent, label-retaining cell population discovered in the late 1950s resides 4-cells above the crypt base. This +4 stem cell population activates upon damage conditions, such as radiation or dextran sodium sulfate (DSS) treatment. Three markers identify the quiescent '+4' cell: homeobox only protein x (HOPX), telomerase reverse transcriptase (TERT), and leucine-rich repeats and immunoglobulin-like domain 1 (LRIG1) (36–38). Interestingly, LRIG1 expression overlaps between both CBCs and the +4 stem cells (38). However, there is a presence of LRIG1 differential expression: non-glycosylated Lrig1 in +4 cells, glycosylated Lrig1 in CBCs (39). In summation, LRIG1+ LGR5+ expression identifies CBCs while LRIG1+LGR5- expression identifies +4 cells.

Differentiated cells within the colon

There are two major subsets of differentiated cells within the colon: the absorptive colonocytes and secretory cells consisting of the goblet, deep crypt secretory, tuft, and enteroendocrine cells.

Colonocytes

The absorptive colonocytes found at the top of the crypt and the intercrypt table, the epithelium between crypts, encompass 80% of all the colonic epithelium cells (40). Colonocytes are responsible for water and nutrient absorption through active and passive transport. Active transport is the movement of chemicals against their chemical gradient from low concentration regions to high concentration. In contrast, passive transport is the movement of chemicals from high to low concentration (24). Increased Notch signaling, through the transcription factor hairy and enhancer of split-1 (HES1), drives the absorptive cellular fate while inhibiting secretory cell fate (Fig 1.2B) (40,41).

Goblet cells

The absence of HES1 drives secretory fate. Specifically, MATH1 (ATOH1), known as the master secretory fate regulator, inhibits HES1 expression decreasing specificity to colonocytes and driving secretory cell fate (Fig 1.2B) (40). There are four subpopulations of secretory cells within the colon. Goblet cells, the largest population of secretory cells,

make up approximately 16% of all colonic epithelium cells (24). The transcription factor GFI1, downstream of MATH1, determines goblet cell fate by inhibiting other secretory cell fates (Fig 1.2B) (41). Goblet cells produce mucins, large glycoproteins critical for barrier defense and microbiome regulation, which are essential to providing a separation between the microbiome and the epithelial layer. They also secrete trefoil factors to aid in tissue repair and are found in other parts of the body, including the respiratory tract, eyelids, and tears. Due to these secretion factors, mucin 2 (MUC2) and trefoil factor 3 (TFF3), along with the presence of mucin droplets, are commonly used to identify goblet cells within the epithelium (24).

Deep crypt secretory cells

Deep crypt secretory cells, found between the stem cells at the bottom of the crypts, also express goblet cell markers however, their exact function and identity are elusive (42). They are distinct from goblet cells through their expression of KIT proto-oncogene receptor tyrosine kinase (CKIT) and regenerating islet-derived protein (REG4) (43,44). . Moreover, they have similar characteristics as CKIT expressing Paneth cells found in the small intestine but also express critical stem cell maintenance factors, including Notch ligands DLL4 and DLL1 and EGFR and its ligand EGF. Therefore, the field recognized deep crypt secretory cells as Paneth-like cells that serve as precursors to goblet cells (43–45).

Tuft cells

Another secretory cell type whose function and classification remains elusive is the tuft cell. Until recently, tuft cells were another +4 reserve stem cell, but in 2009 Gerbe *et al.* revealed doublecortin-like kinase 1 (DCLK1) as a tuft cell market and defined this as a distinct mature cell population, identifiable by their "tufted" apical membrane (46). Interestingly, tuft cell classification as a secretory or absorptive cell is location-dependent within the gut. In the colon, tufts cells are secretory, but in the small intestine, they are absorptive cells developing independent to the ATOH1 (MATH1) secretory lineage (Fig 1.2B) (47). Their function is still elusive, but one of their primary roles is to act as immune cells providing defense to helminth worm infection (48–50). In the colon, their function is even more cryptic. Still, tuft cells are similarly capable of responding to luminal microenvironment perturbation as tuft cell frequency increased in germ-free mice after introducing microorganisms (51).

Enteroendocrine cells

Lastly, enteroendocrine secretory cells are part of the enteric endocrine nervous system driven by Neurogenin 3 (NEUROG3) expression downstream of Atoh1 (Fig 1.2B) (41). Marked by Chromogranin A (CHGA), which plays a role in secretory granule formation, enteroendocrine cells secrete hormones that regulate glucose homeostasis, satiety, and pH balance, as well as gut motility (52).

Colon and colon tumor cellular dynamics

Much attention in the cancer research field has focused on describing cellular functions by genetic alterations. However, non-genetic factors can also determine the diversity of cellular functional states in an organismal context (53). How these different contexts dictate the properties of tumor stem cells remains an area of investigation. Here I will discuss how non-genetic factors dictate non-stem cells' dynamics and translate them into tumor cell dynamics.

Non-stem cell plasticity

The intestinal and colon epithelia are highly dynamic systems where continuous stem cell differentiation replenishes intestinal cell lineages, all with specific prescribed functions. This robust process contains several fail-safe mechanisms, where multiple stem cell populations, each with different properties, can be called into duty when required. For instance, LGR5 expressing stem cells actively proliferate and act as the workhorse for epithelial replenishment. Upon damage or elimination of LGR5 expressing stem cells, multiple cell populations, each with different proliferative capacities within the differentiation continuum, can serve as "facultative" stem cells, exhibiting cellular plasticity (54–61). Cellular plasticity is a cell's ability to reversibility adopt diverse cellular identities within a phenotype spectrum (62). Three examples include transdifferentiation, dematuration, and dedifferentiation (Fig 1.3).

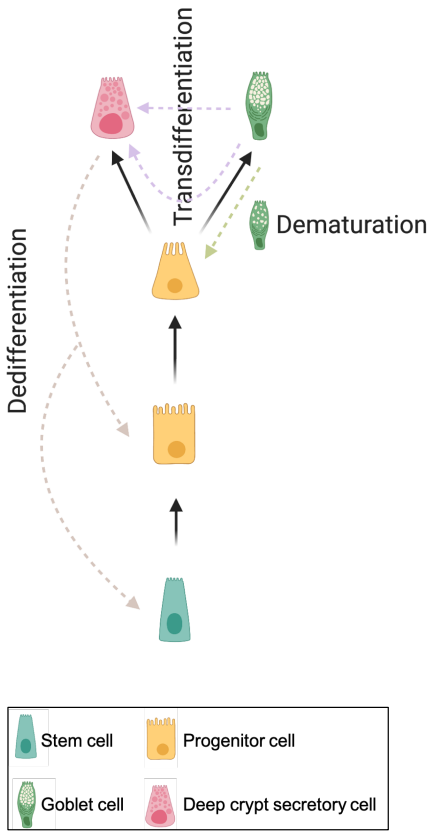

Fig 1.3. Plasticity of non-stem cells. Non-stem cells can undergo dematuration, transdifferentiation, and/or dedifferentiation under different microenvironmental contexts. *Figure created with biorender.com*

Transdifferentiation

Transdifferentiation is when one mature somatic cell transforms into another mature somatic cell without an intermediate pluripotent or progenitor cell state, usually in response to a specific signal (Fig 1.3). For instance, in the stomach, under metaplastic states of stress, chief cells transdifferentiate to Spasmolytic Polypeptide-Expressing Metaplasia (SPEM), a metaplastic mucous cell lineage (63). This process is also commonly associated with dematuration, during which a secretory cell will downregulate its secretory apparatus to transition into a new cell type. For example, when chief cells transdifferentiate into SPEM, they simultaneously downregulate their zymogen secretion machinery and upregulate their mucous granule secretion mechanism. In this process, chief cells do not dedifferentiate to a pluripotent, progenitor state before transitioning to the new cell state (64).

Dematuration

Dematuration is the downregulation process in cellular phenotype without ultimately regaining stem capacity (Fig 1.3) (64). This phenomenon is especially true for secretory cells that express scaling factors in later cellular maturation stages. Scaling factors are transcription factors that, when turned on, affect a multitude of cells. For instance, when the expression of the scaling factor MIST1 occurs, secretory granules develop in various immature secretory cells, thus allowing full maturation and secretory function of these cells (65). Upon loss or inhibition of this scaling factor, secretory cells lose their secretory

granules, unable to function correctly but do not entirely regress to a progenitor-like state; therefore, they undergo dematuration.

Dedifferentiation

Dedifferentiation is the process of a mature cell type reverting to a progenitor-like state under stress signals (Fig 1.3). These cells regain stem capacity properties (54,66,67). Within the colon, both absorptive and secretory cells can regain stem capacity and replenish the colonic epithelium upon ablation of LGR5 expressing stem cells. A seminal study ablated LGR5 expressing stem cells and found that ALPI expressing absorptive progenitors can regain stem capacity and replenish the colonic epithelium (54).

Most studies in the colon investigating the dedifferentiation of mature cell types examine secretory cells. For instance, DLL1 expressing early secretory progenitors, which give rise to the four principal secretory cells within the colonic epithelium, can regain stem capacity under homeostatic and stress-induced through irradiation (55). Similarly, upon irradiation, cells expressing ATOH1, a regulator of secretory cell specification, are known to regain stem capacity (59). These examples are secretory progenitor cells but committed secretory cells can also exhibit dedifferentiation, although at a much lower rate than progenitors.

For example, hormone-secreting enteroendocrine cells, marked by NKX2.2, exhibit plasticity when stem cells are ablated (68). Moreover, DCLK1 expressing tuft cells exhibit

plasticity after irradiation or DSS-mediated damage (69). Interestingly, without absorptive cells, secretory cells cannot regain stem capacity after stem cell ablation and vice versa (70). This phenomenon suggests that the field is just starting to elucidate the intricate processes of the cellular dynamics of non-diseased tissue. Chapter V explores how cellular plasticity can relate to tumorigenesis initiation and the retention of the tumor cell-of-origin signature after tumor formation.

Tumor cell dynamics

Tumor dynamics depend on the cellular distribution in the tumor and microenvironmental niche. These interactions' dynamics are best explained in the tumor's clonality, the tumor cell of origin and tumor stem cells.

Clonality in cancer

Colorectal cancer is monoclonal, meaning tumors can arise from one cell (71). This event is possible through clonal expansion and fitness evolution. For instance, a stem cell X can acquire a mutation (Fig 1.4). This mutation gives stem cell X a fitness advantage over surrounding stem cells, allowing cell X to divide more quickly and give rise to more progeny than other non-mutated stem cells (Fig 1.4). Over time, the progeny of the cell X outnumbers the progeny of non-mutated cells in the crypt, resulting in clonal expansion of mutated stem cell X at the disadvantage of other stem cells (Fig 1.4). However, there is no neoplasia involved until a second mutation occurs in stem cell X (Fig 1.4). When a

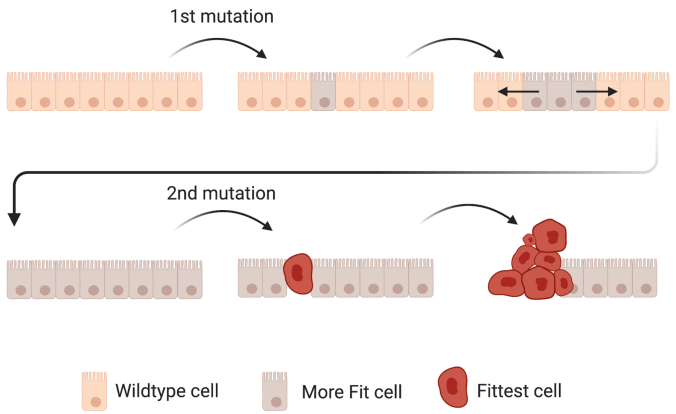

Fig 1.4. Colorectal cancer is monoclonal. When a mutation occurs in a cell resulting in a fitness advantage, the whole crypt will eventually express that fitness advantage. After a second mutation occurs, resulting in an even more fit cell, a tumor can form. *Figure created with biorender.com*

second mutation occurs but is not corrected, the same clonality process occurs, ultimately leading to a monoclonal tumor (Fig 1.4). It is essential to distinguish between the tumor cell-of-origin and tumor stem cell within these tumors to understand how to treat these tumors.

Tumor cell-of-origin

The tumor cell-of-origin is the tissue-resident cell that acquires an oncogenic mutation, triggering tumorigeneses (Fig 1.5). Parallel to clonality in homeostasis, the tumor cell-of-origin could be a stem cell capable of giving rise to tumors. Nevertheless, it could also be a non-stem cell under optimal conditions (Fig 1.5). All tumor cells, including tumor stem cells, are progenies of the tumor cell-of-origin. The tumor cell-of-origin is challenging to identify in humans, as there is only a snapshot of the tumor when diagnosed instead of the tumor's continuous evolution. On the other hand, engineered mice express mutations in particular cell types allowing investigation of the relative tumor cell-of-origin.

Greater than 80% of sporadic CRC cases develop when both *APC* alleles are inactivated (72). It is well-accepted that when such Wnt pathway perturbing event occurs in crypt base stem cells, tumors can arise (38,67,73–79). However, Schwitalla *et al.* laid the foundation for non-stem cell-driven tumorigenesis upon oncogenic activation of Wnt signaling and damage (67). Other studies have since shown that oncogenic alterations in secretory and tuft cells can initiate tumorigenesis (55–57,59). Whether tumorigenesis

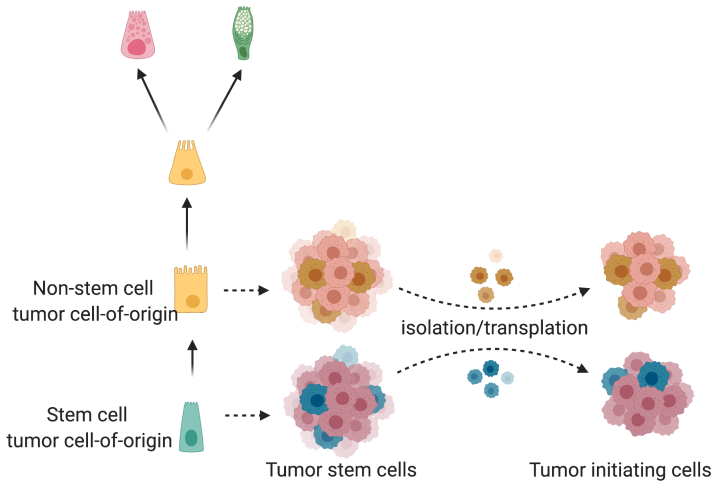

Fig 1.5. Non-stem and stem cells can serve as tumor cells-of-origin. *Figure created with biorender.com*

occurs directly in non-stem cells or through a stem cell intermediate via dedifferentiation, these studies still provide different contexts that generate tumor stem cells.

Tumor stem cells

Within the diversity of cell types in a tumor, tumor stem cells represent a significant cell population influential to tumor malignancy and patient diagnosis (80,81). Tumor stem cells possess stem characteristics to self-renew and maintain the diversity of cell types observed within the tumor (80). Several groups have reported various tumor stem cells' properties, including the ability to resist cytotoxic therapy, repopulate the tumor, and metastasize to distal sites (82–85). Furthermore, recent large-scale data-driven efforts from The Cancer Genome Atlas (TCGA) have identified a stemness index associated with advanced tumor grade, metastasis, and an altered immune microenvironment in various cancer types (86). The tumor stem cell field remains contested, owing, in part, to the lack of understanding regarding the origin of different stem-like properties in the tumor, but I hypothesize that both non-stem and stem cell driven tumors contain a tumor stem cell population that maintains a signature of the tumor cell-of-origin.

The immune system and its role in tumors

Immune cells derive from hematopoietic stem cells found in the bone marrow differentiating from either a common lymphoid or myeloid progenitor, separating them into myeloid or lymphoid cells (87).

Myeloid Cells

Myeloid cells are the progeny of a myeloblast progenitor resulting in two significant categories of myeloid cells: granulocytes and monocytes. Granulocytes contain digestive enzymes that are released upon ingestion of foreign entities and include basophils, neutrophils, and eosinophils. On the other hand, monocytes eventually become macrophages or dendritic cells, which are also considered professional antigen presenting cells (APCs) (87). APCs phagocytose foreign entities and present antigens to naïve T cells through the use of major histocompatibility complexes (MHC). MHC class I (MHCI) is used to directly initiate the killing of pathogens by activating cytotoxic CD8 T cells. APCs utilize MHC class II (MHCII) to induce helper T cells into effector T cells.

Activation of various myeloid cells is a quick process and typically halted upon the stimuli' termination (88). However, under pathological conditions like tumorigenesis, persistent stimuli result in aberrant phagocytosis and signaling perturbation, leading to an immature myeloid cell population termed myeloid-derived suppressor cells (MDSCs). MDSCs protect the host from tissue damage due to a heightened immune response associated with increased persistent inflammatory stimuli (88). They are a heterogeneous myeloid cell population with characteristics resembling macrophages, dendritic cells, and granulocytes. Given these characteristics, one set of markers cannot define them, but they express various elements seen throughout myeloid cells' differentiation process (88,89).

Identified by GR1 and CD11B, there are two categories of MDSCs: granulocytic MDSCs (G-MDSCs) and monocytic MDSCs (M-MDSCs). Their classification depends on the presence of granulocytic or monocytic phenotypic markers. G-MDSCs express high LY6G and low LY6C expression and produce reactive oxygen species to suppress immune cells. On the other hand, M-MDSCs have high LY6C and low LY6G expression and generate nitric oxide to inactivate the immune response. There is a delicate balance in myeloid cell-promoting cytokines. When there is an increase in various cytokines, including CSF-1, GM-CSF, and G-CSF, indicating inflammatory activation, there is increased recruitment and development of innate immune cells like dendritic cells, macrophages, and granulocytes. Prolonged or inflated cytokine increases in combination with additional cytokines and signaling molecules perturb the normal development of innate immune cells leading to increased MDSC accumulation and function (89).

Lymphoid cells

There are three lineages of lymphoid cells: Natural killer cells, B lymphoid cells, and T lymphoid cells. Natural killer cells can directly kill cells infected with antigen without further sensitization, unlike the T and B cells of the adaptive immune system. Both B and T cells, on the other hand, need to be activated before expansion and differentiation. Although naïve B and T cells derive from a common lymphoid progenitor, their names originate from their maturation location; B cells mature in the bone marrow while T cells mature in the thymus. Following maturation, B and T cells circulate the body through the lymph to

secondary peripheral lymphoid organs, where they are maintained and encounter antigens (87).

B lymphocytes

B lymphocytes also known *as* B cells, the third type of APC, will directly encounter antigen through its B cell receptor (BCR) and undergo activation. Once activated, B cells differentiate into three major cell types: plasmablasts for immediate protection, in addition to longer-lived plasma cells and memory B cells. Plasmablasts and plasma cells secrete antibodies, but plasmablasts are short-lived and secrete antibodies that are less specific than antibodies secreted from plasma cells. Memory B cells are dormant B cells that circulate the body. Once they reencounter a particular antigen, they initiate a more robust, quicker antibody response to counteract the target pathogen.

T lymphocytes

T lymphocyte, also known as T cell, maturation begins with thymocytes differentiating into naïve T cells in the thymus. Naïve T cells circulate throughout the body, but once they encounter an antigen with a professional APC's help, they become activated and undergo clonal expansion and differentiation into effector T cells. There are two significant types of effector T cells: cytotoxic CD8 cells and helper CD4 cells. Cytotoxic CD8 cells, also known as killer T cells, are activated directly through MHCI and induce killing of the infected cells by releasing the cytotoxins perforin, granzymes, and granulysin. On the

other hand, antigens expressed through MHCII activate CD4 helper T (Th) cells. This activation can also generate T regulatory (T reg) cells, limiting or inhibiting cytotoxic CD8 response (87).

When an APC presents antigen to T cells, an intricate remodeling process of integrins and receptors must occur to activate and remold the naïve T cell into the mature cell type. The T cell receptor (TCR)-MHC complex must be bound to the antigen in addition to the correct CD4 or CD8 co-receptors. Still, co-stimulatory signals must also be present to activate the T cells fully. For instance, B7 molecules expressed on APCs will interact with CD28 on T cells to stimulate T cell expansion. Once activated, the co-stimulatory signal is modified, leading to further expansion and differentiation of the T cells. CD40 (T cells)-CD40L (APCs) is one such interaction. Their interaction results in transcription factor synthesis to induce transcription of the IL2 gene and its further secretion. IL2 acts in an autocrine fashion, supporting further activation, expansion, and differentiation of T cells (90).

CD28 related proteins on activated T cells can modify and sustain the co-stimulatory signal throughout the T cell response. For instance, CTLA4 can be expressed on T cells and bind to B7 molecules more tightly than CD28, inhibiting T cells' activation. Conversely, ICOS, a CD28 related protein, can bind LICOS on APCs, enhancing T cell's expansion through IL10 instead of IL2 (91). These proteins are common targets of immunotherapy discussed below.

After the infection is under control, most T cells die off, but a small subset persists and transitions into memory T cells. These T cells downregulate the program of effector T cells but remain capable of reactivating effector function if necessary. During this time, memory T cells will adapt a self-renewal characteristic driven by IL-7 and 15 signaling (92). Conversely, inappropriate T cell activation, either by chronic stimulation or a lack of stimulatory signal, results in dysfunctional T cells. Under chronic pathogenesis, like cancer, memory T cell development is altered and, instead, T cell exhaustion phenotype develops. Specifically, prolonged increased expression of IL10, IL6, TGFB, IDO, and IFNs can lead to exhausted T cells. There is a loss of effector functions in T cell exhaustion and a breakdown of memory T cell antigen-independent homeostatic function. There is upregulation of multiple inhibitory receptors like CTLA4, PD1, LAG3, CD244, CD160, and TIM. Moreover, there is a downregulation of co-stimulatory molecules TRAF1 and CD137. Furthermore, there is an altered expression of transcription factors and metabolic derangements (92). One hallmark of some dysfunctional T cells is the alteration of mitochondrial biogenesis and function (93). On the other hand, antigen recognition without co-stimulatory molecules inactivate native (or naïve) T cells and induce an anergic state, where the inability to secrete IL2 is a defining feature (87,94–96). Both exhausted and anergic T cells are characteristics found within tumors.

Tumor Immunology

Tumors can be classified as "hot" or "cold" tumors where hot tumors have high infiltration of CD3 and CD8 cells in different regions of the tumors while these populations are absent in cold tumors. Utilizing the type, density, and location of these immune cells in the tumors is called the immunoscore. When used in conjugation with the TNM scoring metric, it has been shown to more accurately predict patient outcomes (97–100). Likewise, hot tumors have increased immune checkpoints, including PDL-1, CTLA4, TIM3, and LAG3, decreased genomic stability, and increased mutation burden and neoantigens (Fig 1.6). Conversely, cold tumors exhibit increased genomic stability and lower immune checkpoints, antigen presentation machinery, neoantigens, and mutation burden (101). As a result, hot tumors are better candidates for immunotherapy than cold tumors (Fig 1.6). A popular immunotherapy, immune checkpoint inhibitors, target CTLA4, PD1, and PDL1, but the majority of patients with metastatic epithelial cancers treated with immunotherapy still do not experience regression (102). On the other hand, cold tumors do not readily express easily targetable immune components; therefore, it is dire to investigate other cold tumors' features to determine how to treat them via activating the immune response or other means.

Hallmarks of cancer

The hallmarks of cancer have undergone recent revision. Initially, in 2000, six hallmarks of cancer were established: 1) sustaining proliferative signaling, 2) resisting cell death, 3)

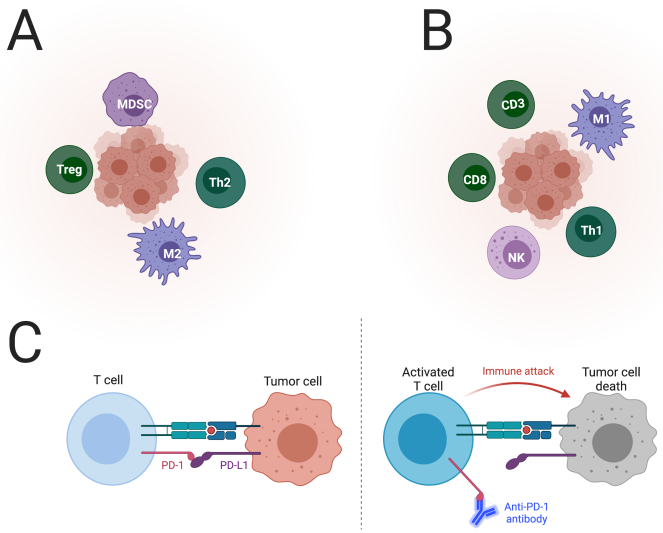

Fig 1.6. The tumor immune microenvironment can be manipulated by the tumor and treatments. A) Cold tumors present a more anti-inflammatory immune microenvironment allow tumors to thrive, while (B) hot tumors exhibit a more cytotoxic microenvironment inhibiting tumor growth. C) Immunotherapy can be used to manipulate these environments, but especially takes advantage of the hot tumor microenvironment. *Figure created with biorender.com*

evading growth suppressors, 4) inducing angiogenesis, 5) enabling replicative immortality, 6) activating invasion and metastasis. More recently, though, four additional hallmarks were introduced: 1) Avoiding immune destruction, 2) tumor-promoting inflammation, 3) deregulating cellular energetics, 4) genome instability and mutation (Fig 1.7) (103). While all ten factors are critical for tumor survival, this work's centrality is around the tumor immune microenvironment focusing on five hallmarks: resisting cell death, inducing angiogenesis, avoiding immune destruction, tumor-promoting inflammation, and deregulated cellular energetics. These condense to exploring tumor immune escape and the Warburg effect described below.

Tumor immune escape

The tumor microenvironment is an intricate system dictated by the cells' signaling and composition within and surrounding the tumor. Since tumors are plastic and unique, the field is just starting to understand how the tumor microenvironment functions. One major player in this is the signaling and composition of the tumor immune microenvironment. The immune composition itself can skew the microenvironment to be anti- or pro-tumorigenic. For instance, the presence of natural killer cells, CD4+ Th1 cells, cytotoxic CD8+ T cells, and inflammatory macrophages within a tumor are typically anti-tumorigenic (Fig 1.6). On the other hand, the presence of immunosuppressive populations like MDSCs, CD4+ regulatory T cells, and anti-inflammatory macrophages are pro-tumorigenic (Fig 1.6) (93). The tumor can manipulate the influx of immune cells. For one, tumor cells can act as antigen presenting cells, but they lack the co-stimulatory

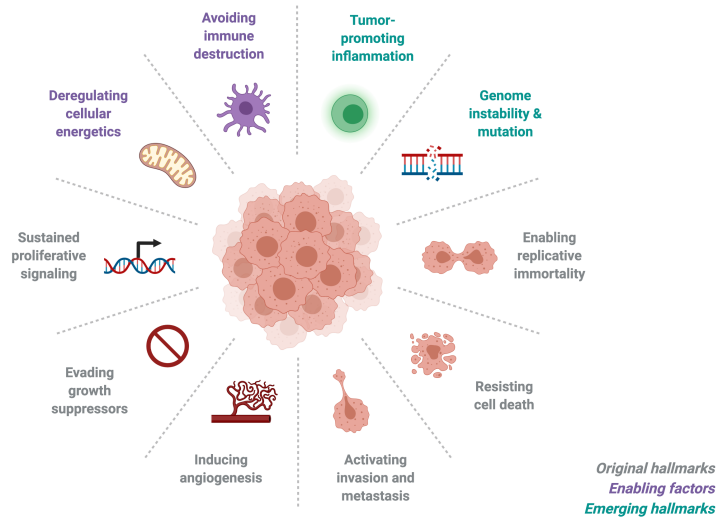

Fig 1.7. Hallmarks of cancer. *Figure created with biorender.com*

molecules found on traditional antigen presenting cells. Therefore, antigen presenting tumor cells can promote immune tolerance, promoting tumorigenesis (104). Microbes within the tumor can also promote an inflammatory program within the tumor, causing expansion of MDSCs and anti-inflammatory M2-like tumor-associated macrophages (105). They can also cause the upregulation of immunosuppressive ligands like PDL1 and CTLA and cytokines like TGFB, all of which play a role in suppressing the activation of CD8 cells and increasing suppressive CD4 T cell populations-- like regulatory T cells-- allowing the tumor to escape immune surveillance (105).

A significant hindrance to effectively treating tumors by manipulating the immune microenvironment is the paradoxical roles of lymphoid and myeloid cell populations. Depending on the context, these cell types can be alternately tumor-promoting or tumor-suppressive (87,88,94,96). A principal example of this is in the case of T cell dysfunction. At the beginning of an immune response, an increase of myeloid cells is beneficial. T cells are activated and can induce apoptosis of targeted cells. If this increase of myeloid cells is chronic, though, like in tumors, the T cells become "exhausted," and cytotoxic programs become dysfunctional, allowing the tumor to thrive unnoticed. Under these conditions, depletion of this myeloid cell population may reactive an antitumor response.

Warburg effect

The Warburg effect occurs when tumor cells upregulate glycolytic catabolism of glucose to form lactate under low oxygen conditions or hypoxia (104). Within hypoxic regions,

necrosis increases due to a lack of nutrition to cells. Necrosis leads to increased potassium released by dying cells, which remodels the activated T cells' epigenome and limits T cell effector function. Within hypoxic regions, there is also a lack of glucose due to anaerobic glycolysis in tumor cells and increased lactic acid production (104). This lack of glucose decreases CD4 and CD8 cells' effector function, ultimately resulting in increased T cells and memory T cells (104). Moreover, hypoxic regions of the tumors have an influx of macrophages that help produce angiogenesis, mitogenic, and associated metastatic cytokines, enabling tumor development. Studies have shown that under *in vitro* hypoxia conditions, MDSCs favor an M2-like tumor-associated macrophage phenotype (106).

The field is just starting to understand the dynamics of tumor cells and the tumor microenvironment. Throughout this thesis, I characterize these dynamics from a systems biology view utilizing single cell technologies. Specially, I explore how signaling pathways and cellular composition is altered in tumor subtypes stressing the importance of molecular features of tumor compared to pathological classification. Moreover, I explore how the tumorigenesis cell-of-origin dictates tumor stem cell characteristics and ultimately the cellular composition and microenvironment of the tumor. These investigations require single cell technologies to be able to investigate rare cell populations that were previously overlooked by more traditional technologies.

Chapter II

BACKGROUND

METHODOLOGIES USED FOR SYSTEMS BIOLOGY

Single-cell Technologies

Many whole-sample techniques assume homogenous cell distributions in tissue systems, but conventional proteomic and genetic methods often lack the sensitivity to detect the underlying molecular heterogeneity in multi-cellular networks. This lack of sensitivity masks the biological significance of rare cell populations. These rare cell populations' importance, though, is critical to understanding both steady-state and disease pathophysiology. For example, tumor stem cells, relevant throughout this work, are only a fraction of a large tumor that can often go undetected by western blots and other "bulk" approaches that assume a homogenous cellular distribution. Like stem cells, tumor stem cells can regenerate the cellular lineages comprising primary tumors. The field hypothesizes that these tumor stem cells can even evade cancer therapy, leading to reoccurrence and increasing disease aggression.

To observe rare cell populations, including tumor stem cells, single-cell methodologies were developed. These methodologies are conceptually grouped as either blind, non-candidate approaches and targeted, candidate-based approaches to assay single-cell suspensions or dissociated tissues (non-suspension). Each method provides unique

insights, and, therefore, utilization of a combination of them will systematically develop a complete picture of the underlying tissue. As this approach leads to a plethora of data, streamlining the subsequent analysis is a significant hurdle. Given this, multiple pipelines and algorithms exist.

Non-candidate approaches

Non-candidate, single-cell approaches are an unbiased way to obtain data because a pre-test panel of candidate analytes is not required. The most commonly used non-candidate approach is single-cell RNA sequencing (scRNA-Seq) (107). Tissues subjected to scRNA-Seq are first dissociated into single cells and placed in a fluid suspension. Depending on the amount of information needed, project budget, tissue type, and technical skills, there are multiple ways to conduct scRNA-Seq (108,109). In this work, scRNA-Seq occurs through the In-Drop encapsulation method, which encapsulates each cell into a droplet. Upon encapsulation, the cell is lysed and fused with a hydrogel microsphere containing unique molecular identifies before being processed into nucleic libraries for sequencing (109). A hurdle in utilizing single-cell RNA sequencing is processing the sheer volume of data produced. The assessment of thousands of genes within thousands of cells occurs; therefore, multiple algorithms and pipelines exist, some discussed briefly below.

Candidate-based approaches

Candidate-based approaches require *a priori* predictions to develop a panel of probes for specific tissue features. These approaches include flow cytometry, cytometry time-of-flight (CyTOF), and multiplexed immunofluorescence. In flow cytometry, there is a mixture of fluorescent-conjugated antibodies for cell-specific epitopes and the cell suspension (110). The labeled cells flow through the cytometer one at a time, and the cells are sorted based on their emission spectra. Analysis of thousands of cells occurs for approximately seven different epitopes at one time. However, spectral overlap from the light wavelengths limits the number of analytes. The development of CyToF has overcome this pitfall. CyToF combines flow cytometry with mass spectrometry by employing metal-conjugated antibodies instead of fluorescently labeled ones, which increases the possible number of simultaneous analytes up to sixty (111).

Flow cytometry and CyTOF require the tissue to be dissociated into single cells and kept in a fluid suspension. One caveat to dissociating epithelial tissue is that epithelial cells are highly polarized and closely connected with neighboring cells through junctional proteins. Once dissociation of the epithelial cells into single cells occurs, these characteristics are modified, resulting in data artifacts. We developed a novel fixation and dissociation approach called "Disaggregation for Intracellular Signaling of Single Epithelial Cells from Tissue (DISSECT)" to preserve the native state of epithelial cells for single-cell analysis using mass and flow cytometry (112). DISSECT provides an advantage over traditional flow cytometry and CyToF by preserving specialized cell characteristics lost in dissociation. Briefly, the tissue is stained, and the antibodies are

fixed to the tissue before dissociated into single cells. We have successfully applied the DISSECT technique to fresh, frozen, and FFPE tissue samples from mice and humans (113,114). Excitingly, these studies demonstrated that DISSECT preserves signaling states and might be a superior assay to the traditional gold standard of western blotting (112). Furthermore, we can apply this methodology to human FFPE banked colorectal cancer samples to understand better colorectal cancer subtypes (discussed in Chapter III) (114). Although this technique's application can be to fresh, fresh-fixed, and FFPE samples, slight modifications are necessary. A detailed discussion of these modifications follows in Chapter IV (113).

With suspension methodologies like flow cytometry and CyTOF, there is a loss of spatial understanding of the analytes when dissociation of the tissue into single cells occurs. The cells' location and their signaling relative to one another is crucial as it can have dire consequences. For instance, the location of immune cells within tumors can determine the tumor's classification and treatment. If immune cells are within the tumor, the tumors will fall into the MSI category of tumors, and treatment could consist of immunotherapy. On the other hand, if immune cells are present just outside the tumor but not within, the tumors will fall into the MSS category of tumors, and immunotherapy would be ineffective. Suspension methodologies would not consider these immune cells' location, and therefore the tumors would be in the same class. However, multiplexed immunofluorescence (MxIF) will resolve this ambiguity. MxIF is irritative staining and inactivation of fluorophores allowing analysis of up to 60 different analytes on one tissue section (115). Since MxIF lacks tissue disassociation, visualization and quantification of

tumor cells and their microenvironment are possible, providing context for classifying or treating tumors. When conducted at the proper resolution, multiplexed dozens of analytes can be quantified for thousands of cells, resulting in high dimensional data. It is advisable to utilize multiple single-cell techniques to acquire a thorough understanding of the native tissue environment, resulting in a colossal amount of data to analyze.

Single-cell data analysis

With the evolution of single-cell methodologies comes a massive increase in the amount of data generated, and as such, analysis of high-dimensional data has become its own field. The utilization of dimensionality reduction techniques allows the study of the different cell populations and their relationships. These analyses allow visualization of high-dimensional (3+) data in 2-dimensional space. The two dimensionality reduction techniques used in this work are t-Distributed Stochastic Neighbor Embedding (TSNE) and Uniform Manifold Approximation and Projection (UMAP). TSNE is a non-linear dimensionality reduction approach. It preserves the data's local structure while de-emphasizing global structure, resulting in similar points clustering together in an unsupervised manner. Because the global structure is not maintained, though, the relationship between the clusters is not meaningful (116). UMAP, on the other hand, preserves some global structure, ensuring that far away points in high dimensions are still far away in low dimensions (117). Because of this, single-cell genomic analyses have transitioned to using UMAP over TSNE for dimensionality reduction analyses; therefore, the utilization of TSNE occurs in Chapters III-IV and UMAP in Chapter V.

Dimensionality reduction is only one way to process, visualize, and analyze the data, though. Analysis of the global structure of the data occurs through trajectory analyses. There are two main groups of trajectory analyses: non-linear embedding approaches and Minimum Spanning Trees (MST). Similar to TSNE, non-linear embedding utilizes non-linear dimensionality reduction techniques to reduce high-dimensional data into 2- to 3-dimensional representation. Unlike TSNE, these analyses maintain the data's global structure, capturing the data's major structures and progression by compressing and elongating it (118). For this work, we utilized MST- based approaches to analyze the trajectory. The nodes used in MST represent cells or clusters of cells, while the connections represent the data cloud's shape in 2 dimensions. Many MSTs are known to be unstable such that multiple runs with the same application result in seemingly random results and overfitting smaller datasets. To overcome this, we developed p- Creode (47). The p-Creode algorithm is an unsupervised trajectory analysis that generates a unique cellular hierarchy placement of cell-state transition trajectories from end states allowing to decipher predecessor-progenitor relationships. It differentiates itself by exploiting an aggregation of a given number of resampled topologies lessening overfitting effects. It has proven robust and successful in several tissue types, including the pancreas and the intestine. It also can be modified to fit the user's needs. This work shows its usefulness in interpreting tumor cells' ratio derived from LRIG1 and MIST1 expressing cells, as seen in Chapter V.

Organoid culture

Regenerative medicine is built on the ability to culture stem cells and differentiate them into functional organs *in vitro* (119). Utilization of this phenomenon occurs in many organ systems, but most notably through induced pluripotent stem (iPS) cells. iPS is a technique that infects non-stem cells with factors that stimulate a stem cell-like state before differentiating into said organs (120). Long term culture of these systems, though, is difficult. Then, in 2009 Sato and Cleavers pioneered a long-term *in vitro* culture system where individual LGR5+ stem cells isolated from adult intestinal tissue can form miniature intestines in a dish called organoids under the right cocktail (121,122).

One significant advantage of this system over iPSCs is its ability to be maintained long term without compromising genomic integrity (123). Moreover, *in vitro* organoids' structure mimics the *in vivo* intestine with the intestinal lumen in the organoid's center with epithelial cells surrounding it. Small intestinal organoids (enteroids) present with a very distinct budding structure, with a defined crypt-villus structure. The villus domain, where differentiated cells reside, is near the organoids' center, while the crypt domain is toward the outside (Fig 2.1) (121). On the other hand, as colonic epithelium lacks villi *in vivo*, *in vitro* colonic organoids (colonoids) are more spheric, only budding under rare conditions (Fig 2.1). Similarly, tumor-derived organoids (tumoroids) are also spherical,

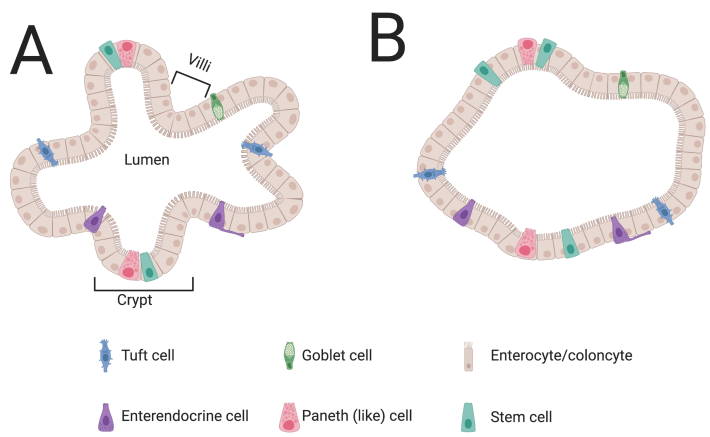

Fig 2.1. Difference between small intestine, colon, and tumor derived organoids. A) Small intestinal organoids maintain the crypt-villus structure with differentiated cells in the villi and stem and Paneth cells in the crypt. B) Colon and tumor organoids are more spherical, mimicking the absence of villi *in vivo*. *Figure created with biorender.com*

only budding under rare conditions (Fig 2.1). Although ongoing research is necessary, I hypothesize that budding in colonic and tumor organoids occur when the rate of division within the organoids is different, allowing for slow dividing cells to accumulate near the center of the organoids.

Unlike the *in vivo* intestine, there is a lack of the extracellular matrix; therefore, these organoids are cultured in a laminin-rich Matrigel to provide needed support. Moreover, the signaling and the immune microenvironment observed *in vivo* is lacking *in vitro,* providing a unique opportunity to investigate all aspects of intestinal biology ranging from development to diseased states, including cancer, through manipulation of culture conditions (124–126). For instance, varying concentrations of EGF, WNT3A, the Wnt agonist R- spondin, and the BMP antagonist noggin influence the presence and distribution of differentiated secretory and absorptive (121). Additionally, investigation of host-pathogen and immune-epithelial cell interaction happens through co-culture systems by adding immune factors to the base organoid culture (127–129). From a disease standpoint, there are currently high throughput screens of drugs and their interaction with a patient's tumors to determine which drug combination will result in the best response for a patient (130–133). Moreover, organoid systems have filled a void allowing the ability to study metastasis of cancer, once difficult to explore (134,135). Specifically, manipulation of tumoroids occurs through *in vitro* expression of mutations. These tumoroids can then be that can then be reintroduced to mice to study metastasis (134,135).

Model Organisms

Using humans for intestinal biology studies although, ideal, is not realistic. First, there are uncontrollable variables like mental state, smoking, or eating habits. Because the intestine is a barrier to the outside world, these variables will inevitably affect the intestine's inner workings and experiments (136). Consequently, numerous model organisms range from primates to *Caenorhabditis elegans*, but in my opinion, the mouse represents the best model system to study intestinal diseases in a systems biology manner. Mice are relatively inexpensive, have a vast experimental tool kit, and reflect many aspects of human immune and intestinal physiology. Additionally, numerous genetic and chemical models are available to study the different gut health and disease properties, including stem and non-stem cell function, inflammation, and cancer, warranting their substantial use to study intestinal biology (137). Here, I will touch on how mouse models are used to study intestinal damage, plasticity through lineage tracing, and the two specific Cre mice used in chapter 5: *Mist1-Cre*^{ERT2} and *Lrig1-Cre*^{ERT2}.

Damage in model organisms

Chronic intestinal damage and inflammation, typically seen as inflammatory bowel disease, increases colorectal cancer risk up to six times (138). Given this, studying intestinal damage and inflammation in mice is imperative. Coincidentally, there are two main categories to impose damage and increase inflammatory signaling in mouse models: genetically modified mice and chemically induced inflammation. Kontoyiannis *et*

al. produced a genetically modified mouse by inserting an AU-rich element into the Tnf-alpha gene, resulting in stabilizing the mRNA and overproduction of TNF-alpha protein. This modification results in small intestinal inflammation mimicking inflammatory bowel disease (139). A pitfall to this model is how quickly mice get sick, resulting in decreased ability to reproduce. Additionally, they commonly lack inflammation in the colon, and the amount of inflammation is heavily influenced by the microbe as we have seen less severe disease in different mouse facilities. Because of this, the most common way to induce damage to inflict an immune response in the colon is to utilize dextran sodium sulfate (DSS). DSS is a heparin-like polysaccharide dissolved in the drinking water (140). Although groups report damage throughout the colon, there is more extensive damage in the distal and mid colon than the proximal colon (141–144). It can also be used across numerous model organisms, although the mechanism of action can differ. For example, DSS causes direct damage to the basement membrane by being trafficked across the *Drosophila* intestinal enterocytes. On the other hand, in mice, DSS damages the junctional proteins holding neighboring epithelial cells together (145). DSS can also be overlaid on top of oncogenic mutations to drive tumorigenesis. For instance, the introduction of Azoxymethane, a procarcinogen that causes DNA damage, before DSS (AOM/DSS) induces colitis-associated cancer (140). Furthermore, as seen in Chapter V, DSS can be used after the initiation of the Cre-lox system to study the plasticity of cells in addition to tumorigenesis.

Cellular plasticity can be determined by lineage tracing

The experimental gold standard to determine a cell's multipotency is through lineage tracing using a genetically regulated label. Seminal work in this field used vital dyes or isotopically labeled cells to determine if they possessed stem capacity and the ability to give rise to progeny (146). A cell is multipotent when all the colonic epithelium lineages inherit the label, resulting in the long-term production of marked cell lineages in a given tissue that exhibits self-renewal.

This technique eventually advanced to the modern-day *Cre*-lox system, which allows for spatial and temporal control of lineage tracing activity. A particular cell of interest is genetically engineered to express an inheritable reporter, and a CRE recombinase enzyme is attached to a ligand-specific receptor. When the ligand, tamoxifen, is present, it binds the receptor, initiating CRE recombinase to translocate to the nucleus, recognize, and induce site-specific recombination typically at lox-P sites, sites on bacteriophage P1, which consists of 34 base pairs. Lox-P sites flank stop codons of a ubiquitously expressed gene, such as *Rosa26*. Excision of the STOP codon results in reporter expression inherited by the initial cell of interest's progeny. Long-term lineage tracing is then observed in stem cells' progeny 28 days post-CRE activation in the colon (Fig 2.2).

This system is regularly used under homeostatic conditions but more recently has been used under damage conditions to determine whether mature cell types regain stem cell function (Fig 2.2). Examples of damage-inducing agents commonly used are irradiation,

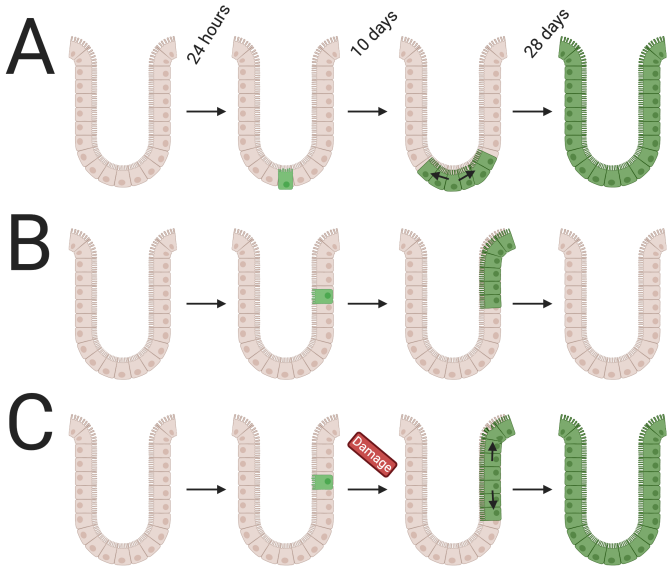

Fig 2.2. Lineage tracing is the gold standard to determine cellular plasticity. A) Stem cell mediated lineage tracing results in long term reporter expression while B) non-stem cell driven lineage tracing does not. C) Non-stem cell driven lineage tracing under damage results in long term lineage tracing. *Figure created with biorender.com*

diphtheria toxin, and dextran sodium sulfate (DSS). These agents are hypothesized to damage the available pool of actively dividing stem cells, allowing differentiated cell types to revert to a stem cell state and replenish the colonic epithelium.

Lineage tracing can also give insight into tumor-initiating potential. For instance, lineage tracing can be initiated from a known cell type after tumor formation to determine that particular cell's plasticity characteristics (147). This is not all-inclusive, though, as it is devised from candidate cell markers, and the tumor is an evolving system continually changing. Addressing this, mutation-induced marks during DNA replication suggest that only a small population of tumor stem cells largely self-renew and expand only when necessary (33).

For this work, we utilize lineage tracing in Chapter V to help characterize Mist1-expressing cells, specifically can Mist1 expressing cells exhibit multipotential stem cell capacity under homeostatic or damage conditions. Furthermore, we utilize the Cre-lox system to induce tumorigenesis from non-stem cells through *Mist1-Cre^{ERT2}* and stem cells through *Lrig1-Cre ^{ERT2}*.

Mist1-Cre^{ERT2}

Muscle, Intestine, and Stomach expression 1 (MIST1/ BHLHA15) is a 197 amino acid class A basic helix-loop-helix (bHLH) transcription factor that binds E-box regulatory elements at the -CANNTG- core consensus sequence as a homo- or heterodimer with

other bHLH proteins (148). MIST1 expression occurs in exocrine secretory cells like the Paneth cells of the small intestine, the acinar cells of the pancreas, or the zymogenic cells of the stomach (148). bHLH transcription factors are involved in the differentiation of several different kinds of tissue types, including the exocrine and endocrine pancreas, neuronal cells, B lymphocytes, and skeletal muscle (149). As the name suggests, these transcription factors contain two necessary regions: a basic region responsible for DNA binding and a helix-loop-helix region that supports protein dimerization (148).

Pin *et al*. published one of the first known mouse models studying *Mist1* and its *in vivo* roles and expression levels (150). They developed a *Mist1* knockout mouse through the use of *LacZ*, replacing the *Mist1* coding region. They found that *Mist1* is expressed early in the developing pancreas but is not necessary for cellular fate. Specifically, *Mist1* is essential for the complete maturation of acinar cells within the pancreas. In the absence of *Mist1*, there is disorganization of the acinar cellular structure and disrupted exocytosis signaling from acinar cells.

Although *Mist1* characterization occurred in the pancreas and stomach, at the start of the investigation shown in Chapter V, there was one study to our knowledge describing *Mist1* in the intestine as a possible secretory progenitor cell (148). Since then, Hayakawa *et al.* showed that MIST1 expressing cells are secretory progenitors that exhibit plasticity and serve as colonic tumor cells-of-origin under DSS damage (151). In Chapter V, we expand on this by exploring the TSCs within non-stem and stem cell-driven tumors. Specially, we reveal reduced stem capacity but increased class II antigen

presentation ability for non-stem cell (Mist1) driven TSCs compared with stem cell (Lrig1) driven TSCs, which resulted in a favorable immune microenvironment skewed towards active cytotoxic response in Mist1-driven tumors.

Lrig1-Cre^{ERT2}

Leucine-rich repeats and immunoglobulin-like domains 1 (LRIG1) is a transmembrane protein that contains an extracellular region of 15 leucine-rich domains and three immunoglobin domains (152). It is a negative regulator of the receptor tyrosine kinase signaling pathways ErbB. There are four members of the ErbB family of receptor tyrosine kinases (EGFR, ErbB2, 3, and 4) that LRIG1 will form a complex with, promoting receptor ubiquitination increasing basal and ligand simulated rates of receptor degradation (153). When binding of these RTKs occur, there is kinase activation, autophosphorylation, and triggering of multiple intracellular growth signaling pathways. Therefore, in cancer, LRIG1 is a tumor suppressor as upregulation of RTK pathways is a common occurrence.

LRIG1 is a quiescent stem cell in multiple organs, including the skin, hair follicle, and throughout the gastrointestinal system from the oral mucosa to the intestine (154–157). Specifically, in the intestine, there are different forms of Lrig1, each expressed in a different stem cell subset. The glycosylated form of Lrig1 is expressed in quiescent stem cells, while non-glycosylated Lrig1 expression occurs in actively dividing stem cells (39). We utilize Lrig1-Cre in Chapter V as a control for *Mist1-Cre^{ERT2}* lineage tracing and as the cell of origin for stem cell-driven tumorigenesis.

There is no one “silver bullet” to be able to fully characterize and understand a disease state. Each technique and model has its pros and cons, but when used together, they create a holistic understanding of the disease state. It is for this reason, I utilize a combination of systems biology techniques including single cell techniques like multiplexed imaging, DISSECT-CyTOF, and scRNA-Seq and *in vitro* organoids on multiple models to better understand the molecular characteristics and mechanistic insights of colorectal cancer.

Chapter III

IMPAIRED COORDINATION BETWEEN SIGNALING PATHWAYS REVEALED IN HUMAN COLORECTAL CANCER USING SINGLE-CELL MASS CYTOMETRY OF ARCHIVAL TISSUE BLOCKS

Recreated from: Simmons, AJ, **Scurrah, CR**, McKinley, ET, Herring, CA, Irish, JM, Washington, MK, Coffey, RJ, Lau, KS. Impaired coordination between signaling pathways revealed in human colorectal cancer using single-cell mass cytometry of archival tissue blocks. Sci Signal, 2016.

Introduction

A distinguishing feature of cancer and other diseases of dysregulated homeostasis is the expanded degree of intra-tissue cellular heterogeneity (21,158–160). Heterogeneous cell populations arise from an aberrant differentiation process where cells adopt semi-mature or new progenitor states on the Waddington landscape (161). Cellular heterogeneity has been demonstrated to present a significant challenge for treating these diseases, as therapies targeting one cell type may not be effective in another (162). Furthermore, rare cell populations, such as tumor stem cells (33,163), can adopt specialized, deleterious functions, including therapeutic resistance and metastatic ability (164–168). The

phenotypic state of a cell is governed by its genetics and environment; information from these sources are integrated by signaling and transcriptional networks into cellular behaviors. Investigations of cellular heterogeneity immensely benefit from single-cell analysis (169,170). However, it is not trivial to interrogate multi-pathway signaling activities at single-cell resolution since cellular signaling states can be destabilized outside the native tissue context (112,171,172).

A tried and true approach for preserving tissue morphology, and even cellular signaling states, is the procedure of formalin fixation coupled to paraffin embedding (FFPE). FFPE has been a standard practice in clinical analysis of tissues for nearly a century, and its ability to preserve tissues at ambient temperatures has been widely demonstrated (173). Due to the effectiveness of FFPE for preserving tissue, large repositories of clinically-annotated patient samples have been collected over the years. These banks are valuable resources for scientific insight when coupled to next-generation analytical approaches (174,175). Specifically, one of our goals is to conduct single-cell signaling analysis on FFPE tissues to address cellular heterogeneity. In order to achieve this, careful measures must be taken to undo the effects of formalin crosslinking in order to access cells, proteins, and nucleic acids for sophisticated analyses.

To comprehensively assess the phenotypic state of cells, evaluating the activity of a single pathway is not sufficient. Recently, several approaches have been described for measuring protein parameters from FFPE tissue in a multiplex fashion. The majority of these advances have been microscopy-based approaches for imaging tissue sections

that are ~5 µm in thickness. Approaches that enable multiplexing protein measurements include iterative rounds of fluorescence imaging (115,176–178) or metal-based detection (179,180). To achieve single-cell resolution, single or multiple cell border markers are used in conjunction with sophisticated image processing algorithms to extract single cell objects from images (181). Oblique sectioning and imperfect segmentation of partial cells can lead to inaccurate quantification, making these approaches semi-quantitative at best. Furthermore, either due to the iterative nature of cyclic immunofluorescence or rastering of samples for imaging mass-spectrometry, these approaches are low throughput and require multiple days/weeks of analysis to fully sample a given specimen. Given their space-resolving capabilities, we surmise that these techniques will be very powerful when combined with a primary strategy that confers feasibility to analyze a large number of samples with higher quantitative accuracy.

Our lab has recently reported a relatively rapid mass cytometry-based strategy for profiling signaling protein modifications at the single-cell level from solid tissues (112). This strategy, named DISSECT (Disaggregation for Intracellular Signaling in Single Epithelial Cells from Tissue), involves rapid, short fixation of freshly-isolated tissue to maintain native signaling in intact epithelia, and then a series of coupled procedures for staining and dissociation prior to mass cytometry analysis. The present study examines whether the same approach can be applied to FFPE-preserved tissues, given that FFPE preservation also involves the use of a formaldehyde fixative. In this report, we present an optimized procedure for dissociating single cells from FFPE-preserved solid tissues while maintaining their intact signaling states for mass cytometry analysis. We conducted

a proof-of-concept study on a small of cohort of human normal colon and colorectal cancer (CRC) FFPE specimens to sample signaling pathway heterogeneity at the single-cell level. Our results indicate that in normal colonic tissues, signaling pathways are organized into modules according to surface-to-crypt differentiation status. This modular organization is undermined in CRC. In addition, examining tumor samples in combination with genomic markers such as microsatellite and mutational status reveals distinct single-cell cancer phenotypes. This hypothesis-generating study demonstrates FFPE-DISSECT coupled to mass cytometry analysis on archival tissues, with the aim to extend to large cohort studies from solid tumor repositories for classify tumors in conjunction with genomic, transcriptomic, epigenomic, and proteomic characterization.

Results

A method to disaggregate single epithelial cells from archived tissue blocks that preserves cell type and signaling markers

We established a single-cell disaggregation approach for FFPE tissues (FFPE-DISSECT) combining heat-induced antigen retrieval with the whole mount staining and dissociation steps of DISSECT (Fig 3.1) (112,182). The steps of DISSECT were incorporated to enable epithelial signaling state preservation during the disaggregation process. We confirmed single-cell retrieval from FFPE tissues by both bright-field and autofluorescence imaging (Fig 3.2A, B). As with DISSECT, because tissue was kept intact until the end of the protocol, cell loss due to pre-analytic processing was minimized. Thus, we routinely yielded 5000-10000 cells (7503 +/- 2830 cells) per square millimeter of tissue

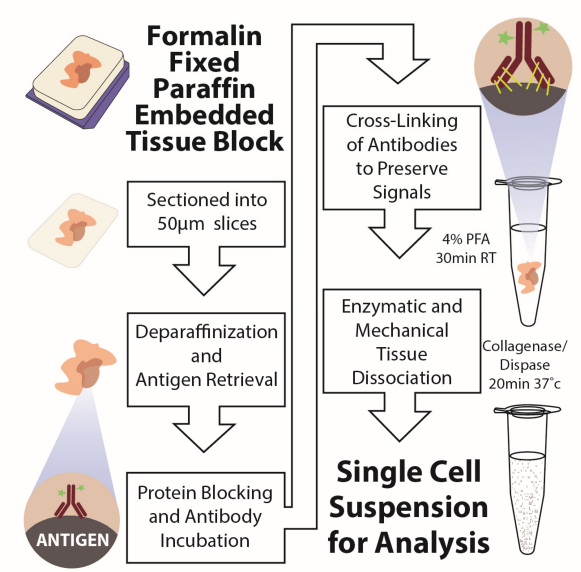

Fig 3.1. **Schematic of the FFPE-DISSECT process for preserving native epithelial signaling.** Thick curls were sectioned from FFPE blocks, antigen retrieved, and then processed following the steps of the DISSECT procedure.

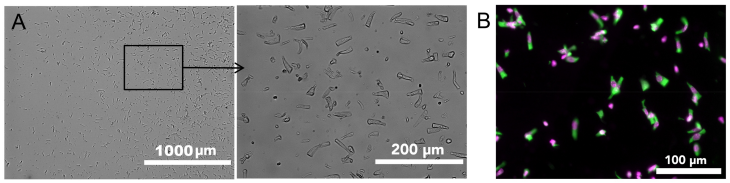

Fig 3.2. Imaging of single cell suspensions prepared by FFPE-DISSECT from embedded mouse intestinal tissue by (A) brightfield and (B) autofluorescence. Whole columnar epithelial cells isolated as single cells can be seen.

from a single 50 µm section. From the approximate area occupied per sample, we estimated that we yielded routinely on the order of a million cells per 50 µm tissue section.We first determined the preservation of cell identity markers for classifying epithelial cell types using our approach on murine intestinal tissue embedded by FFPE. Up until tissue dissociation, CLCA1 (chloride channel accessory 1) and CK18 (cytokeratin 18), markers for goblet and secretory cells, displayed substantial co-localization in whole-mount immunofluorescent staining, as expected (Fig 3.3). DCLK1 (doublecortin like kinase 1), a marker of tuft cells, labeled a separate population of CK18-/CLCA1- cells. Upon dissociation, these relationships remained intact in single epithelial cells (Fig 3.4A). Furthermore, the correct subcellular localization of proteins within cells can be visualized in the absence of scattered light or convolution from neighboring cells, i.e., CK18 staining of cytoskeletal structures and CLCA1 staining of mucous granules (Fig 3.4B). We then quantitatively verified marker co-expression using multi-parameter flow cytometry. CK18+ cells and CLCA1+ cells were independently gated. Back-gating of CK18+ and CLCA1+ cells revealed that they largely fell within an overlapping population, with CK18 marking a wider population of cells due to its ability to label other cells in the secretory lineage (Fig 3.4C, Fig 3.5A). These results demonstrated that cell types can be discerned in dissociated epithelial cells after FFPE-DISSECT.

More importantly, we determined that single cells retained their native signaling states post-dissociation using FFPE-DISSECT. To activate signaling pathways *in vivo*, we exposed the murine intestinal epithelium to TNF-α (tumor necrosis factor alpha) via intravenous administration, as we have done previously (183,184). Duodenal tissues from

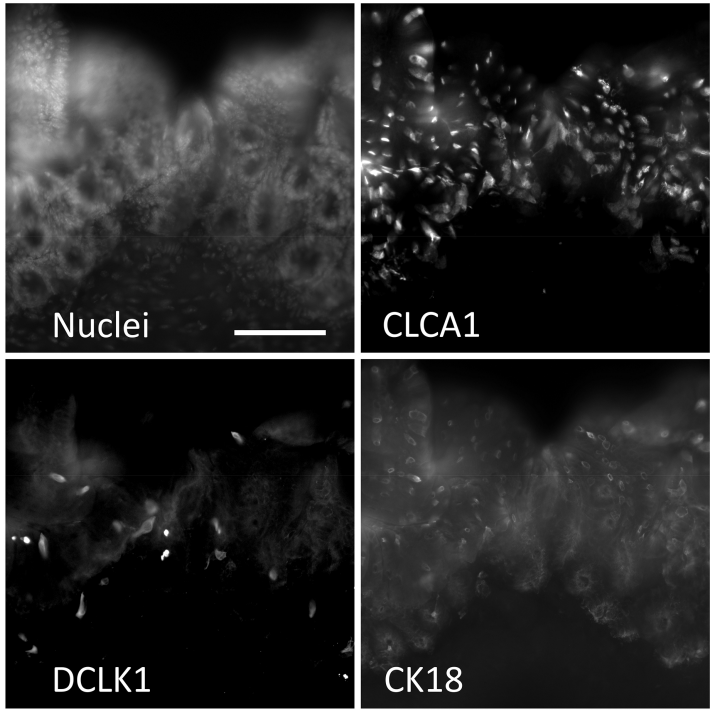

Fig 3.3. Whole mount staining of embedded mouse intestinal tissue prepared by FFPE-DISSECT prior to single cell disaggregation. Cell type markers (CK18, CLCA1, DCLK1) are imaged.

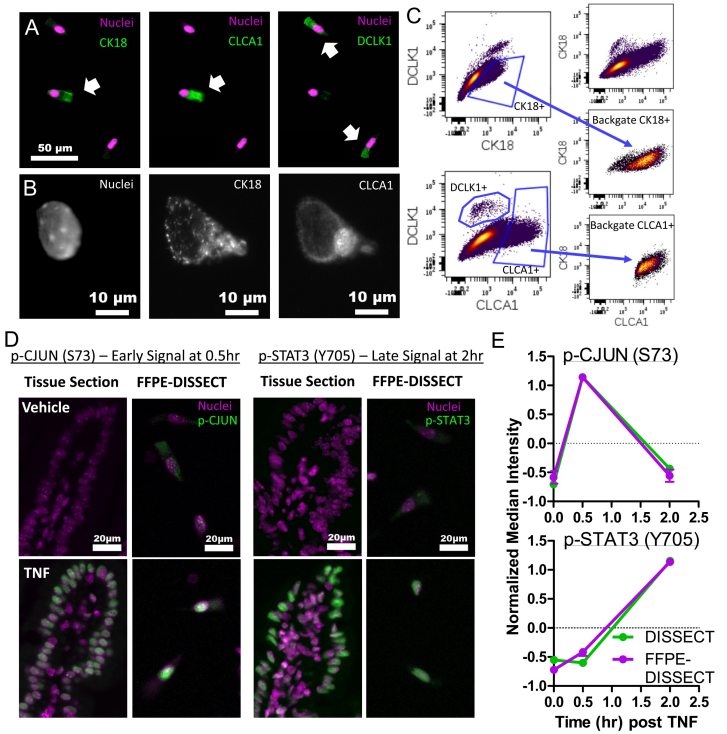

Fig 3.4. FFPE-DISSECT enables the identification of cell types and quantification of phospho-protein signaling activities. (A) IF imaging of dissociated cells from FFPE murine intestinal tissues prepared by FFPE-DISSECT, stained for cell type markers CK18, CLCA1, and DCLK1. (B) IF imaging of a single epithelial cell stained for nucleic acid, CK18, and CLCA1. (C) Flow cytometry bi-plots of the mouse ileum prepared by FFPE-DISSECT. Manual gating of goblet cells by CK18 and CLCA1, and tuft cells by DCLK1. CK18 and CLCA1 singular positive cells are back-gated to a bi-axial plot not used for the original gating to demonstrate that the cells comprise an overlapping goblet cell population. (D) IF imaging of intact FFPE intestinal tissues as 5 µm sections, compared to single cells prepared by FFPE-DISSECT, stained for p-CJUN (early signal) and p-STAT3 (late signal) in response to TNF-α at the appropriate time points. (E) Quantification of p-CJUN and p-STAT3 from single-cell suspensions generated from murine duodenal tissues, prepared immediately by DISSECT (green), or FFPE-embedded and then by FFPE-DISSECT (magenta), followed by flow cytometry. Median intensities calculated from single cell distributions are displayed for comparisons. Tissues were harvested at specified time points after TNF-α administration. Error bars represent standard error of the mean (SEM) from n=3 animals and data scales are Z-score values derived from mean centering and variance scaling of each set of time course experiment.

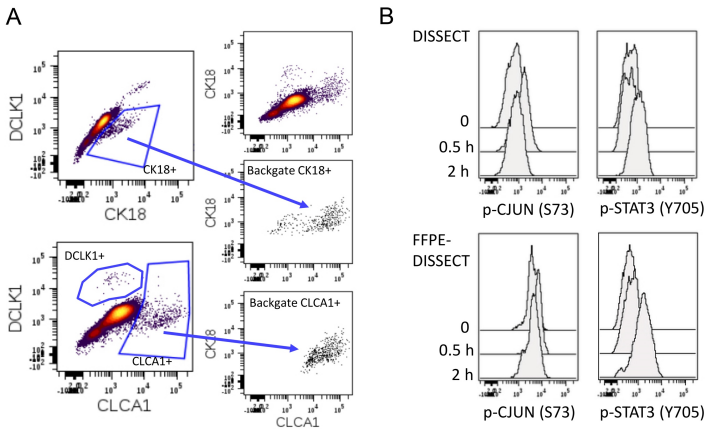

Fig 3.5. Fluorescence cytometry of samples prepared by FFPE-DISSECT. (A) Flow cytometry bi-plots of the mouse duodenum prepared by FFPE-DISSECT. Manual gating of goblet cells by CK18 and CLCA1, and tuft cells by DCLK1. CK18 and CLCA1 singular positive cells are back-gated to a bi-axial plot not used for the original gating to demonstrate that the cells comprise an overlapping goblet cell population. (B) Phospho-flow analysis of p-CJUN (early signal) and p-STAT3 (late signal) of the murine duodenum in response to TNF-α at specified time points. Single cells were prepared either immediately by DISSECT, or FFPE-embedded and then by FFPE-DISSECT.

the same animal were assessed as FFPE tissue sections or single cells generated by FFPE-DISSECT. Immunofluorescence imaging of tissue sections revealed that p-CJUN (an early TNF-α-induced signal) was upregulated at 0.5 hours post TNF-α exposure, and p-STAT3 (a late signal) was upregulated at 2 hours post TNF-α (Fig 3.4D). Imaging of single cell suspensions prepared by FFPE-DISSECT from serial sectioning of the same tissue block also revealed activation of the two signaling pathways at the appropriate time points compared to vehicle control (Fig 3.4D). We quantitatively compared signaling data from single-cell suspensions prepared by the validated DISSECT approach from freshly isolated tissues (112), with those prepared by FFPE-DISSECT from embedded tissues. Using the median intensity calculated from single cell distributions evaluated by flow cytometry (Fig 3.5B), we confirmed that both DISSECT and FFPE-DISSECT generated comparable signaling data for both p-CJUN and p-STAT3 with similar dynamics (Fig 3.4E). These results demonstrated the ability of FFPE-DISSECT in preserving signaling states of p-CJUN and p-STAT3 in single epithelial cells disaggregated from FFPE tissues.

Quantitative assessment of mass cytometry signaling analysis on FFPE tissue

In clinical practice, excised tissues requiring gross pathological examination may not be immediately fixed. Reports have documented the effects of ischemia and other factors on the degradation of protein signals in other tissues such as breast (185). To examine the effects of post-excision time outside of the body on signaling in the intestinal epithelium, we harvested intestinal tissues from mice, and fixed the tissue either immediately, 30 minutes post-excision, or 1 hour post-excision. Following standard FFPE processing, we

examined changes in constitutively active signaling pathways at homeostasis, for example, p-ERK mostly in the crypt and p-S6 mostly at the tip of the villus. We performed such analysis for a wide variety of markers across a wide breadth of signaling pathways that we will examine in human patients (Fig 3.6). For the intestinal epithelium, there was minimal degradation of these signals for up to one hour from the time of harvesting the tissue. We further verified that the length of fixation time, for up to 72 hours, has minimal effect on the detection of representative signaling markers in FFPE (Fig 3.7).

As we have successfully assessed the validity of FFPE-DISSECT on selected signaling markers, we next sought to systematically and quantitatively validate our approach over a broad range of signaling pathways. We used mass cytometry as a multiplex technique to quantify a broad range of signaling markers from single cell suspensions, comparing between FFPE-DISSECT preparations from embedded tissues and DISSECT preparations from fresh tissues. Single-cell signaling data obtained by DISSECT have previously been rigorously validated against those generated by conventional bulk approaches such as immunoblotting (112). Mice were stimulated with TNF-α and duodenal tissues were harvested over a time course to sample a quantitative range of signaling levels. Harvested tissues were then divided: 1) to either be freshly processed by DISSECT, or 2) to be embedded and then processed by FFPE-DISSECT. Mass cytometry analysis was performed on both sets of tissues (isolated from the same animal) using the same panel of metal-conjugated reagents for signaling markers (Table 3.1). The normalized median intensities of distributions of signaling markers were used as a direct comparison between DISSECT and FFPE-DISSECT preparations (Fig 3.8). The

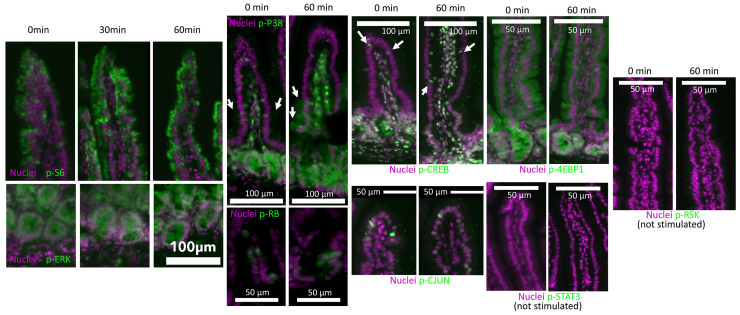

Fig. 3.6. Signals are preserved for up to 1-hour post-excision. Immunofluorescence imaging of basal signals for all phospho-protein signaling markers used in the human study (Table 3.3) in FFPE murine tissues with a post-excision time of up to one hour for simulating possible tissue preparation conditions in the human study. Murine duodenal tissues were harvested, and then either fixed immediately, or stored in RPMI for 30 or 60 minutes (as per Cooperative Human Tissue Network standard operating procedure) prior to fixation and FFPE processing. Crypts, villi, or both displayed according to signal localization. Arrows represent individual positive cells. Images are representative of 3 experiments. Scale bars as indicated.

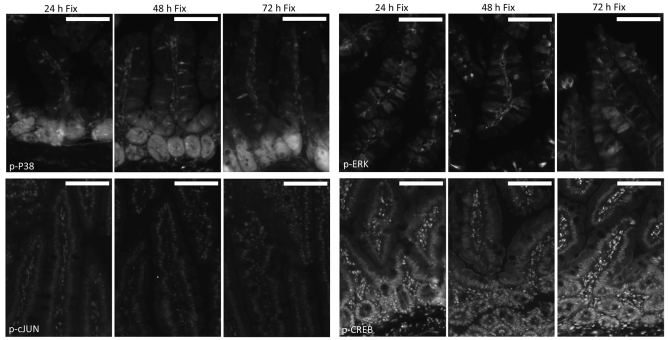

Fig. 3.7. Fixation time does not affect signaling marker detection in FFPE. IF imaging of murine duodenal tissues stimulated by TNFα for 30 mins that were in fixative for the indicated time. Representative cytoplasmic (p-P38, p-ERK) and nuclear (p-CJUN, p-CREB) signals.

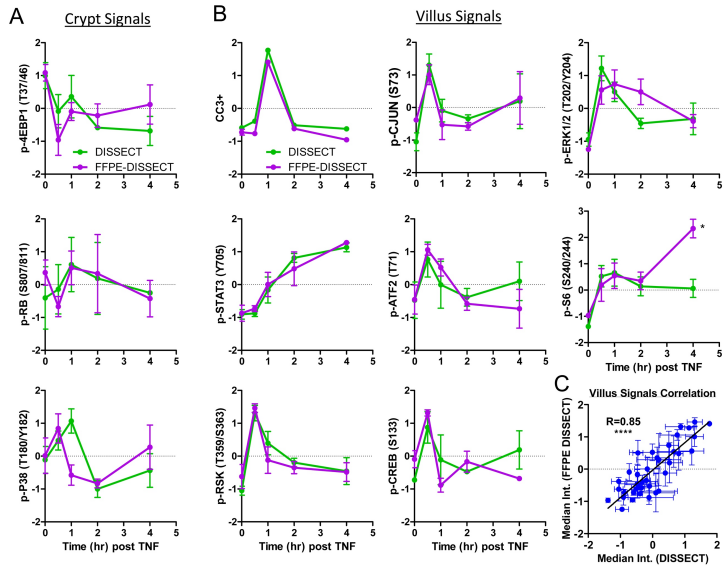

Fig 3.8. **Comparison between mass cytometry data generated by FFPE-DISSECT and the validated DISSECT method on the same intestinal tissue.** Murine duodenal harvested from specified time points post TNF-α administration were split in two, with one half processed immediately by DISSECT (green), and the other half FFPE-embedded and then processed by FFPE-DISSECT (magenta). Both sets of tissues were analyzed by mass cytometry with the same cross-reacting signaling antibody panel. Dynamic signals are presented as TNF-α stimulation time courses, and enriched in either (A) crypts or (B) villus. (C) Correlation analysis combining all villus signaling markers, comparing mass cytometry data generated by DISSECT against FFPE-DISSECT. Quantitative data from different time points were used to generate a range of variation for correlation analysis. Error bars represent SEM from n=3 animals and data scales are Z-score values derived from mean centering and variance scaling of each set of time course experiment. * P ≤ 0.05, ** P ≤ 0.01, *** P ≤ 0.001, **** P ≤ 0.0001

DISSECT approach was optimized for scraped mucosa, and thus, the data generated were enriched for villus signals. In contrast, tissue sectioning enabled sampling of the entire epithelium for FFPE-DISSECT. Thus, crypt enriched signals, such as p-RB, p-4EBP1, and p-P38 (Fig 3.9A), did not show good concordance between the two methods due to the de-emphasis of crypt signals in DISSECT preps (Fig 3.8A). Crypt proliferative signals (p-4EBP1 and p-RB) generated by FFPE-DISSECT showed an initial dip and a subsequent increase after TNF-α exposure, mirroring the proliferative response of the intestinal epithelium to TNF-α (184). Examining villus-enriched signals, a strong correlation between data generated by DISSECT and FFPE-DISSECT was observed (Fig 3.8B). Quantitative correlation analyses using villus-enriched signals resulted in a highly significant correlation (R=0.85, p<0.0001) of mass cytometry data generated by DISSECT against FFPE-DISSECT (Fig 3.8C). Including crypt-enriched signals resulted in a slightly lower correlation (R=0.76, p<0.0001) (Fig 3.9B). We further verified FFPE-DISSECT and compared median signals obtained to those obtained by IF imaging (Fig 3.9C, D) and quantitative immunoblotting (Fig 3.9E, F), comparing across different cohorts of mice similarly stimulated with TNF-α as a time course. Again, FFPE-DISSECT compared favorably. By using FFPE-DISSECT in conjunction with mass cytometry, valid, single-cell level signaling data can be obtained from embedded epithelial tissues.

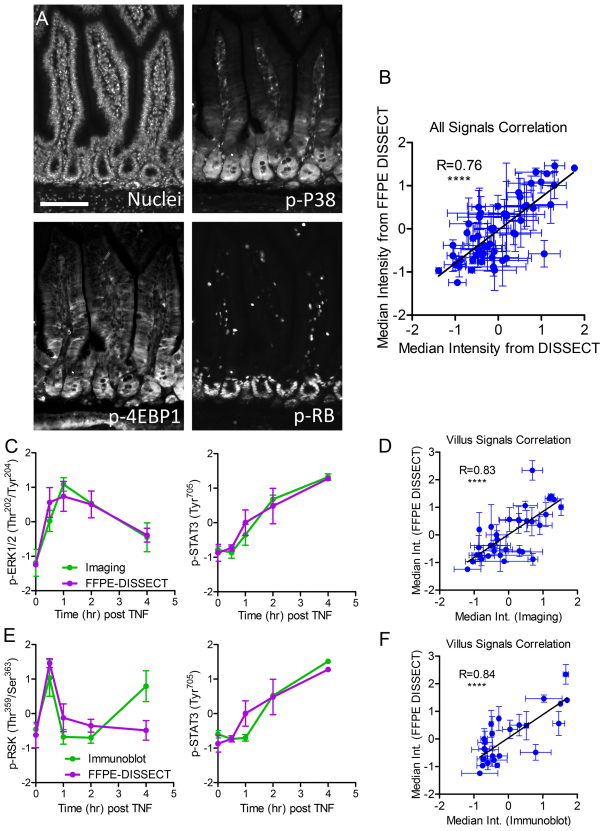

Fig 3.9. Villus signals are more enriched in DISSECT, whereas crypt signals are better represented in FFPE-DISSECT. (A) IF imaging of p-P38, p-4EBP1, p-RB at homeostasis in murine duodenal FFPE sections. (B) Correlation analysis combining all signaling markers (both villus and crypt), comparing mass cytometry data generated by DISSECT against FFPE-DISSECT. Error bars represent SEM from n=3 animals and data scales are Z-score values derived from mean centering and variance scaling of each set of time course experiment.

Cell type-specific signaling reveals increased secretory cell sensitivity to basal and TNF-α-induced signaling

In addition to examining the average over epithelial distributions, we sought to determine how different cell populations in the small intestine respond to TNF-α using our single-cell of induction (183,184,186) . Our previous study demonstrated that the onset of apoptosis occurs at 1 hour after intravenous administration of exogenous TNF-α, and thus, mass cytometry data enabled by FFPE-DISSECT were obtained from duodenal tissues at this time point. t-distributed stochastic neighbor embedding (t-SNE (116)) analysis on 15-channel signaling and cell identity data revealed a CC3+ population of apoptotic epithelial cells (Fig 3.10A, for markers - Table 3.1). This dying cell population has a distinct signaling signature, including the downregulation of p-ERK and upregulation of p-P38 (Fig 3.10A, B, and replicates: Fig 3.11), as reported previously. We previously showed that p-ERK upregulation in neighboring cells surrounding the apoptotic cell is a contact-dependent survival mechanism preventing large-scale barrier defects in the gut (112). We then further evaluated cell-type-specific signaling by integrating signals from the entire TNF-α time course in cell populations expressing cell-type-specific markers (CLCA1+ goblet cells, CHGA+ - chromogranin A enteroendocrine cells, CK+/CLCA1-/CHGA- enterocytes). Goblet cells generally have increased signaling across most pathways assayed, whereas enteroendocrine cells selectively upregulate certain pathways when compared to enterocytes (Fig 3.10C and Fig 3. A). The relative differences in signaling between cell types can be reproduced by DISSECT on freshly isolated tissue, again confirming the validity of our new approach (Fig 3.10C and Fig 3.S8A). Furthermore, the upregulation of p-ERK, p-ATF2, and p-4EBP1 in goblet cells, and of only p-ATF2 in

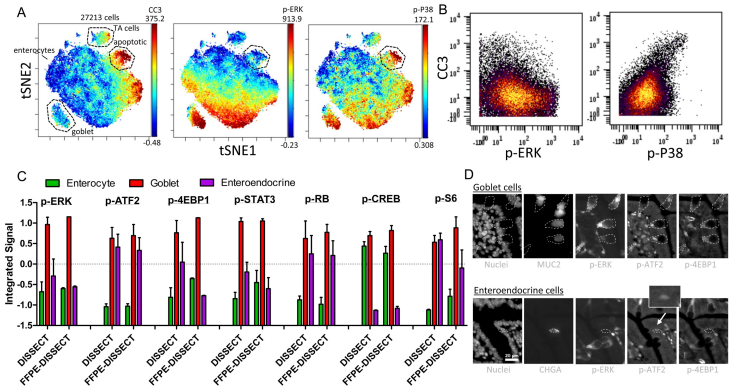

Fig 3.10. **Cell-specific signaling in the murine duodenal epithelium.** (A) t-SNE analysis of mass cytometry data from the mouse duodenum exposed to TNF-α for 1 hr, prepared by FFPE-DISSECT. Color overlaid represents the relative quantification of cleaved caspase 3, p-ERK, and p-P38 events, respectively. Labelled cells: apoptotic – CC3+ (3.07%), TA cells – p-4EBP1+ (4.13%), goblet – CLCA1+ (5.44%), enterocytes - CKAE+, CLCA1-, CHGA-. Numbers on right axis represent min and max value of the color scale. (B) Bi-plots of CC3 with p-ERK or p-P38, demonstrating negative correlation in the former and positive correlation in the latter. (C) Signaling specific to epithelial cell types (enterocyte-CKAE+, CLCA1-, CHGA-, goblet – CLCA1+, enteroendocrine – CHGA+) calculated by integrating signal values over the entire TNF-α time course, comparing mass cytometry data generated by DISSECT against FFPE-DISSECT. Error bars represent SEM from n=3 animals and data scales are Z-score values derived from mean centering and variance scaling over data values for the three cell types for each method. (D) IF imaging to confirm cell type-specific signals (p-ERK, p-ATF2, p-4EBP1) at homeostasis.

Epitope	Clone
CKAE1/3	CKAE1/AE3
p-4EBP1 (T37/46)	236B4
p-RB (1207/811)	D20B12
p-S6 (S240/244)	D68F8
p-ATF2 (T71)	11G2
p-P38 (T180/Y182)	D3F9
p-STAT3 (Y705)	D3A7
p-CJUN (113)	D47G9
p-RSK (T359/S363)	D1E9
p-CREB (S133)	87G3
p-ERK1/2 (T202/Y204)	D13.14.4E
p-EGFR (Y1068)	D7A5
ChrgA	Polyclonal
CLCA1	EPR12254-88
C-Caspase 3 (N-175)	Polyclonal

Table 3.1. Mouse antibody reagent panel

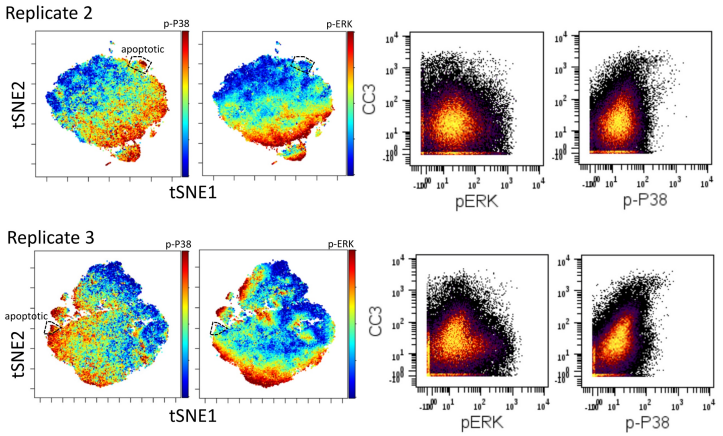

Fig 3.11. Replicates over multiple animals depicting relationships between apoptosis and signaling pathways using t-SNE and bi-plots.

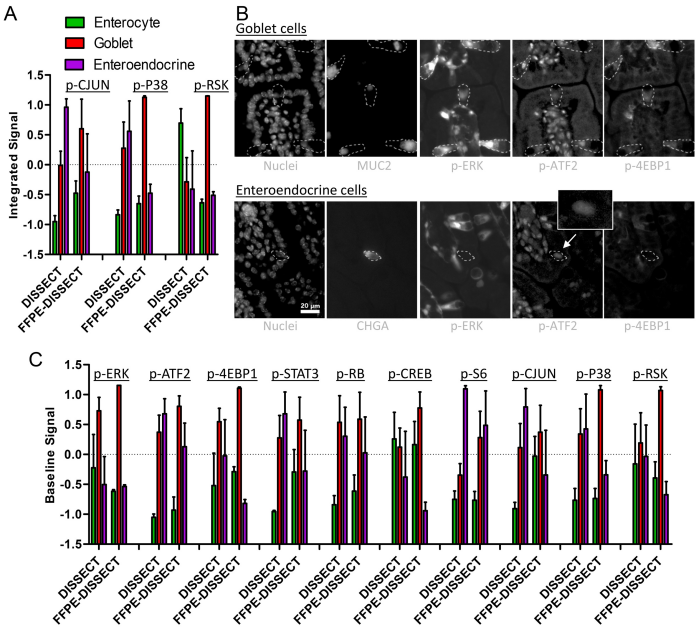

Fig 3.S8. Cell type-specific signaling in the murine duodenal epithelium. (A) A subset of signals specific to epithelial cell types (enterocyte- CK20+, CLCA1-, CHGA-, goblet – CLCA1+, enteroendocrine – CHGA+) calculated by integrating signal values over the entire TNF-α time course, comparing mass cytometry data generated by DISSECT against FFPE-DISSECT. (B) Replicate IF imaging to confirm cell type-specific signals (p-ERK, p-ATF2, p-4EBP1) at homeostasis. (C) Baseline signals specific to epithelial cell types, comparing mass cytometry data generated by DISSECT against FFPE-DISSECT. Error bars represent SEM from n=3 animals and data scales are Z-score values derived from mean centering and variance scaling over data values for the three cell types for each method.

enteroendocrine cells was corroborated by immunofluorescent imaging (Fig 3.10D and Fig 3.S8B). These differences were also observed at basal level without TNF-α stimulation, perhaps demonstrating the importance of these signaling pathways in the identity of these cells (Fig 3.S8C). Here, we focus on the role of p-ERK in goblet cell identity.

MEK-ERK signaling is canonically activated by upstream Ras activation. The members of the Ras family of small GTPases (KRAS4A, KRAS4B, NRAS, HRAS) share N-terminal sequence identity and *in vitro* effector binding, but have distinct subcellular membrane distribution due to differences in post-transcriptional modifications in their C- terminal hypervariable regions (187). Thus, different Ras isoforms can engage in different signaling effectors, such as Raf, PI3K, and Ral, which can lead to different phenotypic manifestations. Mutationally activated KRAS in the intestinal epithelium induces hyper-proliferation, whereas active NRAS does not (188). Given that both activated KRAS(188) and NRAS(186,189) in the intestine can sensitize downstream MEK-ERK towards activation in different circumstances, we surmise that MAPK-induced goblet cell identity may be a common feature of Ras activation. *Villin-Cre* driving an activated KRAS ($KRas^{LSL\text{-}G12D/+}$) allele in the intestinal epithelium increased the number of goblet cells (Fig 3.13), but also induced hyperplasia as documented previously (188,190). The same induction scheme with activated NRAS ($NRas^{LSL\text{-}G12D/+}$) did not result in hyperplastic growth. Surprisingly, NRAS activation led to a similar increase in goblet cells (Fig 3.13), a phenotype that has not been connected to NRAS activation until now. Furthermore, in accordance with the role of p-ERK in promoting enterocyte survival, goblet cells have x

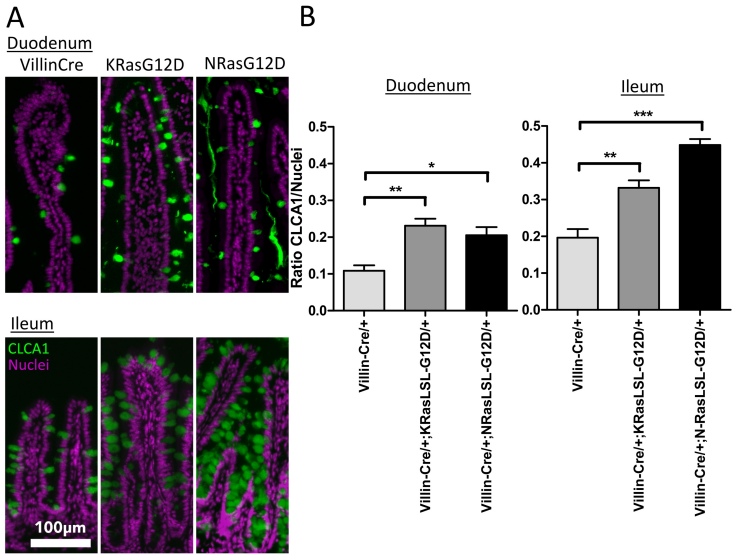

Fig 3.13. RAS induction of MEK-ERK signaling induces goblet cell identity. (A) IF imaging of goblet cells by CLCA1 staining in *Villin-Cre*/+ control, *Villin-Cre*/+; *KRas*$^{LSL\text{-}G12D/+}$, and *Villin-Cre*/+; *NRas*$^{LSL\text{-}G12D/+}$ murine duodenal and ileal epithelial. (B) Quantification of the ratio of area occupied by CLCA1 staining versus nuclear staining in the villus (with a correction factor for the size of a goblet granule against the size of a nucleus). Error bars represent SEM from n=3 animals. * P ≤ 0.05, ** P ≤ 0.01, *** P ≤ 0.001, **** P ≤ 0.0001

enteroendocrine cells was corroborated by immunofluorescent imaging (Fig 3.10D and Fig 3.S8B). These differences were also observed at basal level without TNF-α stimulation, perhaps generating meaningful single-cell signaling data from embedded tissues.

Human CRCs present with dysregulated signaling and differentiation

One of the goals for FFPE-DISSECT application to embedded tissue is to enable single-cell signaling analysis on human patient tissue repositories stored as FFPE blocks. To that end, we procured a cohort of clinically-annotated colonic tissue samples from the Western Division of the Cooperative Human Tissue Network (CHTN), situated at the Vanderbilt University Medical Center. After discarding samples with low cellularity (<10%), our cohort included 7 normal colon control samples and 13 (6 MSI and 7 MSS) primary CRC samples. Control colon samples were collected from a variety of conditions unrelated to CRC (e.g., adjacent normal from diverticulitis). According to our time-to-fixation optimization, we only selected samples with a post-excision time of <1 hour, a parameter tracked by CHTN. Clinical and pathological attributes of the CRCs, including the microsatellite and KRAS/BRAF mutational status, were summarized (Table 3.2). A board-certified pathologist further examined the hematoxylin & eosin stains of these samples to confirm tumor histology (Fig 3.14). A panel of cross-reacting antibodies against signaling proteins and cell type markers were prepared for mass cytometry analysis (Table 3.3). These reagents have been verified to stain human tissues by immunofluorescence imaging (Fig 3.15), and to be on-target previously (112). Mass

ID	Age	Sex	Metastatic	Stage	Grade	KRAS	BRAF	MSI status	Tumor Site	PET (h)
33468	57	M	Yes	IIIC	G2	U	U	MSS	Sigmoid	1
33469	75	M	No	II	G2	U	U	MSS	Cecum and ileocecal valve	0.5
33470	56	F	Yes	IV	G3	G12V	WT	MSS	Cecum	1
33471	81	F	No	IIA	G2	U	V600E	MSI-H	Left colon	0.5
33472	47	M	Yes	III	G3	U	V600E	MSI-H	Cecum	0.5
33473	80	M	U	IIA	G2	WT	WT	MSS	Sigmoid colon	0.5
33474	78	F	U	IIA	G2	U	V600E	MSI-H	Hepatic flexture	0.5
33475	58	M	Yes	IIIB	G2	U	U	MSS	Right colon	0.5
33476	65	M	Yes	IV	U	U	WT	MSI-H	Cecum	0.75
33478	35	M	Yes	IIIC	G2	WT	U	MSS	Sigmoid colon	0.5
33479	40	M	U	IIA	G2	U	WT	MSI-H	Hepatic flexture	0.5
33482	71	M	Yes	IIIC	G2	G12C	WT	MSS	Lower pole	0.5
33483	82	M	Yes	IIIB	G3	U	V600E	MSI-H	Right colon	0.5

Table 3.2. Summary pathological characteristics of human colon cancer samples

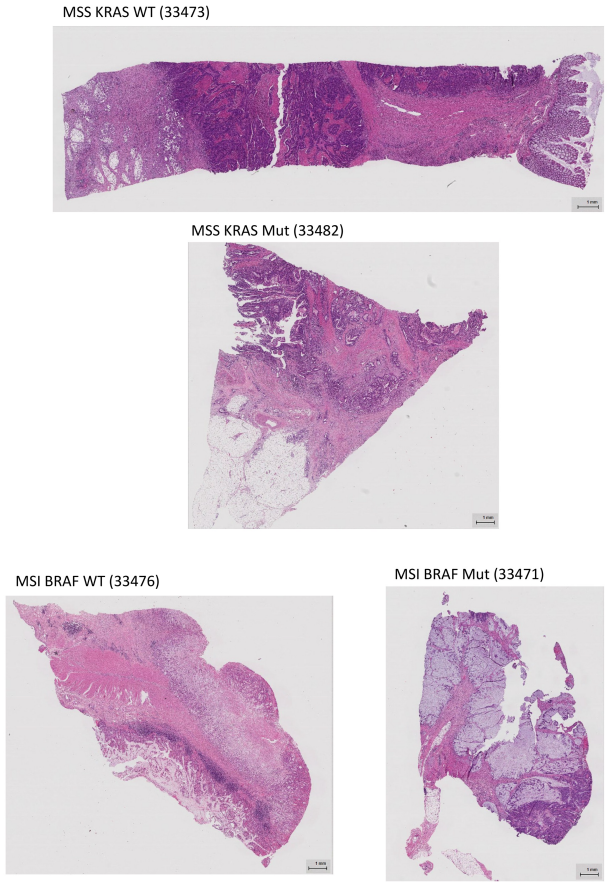

Fig 3.14. Hematoxylin and eosin of MSS and MSI CRCs showing tissue areas occupied by tumors.

Epitope	Clone
CK18	C-04
CD117 (KIT)	104D2
p-EGFR (Y1068)	D7A5
p-4EBP1 (T37/46)	236B4
p-RB (S807/811)	D20B12
p-S6 (S240/244)	D68F8
CD8	C8/144B
Vimentin	D21H3
p-P38 (T180/Y182)	D3F9
p-CJUN (S73)	D47G9
p-STAT3 (Y705)	D3A7
p-RSK (T359/S363)	D1E9
Pan-CK	C11
p-CREB (S133)	87G3
p-ERK1/2 (T202/Y204)	D13.14.4E
Ki-67	B56
CHGA	Polyclonal
CK20	D9Z1Z
CLCA1	EPR12254-88
C-Caspase 3 (N-175)	Polyclonal

Table 3.3. Human antibody reagent panel

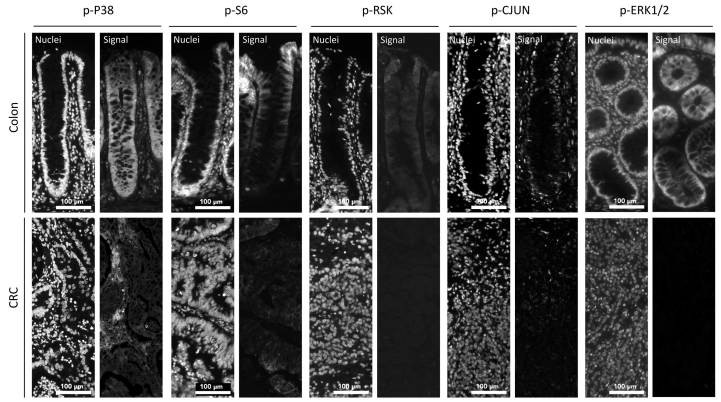

Fig 3.15. Signaling in human normal colon and CRC. IF imaging of p-P38, p-S6, p-P90RSK, p-CJUN, and p-ERK1/2, with full representation of the surface-to-crypt axis.

cytometry following FFPE-DISSECT was performed on this cohort of human colon and CRC samples. Because actual tumors comprised only of a minor fraction of tissues resected (Fig 3.14), we decided to focus specifically on epithelial/cancer cells which are marked and can be gated by PCK (pan-cytokeratin) (Fig 3.16A, B). From mass cytometry data, we quantitatively assessed the percentage of different epithelial cell types in various differentiation states from normal colon versus CRC tissues within the epithelial compartment. As expected, terminally differentiated cells (CK20+ - cytokeratin 20) were significantly decreased in CRC compared to normal colon (Fig 3.17A and Fig 3.16A). Furthermore, goblet cells (CLCA1+) and enteroendocrine (CHGA+) cells were also significantly decreased (Fig 3.17B, C and Fig 3.16C). However, we discovered that a portion of protein markers representing signaling pathway activation were downregulated in CRC (Fig 3.17D and Fig 3.15). This result was paradoxical given that cancer is mostly driven by mutations that ultimately activate signaling pathways. However, there is evidence from *in vivo* studies that demonstrate the upregulation of negative feedback mechanisms when MAPK signaling pathways are mutationally activated only in the context of CRC (191). For instance, mutational activation of KRAS in CRC paradoxically results in the downregulation of p-ERK due to the upregulation of MKP3 ERK phosphatase (188). Furthermore, as shown in our mouse studies, there are substantial signaling activities in differentiated cells and these cells are largely absent in CRC (Fig 3.10C, D). To verify that the reduction in signaling of these pathways did not result from poor penetration of fixative, we were able to detect similar stain intensities of multiple signaling markers in the peripheral and central regions of the same tumors, for tumors

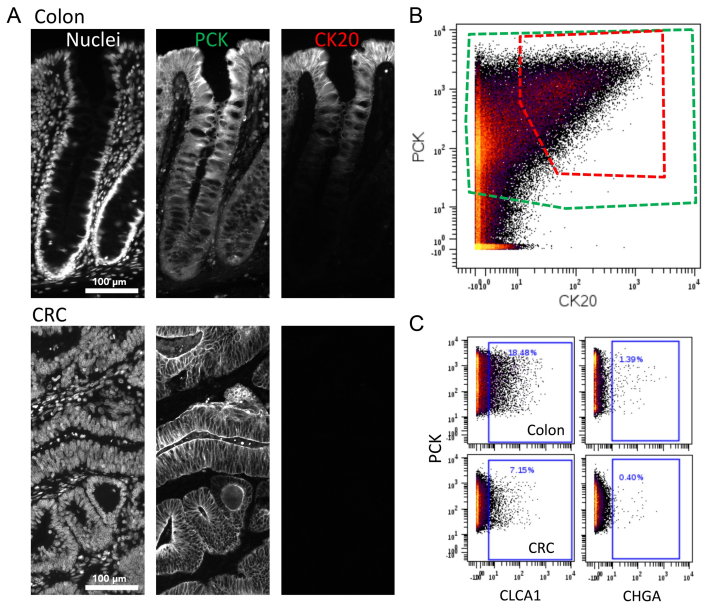

Fig 3.16. Differentiation in human normal colon and CRC. (A) IF imaging of PCK, which marks all epithelial cells, and CK20, which marks differentiated epithelial cells in normal colon and CRC. (B) Mass cytometry-generated bi-plot of PCK vs. CK20 on normal colon overlaid with cell density. Schematic of epithelial (tumor) cell gating by PCK (green) and CK20 (red) for further analysis. (C) Manual gating of goblet cells by CLCA1 and enteroendocrine cells by CHGA for normal colon and CRC.

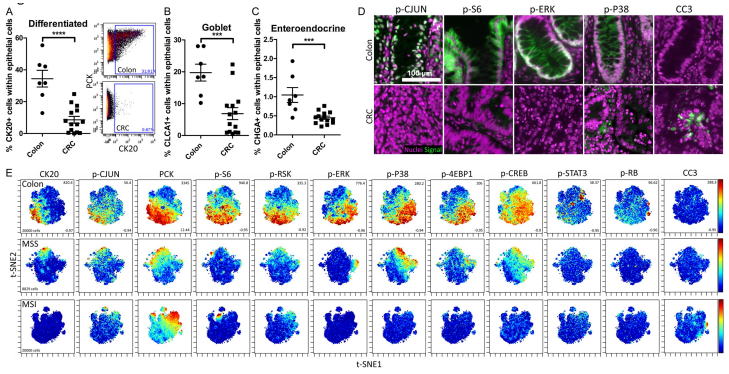

Fig 3.17. Mass Cytometry analysis of human colorectal cancer specimens prepared by FFPE-DISSECT. Percentage of (A) CK20+ fully differentiated epithelial cells, (B) CLCA+ goblet cells, and (C) CHGA+ enteroendocrine cells in the normal human colon compared to CRC. Error bars represent SEM from n>7 different patient specimens. Inset depicts manual gating of differentiated cells by CK20. (D) IF imaging of signaling markers (p-CJUN, p-S6, p-ERK, p-P38, CC3) comparing normal colon and CRC. (E) t-SNE mapping of mass cytometry data generated from human colon, MSS or MSI CRC specimens, overlaid with signaling and selected differentiation markers. Numbers on right axis represent min and max value of the color scale. The same scales were used between all samples. Proportional downsampling to 20,000 cells was performed for more equivalent representation since some samples have a small representation of actual tumor cells. On average 60,000 cell events were collected per sample.

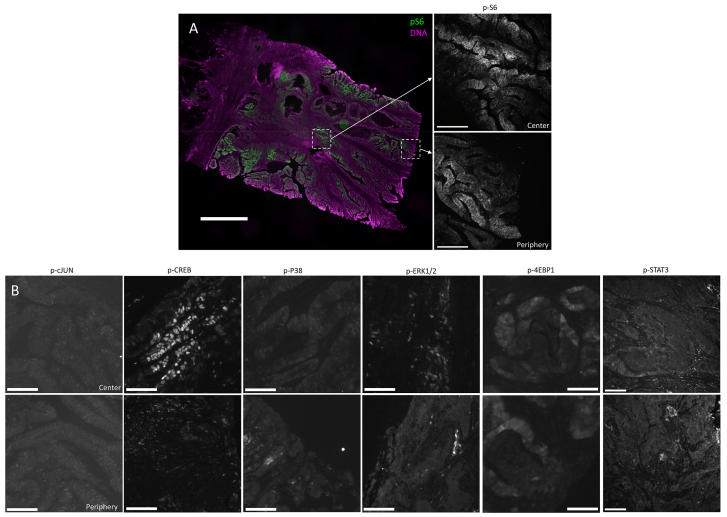

Fig 3.18. Evidence of fixative penetration. (A) Demonstration of IF imaging of whole tumors at the periphery or center. Stitched image and staining for p-S6. (B) Representative images of signaling markers detected at the periphery and the center of the same tumors.

displaying positive signals (Fig 3.18). These results, all obtained from one sampling of tissue, suggested that differentiation is impaired in CRC, and these changes are associated with reduced signaling through certain pathways.

Modular organization of signaling pathways is disrupted in human CRC

Using t-SNE analysis to visualize multidimensional single-cell data from normal and CRC tissues, we observed defined organization of signaling pathways in normal colon tissues at single-cell level. The activation level of signaling proteins in different pathways formed distinct patterns on t-SNE maps (Fig 3.17E, for markers – Table 3.3); in one specimen, signaling markers formed a counter-clockwise arrangement in association with surface-to-crypt status marked by cytokeratins. These patterns can be broken down into a modular architecture: p-CJUN correlated with CK20+ differentiated cells, PCK, p-S6, and p-RSK shared similar expression patterns, and p-ERK, p-P38, p-4EBP1, and p-CREB formed another module correlating to less differentiated crypt cells. These modules can also be revealed by calculating the pairwise correlation between signaling markers over individual cells, and using correlative distances for hierarchical clustering per sample (Fig 3.19A). Qualitatively, the components within each module were consistent between normal colon samples, signifying robust organization of signaling pathways between cellular populations. The level of correlation between signaling pathways over single cells was reduced in both MSS and MSI CRC samples, signifying the usage of heterogeneous modes of signaling pathway regulation between individual cells in a tumor (Fig 3.17E, Fig

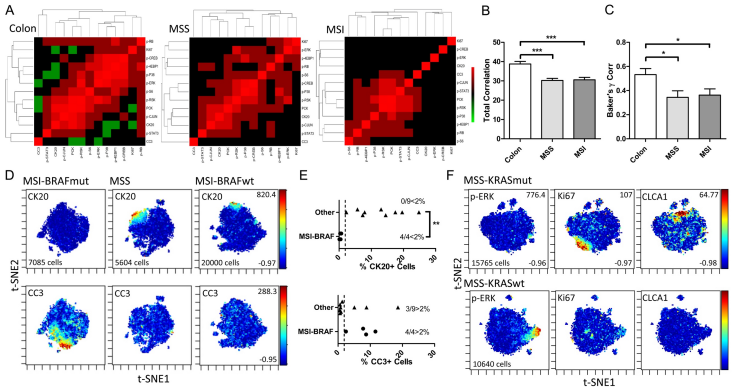

Fig 3.19. Insights into the heterogeneous organization of signaling pathways in CRC from single-cell data. (A) Heatmap and hierarchical clustering derived from pairwise correlative distances between signaling markers calculated over all single cells in a sample. A high pairwise correlation signifies two pathways are regulated in the same way in all cells. Representative colon, MSS, and MSI samples are shown. (B) The mean value of all pairwise correlations between signaling markers calculated per sample, comparing between normal colon, MSS, and MSI. Error bars represent SEM from n>6 different patient specimens. (C) Baker's gamma correlation coefficient comparing the similarity between hierarchical clustering trees computed between all samples within each group (colon, MSS, MSI). Error bars represent SEM from n>6 different patient specimens. (D) t-SNE maps of mass cytometry data generated from a MSI-BRAFV600E mutant tumor compared to MSS or MSI-BRAF wild type tumors overlaid with CK20 and CC3. Numbers on right axis represent min and max value of the color scale. The same scales were used between all samples. (E) Percent CK20+ or CC3+ cells comparing MSI-BRAFV600E mutant tumors compared to tumors of other genotypes. Dotted line represents the 2% threshold, and inset is the number of samples passing the threshold. (F) t-SNE maps of mass cytometry data generated from a MSS-KRASG12 mutant tumor compared to a MSS-KRAS wild type tumor overlaid with p-ERK, Ki67, and CLCA1. * P ≤ 0.05, ** P ≤ 0.01, *** P ≤ 0.001, **** P ≤ 0.0001

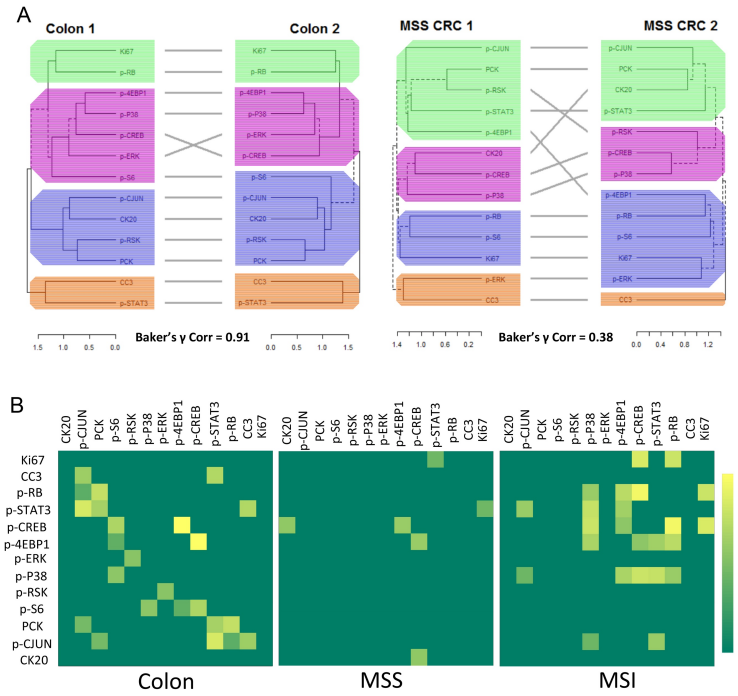

Fig 3.20. Analysis of the organization of signaling pathways in human specimens. (A) Pairwise comparisons between hierarchical clustering trees with calculated Baker's gamma correlation coefficient for normal colon and MSS CRC. Colored blocks represent signaling modules as determined by clustering on signaling markers. (B) Heatmaps generated by pairwise correlations between signaling markers calculated over all samples, disregarding single-cell data but instead using the median values generated from single-cell distributions. Heat represents correlation >0.7.

3.18A). Furthermore, modular organization of signaling pathways from hierarchical clustering was not preserved from sample to sample in CRC, implying significant intertumoral heterogeneity in signaling pathway regulation (Fig 3.20A). In place of qualitative assessment of signaling heterogeneity on a sample-per-sample basis, we quantitatively assessed intratumoral and intertumoral heterogeneity over all the samples. We evaluated signaling markers measured in a pairwise fashion, with the notion that high by all cells. On a per sample basis, this metric can be represented by the total intensity on a correlative distance heat map (Fig 3.19A). Normal colon samples have significantly higher total correlation compared to MSS and MSI CRC samples, denoting the loss of signaling regulation homogeneity between cells in CRC (Fig 3.19B). We quantitatively evaluated intertumoral signaling heterogeneity by assessing the degree by which signaling modules are reused between samples. For this, we took advantage of tools built previously to assess the similarity between dendrograms to evaluate the degree similarity between the structures of hierarchical clustering trees (192). We used the Baker's Gamma Correlation coefficient (193), a metric that is insensitive to the height of the branches but only to the position of each branch, to calculate pairwise similarities between hierarchical trees generated for each sample (Fig 3.20A). The mean Gamma Correlation pairwise coefficient showed a significant decrease in value between normal colon and MSS and MSI CRC samples, suggesting that normal colons reuse similar signaling modules across different samples more so than CRCs (Fig 3.19C). Using bulk (average) data to perform the same analysis resulted in different interpretations, again, with normal colon samples having high correlation between sets of signaling markers, MSS samples having reduced correlation, and MSI samples having correlation between different sets

of markers (Fig 3.20B). This difference may be due to the loss of single-cell resolution where markers expressed in different cells are considered to be in the same compartment as a sample average. These results demonstrated, in a quantitative fashion, that 1) cells within normal colon have shared regulatory mechanisms between pathways but not for cells in CRC samples (intratumoral heterogeneity), 2) organized signaling modules are reused between normal colon samples but not between CRC samples (intertumoral heterogeneity).

We next examined whether single-cell signaling properties of tumors are associated with molecular characteristics (Table 3.2). All microsatellite unstable (MSI) tumors in our set with a BRAFV600E mutation (4/4) presented with no CK20+ differentiated cells, whereas all other tumors (MSS or MSI with wild type BRAF – 0/9) presented with some degree of differentiation (Fig 3.19D, E). Furthermore, MSI-BRAF mutant tumors all had (4/4) some degree of CC3+ apoptotic cells, whereas only a minority of other tumors (3/9) exhibited this phenotype (Fig 3.19D, E). For MSS tumors specifically, a KRAS G12 mutation conferred downregulation of p-ERK, increased proliferation (Ki67), and upregulation of CLCA1+ goblet cell specification compared to KRAS wild type tumors (Fig 3.19F). These results provided evidence that molecular properties, not pathological details, correlate with single-cell signaling phenotypes in CRC.

Discussion

There is an ongoing effort to use next-generation genomic, epigenomic, transcriptomic, and proteomic data to predict tumor outcomes and responses to therapy (194). However, the degree of behavioral diversity within a tumor may be just as important, since different cellular populations may respond to drugs differently and cooperate to produce emergent behaviors. FFPE-DISSECT enables the analysis of single cell signaling activities in archival human tissues. Whereas large academic centers have access to various methods for human tissue preservation, such as flash freezing, most community hospital settings only have access to FFPE. These untapped, large human tissue resources can now be mined at the single-cell level for building appropriately powered models to inform how heterogeneity contribute to tumor behavior and how cellular diversity changes in response to treatment.

There are several caveats to using FFPE-DISSECT, which fall under the same limitations as other FFPE applications. First, the range of antibodies that actually work in FFPE tissues is reduced compare to freshly isolated tissues, because not all conformationally blocked antigens can be retrieved. We somewhat alleviated this problem by only using antibodies that are well-validated (e.g., by knockdown in human cell lines or mouse tissues) and are widely used in the field for FFPE applications. This problem can perhaps be further addressed in the future by better antibody generation practices. For example, a higher success rate for the generation of antibodies for FFPE applications may be achieved by using fixed proteins as immunogens instead of native peptides. Second, the veracity of a stain of a human FFPE section due to tissue degradation comes into

question. The preservation of signals, specifically of signaling proteins, is sensitive to the amount of time the tissue has been outside the body (185). Furthermore, storage conditions of FFPE block, such as temperature and humidity, may introduce variability in the results (195). Standardized operating procedures regarding post-excision time, fixation, and storage, such as those adopted by CHTN, are required to decrease the variability introduced during the tissue preparation step. Third, mass cytometry, although multiplexed, still remains a candidate-based method, and the biological insights derived are only as informative as the biomarker panel allows. A well-known shortcoming of immunohistochemistry techniques is the reliance on cell-type specific markers and morphology to identify cell types, whereas these properties may be altered by concomitant loss of architecture, infiltration of host cells, and dedifferentiation in dysplastic tissue. While we appreciate that cell identities in cancer may not reflect those of normal tissue, the use of multiplex marker panels, specifically those of signaling that represent the functional state of a cell, can allow for the inference of the lineage of origin of cancer cells with unknown identities. Using multiplex single-cell data with comparative algorithms such as Citrus (196), one can determine the similarity of cancer cells to reference signatures of normal cell types in marker space. Furthermore, candidate-based single-cell approaches can be coupled with single-cell RNA sequencing (197), and even other unbiased bulk-based methods to become a powerful discovery tool. There is high potential impact for characterizing unidentified transitional cells in cancer, as they may have altered properties that contribute to malignancy, and more importantly, may be targetable by therapy. All of the above limitations are inherent to FFPE applications in general, and should be considered and be controlled for at the study design phase.

The ability to query signal transduction in a cell-type specific or even at a single-cell level is a defined strength of our approach. The prevalent methods to detect and quantify signaling proteins remain to be bulk approaches such as Western blots and ELISA (184,198), which assume cellular homogeneity and are not always suitable for tissue analysis. With these approaches, positive signals in small subsets of cell are washed out by larger populations, and the cellular sources of positive signals cannot be determined. For imaging applications in tissues, cell-type specific signaling is usually evaluated with low multiplexity, for instance, looking at one signaling marker with one cell type marker. More recent advances, as mentioned above (115,176–180), allow for higher multiplexity but at the expense of feasible application on large sample sets. FFPE-DISSECT coupled to mass cytometry is a relatively rapid method for performing multiplex single-cell signaling analysis. It can be used for proposing interesting signaling markers that can be followed up with imaging, as we have done in this study.

The major assumption of FFPE-DISSECT, which begins with archival tissue blocks, is that the tissues are handled properly during the pre-analytical fixation steps. This assumption is widely made in the histopathology field, especially in tissue microarray or cohort studies where hundreds of samples are collected from different sources (199). Improperly fixed tissue will inevitably lead to invalid downstream analyses. To mitigate artefacts arising from this source, a standardized SOP was adopted for processing all tissues in this study. First, tissue thickness was limited to 5 mm, which according to common references (ref), should allow efficient penetration of fixation within one hour.

Second, fixative was incubated with a magnetic stirrer to maximize diffusion. Third, the fixation time was standardized at 24 hours. Last, and most importantly, a board-certified pathologist has reviewed the histology of tissue along with quality assurance-quality control data. Histological characteristics indicating poor fixation quality/inadequate fixative penetration include: 1) processing observations based on nuclear staining and appearance of cytoplasm, 2) scratches or hatching of the specimen during microtomy, 3) section disintegrating or pulling apart, 4) smudging or unusual staining, 5) other unusual artefacts, 6) stutter, 7) degree of autolysis, and 8) cells showing crenation. Samples indicative of fixation problems were not included in this study. Aside from pre-analytical evaluation, additional steps can be taken to identify potential artefacts after data collection. These include: 1) imaging tissue section from the same tissue block to ensure concordance (% of host cell infiltrating, relative intensity of markers) with single-cell data, 2) imaging single-cell suspensions to ensure disaggregation into single cells, 3) evaluating proper conjugation of antibodies by staining with both the conjugated and the unconjugated clone coupled to a secondary detection system, 4) assessing detection specificity by identifying CyTOF events that are positive for all markers. Many of these artefacts arise from the FFPE process, and we remain hopeful that widespread adoption of standardized procedures and additional technological advances will minimize these issues in the future.

Our approach illuminated differential signaling patterns in different cell types (enterocytes, goblet cells, and enteroendocrine cells), with the conclusion that secretory cells in general are more sensitive to basal and TNF-α-induced signaling. Goblet cells have the highest

signaling propensity, with upregulation of many pathways compared to enterocytes. Specifically, goblet cells upregulate p-ERK. We have identified p-ERK as a survival mechanism against TNF-α-induced apoptosis, and accordingly, goblet cells were also resistant to TNF-α-induced apoptosis (112). Furthermore, EGFR is an receptor upstream of p-ERK that plays critical roles in growth, survival, and differentiation in the stem cell niche (200). Following this line of logic, we established a link between Ras activation and goblet cell metaplasia in the intestinal epithelium. This is the first time that NRAS activation is connected to this phenotype to our knowledge. Demonstrating the casual effect of this pathway, ERK signaling downregulation has been documented to suppress goblet cell specification. Heuberger *et al.* have shown that epithelial specific SHP2 knockout suppresses p-ERK signaling and goblet cell differentiation by modulating TCF4 isoform switching and WNT-dependent transcription (201). This effect on goblet cells can be rescued by gain-of-function in MEK1. A more recent report by De Jong *et al.* has also shown that the knockout of both ERK1 and 2 downregulates goblet cell differentiation (202). Goblet cells were reduced, but not completely ablated in these studies, suggesting that there are redundant mechanisms to maintain goblet cell number. Using a multiplex cell-type specific approach, we propose other candidate signaling pathways, such as p-ATF2, that may act in synergy with p-ERK to control goblet cell specification.

Cellular heterogeneity is an important topic in cancer biology from both genetic and cell biology perspectives. Differential signaling between cells is a form of heterogeneity that controls cellular behaviors, but is relatively unexplored. Gerdes *et al.* reported that pathway relationships between signaling components identified from cell lines may not

hold true in human tissues when observed at single-cell level (115). Here, we identified signaling pathways that organize into a modular architecture associated with surface-to-crypt identity in the normal colonic epithelium. Consistent correlation between pathways over single cells represent regulatory mechanisms that are recurrently used by all cells in the tissue. Maintenance of modular architecture between samples reflects homogenous organization of signaling pathways. Quantifying these two properties using mass cytometry single-cell data suggest that both intra- and inter- tissue heterogeneity is increased in CRC regarding signaling regulation. Heterogeneity in cancer signaling reflects the relaxation of constraints that allows a cancer cell to sample a wider state space. These constraints can be physical or biochemical, from disorganization of tissue architecture to rewiring of signaling networks. In turn, a cell can adopt novel behaviors and functions outside of normal cellular behaviors, such as epithelial-to-mesenchymal transition (203).

The RAS-RAF-MEK-ERK MAP kinase cascade plays a major role in the pathogenesis of CRC. Activating KRAS and NRAS mutations are found in ~50% of all CRC, while activating BRAF mutations are found in ~10% of CRC (204–206). Mutations in KRAS and downstream BRAF have been shown to be a biomarker for resistance to upstream anti-EGFR therapies, as expected (207,208). However, downstream MEK inhibition has been shown to have limited efficacy in CRC with KRAS and BRAF mutations (209,210). While acquired resistance mechanisms, such as upregulation of ERBB family members and BRAF gene amplification (211,212), have been revealed in cell lines, an alternative explanation for the lack of efficacy of MEK inhibitors in the clinic may simply be that MAPK

signaling downstream of KRAS and BRAF mutations is not upregulated in CRC tissue, as shown in the current study. Unlike cell lines (213), activating KRAS and BRAF *in vivo* results in negative feedback that upregulates ERK phosphatase expression (191). Channing Der's group has observed that nuclear ERK phosphorylation in human CRC is not correlated to KRAS and, to a lesser extent, BRAF mutational status (214). Mouse models also revealed that KRAS activation in normal epithelium activates p-ERK, but this effect is inhibited in the context of cancer (188). These results support that tissue and disease contexts strongly govern the influence of genetics on the output of signaling pathways.

Although some argue for the redundant function of KRAS and BRAF mutations in MAPK signaling by their mutual exclusion (215), the cancer phenotypes induced by these mutations are vastly different. KRAS mutations mostly occurs in the common sporadic CRC pathway known as CIN (chromosomal instability), while BRAF mutations mostly occurs in the CIMP (CpG Island Methylator Phenotype) pathway (216,217). Hypermethylation of the MLH1 gene results in diminished DNA repair and induces a MSI-high phenotype distinct from that caused by mismatch repair gene mutations (such as in Lynch's syndrome) (218,219). Thus, BRAF mutations are seen in a majority of MSI tumors and rarely in MSS tumors (220). BRAF mutant pathology is also distinct from traditional adenocarcinomas, adopting a serrated morphology (206). Although microsatellite instability is often a good prognosis due to the infiltration of active immune cells (21,221), patients with BRAF mutant tumors have relatively poor overall survival despite their MSI status (219,222). These properties may be due to the lack of

differentiation in BRAF mutant MSI tumors, resulting in a large number of “stem-like cells” , as seen in this study and reported in others (161,223), which confers resistance to conventional therapies. Perhaps, increased sensitivity to apoptosis in these tumors, as marked by CC3 positivity, can be exploited as a therapeutic option. In our hands, KRAS mutation in MSS tumors is suggested to result in downregulation of p-ERK, upregulation of goblet cells, and increased proliferation, all in different cell populations. A weakness in our study is the low number of samples in each grouping, especially if we further partition samples by molecular details. Our intent here is to provide a proof-of-concept application of FFPE-DISSECT on human CRCs, and the hypotheses generated with this small cohort will need to be confirm in a larger set of tumors. However, given that our approach can be applied to FFPE blocks, one can have access to much larger repositories of retroactively collected samples that can power any study. FFPE-DISSECT coupled to mass cytometry applied to archival samples is a powerful tool to generate large amounts of single-cell data with acceptable throughput. These data are complementary to other precision medicine efforts to molecularly characterize solid tumors for arriving at subtypes that can predict prognosis and therapeutic response.

Methods

Mouse Experiments

All animal experiments were performed under protocols approved by the Vanderbilt University Animal Care and Use Committee and in accordance with NIH guidelines. Mice were stimulated with TNF-α as a time course, and their duodena (proximal small intestine)

were collected for analysis as previously described (183,184). For DISSECT, a previously published protocol was used (112). For FFPE embedding, tissues were fixed in formalin for 24 hours prior and then were subjected to standardized embedding procedures. Tissues were incubated in RPMI when outside of the body for extended time.

Human Tissue Acquisition

Human normal colon and colorectal cancer tissues were obtained under protocols approved by Vanderbilt University through the Cooperative Human Tissue Network (CHTN). Clinical and pathology reports were attached to each sample prior to de-identification of patient information. An optimized CHTN collection SOP was used. Briefly, specimen sizes were limited to 5 mm in diameter and fixed for 24 hours in magnetically stirred formalin (to facilitate diffusion), after which the specimen was embedded with a standardized FFPE protocol. The time from which the specimen was excised from the patient to the fixative (during which the tissue was examined by the pathologists or their assistants) was recorded as the post-excision time (PET). Specimens with substantial tumor cell content determined by haematoxylin and eosin staining were selected for analysis. Overall, 7 normal colon samples and 13 CRC samples were selected.

DISSECT Disaggregation on FFPE Tissues

50μm sections were freshly cut from each block and placed in 1.5mL microcentrifuge tubes (Fisher). Samples were heated to 65˚c for 25 minutes to melt wax, then washed 3

times with 1mL of histoclear for 8 minutes each. Tissues were then rehydrated in 2 washes each of 100%, 70% and 50% ethanol, then 3 washes of PBS. Samples were washed for 10 minutes in PBS with 0.3% Triton X-100, then washed a final time in PBS before incubation in the HIAR buffer (DAKO). Samples were incubated in the buffer under high heat and pressure for 20 minutes (actively heating for the first 4 minutes), followed by 20 minutes cooling of the bench. Samples were then washed 3 addition times in PBS and stored at 4˚ until staining. Tissues were blocked at room temperature (RT) for 30 minutes in 2.5% donkey serum (Jackson ImmunoResearch) in PBS and stained overnight at RT with antibodies diluted in the same buffer. Additional blocking with carefully chosen serum combinations were applied if secondary antibodies were used. After appropriate washing, samples were incubated for 30 minutes in 4% PFA to crosslink antibodies to their targets. Samples were washed, and then incubated for 25 minutes at 37˚C in 200µL PBS with 1mg/mL each of collagenase (Calbiotech) and dispase (Life Technologies). Tissues were passaged 5-10 times through a 27ga needle to mechanically dissociate them into single cells. Cells were incubated with a nuclear intercalating agent prior to analysis.

Cytometry Analyses

For both fluorescence cytometry and mass cytometry, cells were initially gated using DNA content (Hoescht – fluorescence cytometry) or intercalator (Iridium – mass cytometry) following established procedures to identify intact single cells and eliminate cell doublets and clusters from analysis (112,224,225). Single cells were then analyzed for intensity of

antibody conjugates. Fluorescence cytometry was performed on a BD LSRII with 5 lasers and mass cytometry was performed on a Fluidigm-DVS CyTOF 1 instrument. Epithelial-specific analysis was achieved by gating cells positive for pan-Cytokeratin (PCK).

Immunofluorescence Imaging

FFPE tissues were sectioned at 5 µm and processed using standard immunohistological techniques, stained with appropriate primary or primary/secondary antibodies. DISSECT-processed tissues were also imaged pre- and post- disaggregation in a whole-mount format. Slides were imaged using a Zeiss Axiophot fluorescence/brightfield microscope with a Zeiss Axiocam with 5 channel imaging capabilities. Quantitative analysis of goblet cells in the villus was performed on ImageJ using the particle analysis module. Ratios of areas occupied between the CLCA1 channel and nuclear channel were calculated with a correction factor for the typical size of a goblet granule against the typical size of a nucleus.

Quantitative Immunofluorescence Imaging and Immunoblotting of Signaling Proteins

The same antibody clones were used for FFPE-DISSECT-CyTOF. Quantifications were performed as before, outlined in (112).

Antibody Reagents

See Tables 1 and 3. All signaling antibodies were previously validated and used in mass cytometry applications (112).

Data Analysis

t-SNE analysis was performed using the viSNE implementation on Cytobank.org following established single-cell analysis workflows (226–228). Gating for cell types was performed by considering a first decade (10^1) threshold for cell type specific markers. Unpaired t-tests and correlation analyses were performed using Prism (Graphpad). Multiple comparison tests were performed with ANOVA with Tukey post-hoc test (Graphpad). Correlative distances and heat maps were generated using MATLAB (Mathworks). Hierarchical clustering and dendrogram analysis were performed using the dendextend package in R (192).

Chapter IV

SINGLE- CELL MASS CYTOMETRY OF ARCHIVED HUMAN EPITHELIAL TISSUE FOR DECODING CANCER SINGALING PATHWAYS

Recreated from: **Scurrah, CR**, Simmons, AJ, Lau, KS. Decoding cancer cell signaling pathways by single-cell mass cytometry. Methods Mol Biol. 2019.

Introduction

Analytic techniques have rapidly progressed to single-cell resolution, enabling assays that address cellular diversity within tissues. These approaches can characterize the increasingly appreciated heterogeneities that manifest in complex diseases. For instance, many cases of cancer are distinguished by intratumoral infiltration of immune, endothelial, mesenchymal, and endothelial cells. These microenvironmental influences, coupled to genetic alterations, present a landscape of diverse cancer cell states. Specifically, rare cell populations, such as tumor stem cells, possess specialized deleterious functions. Tumor stem cells frequently resist standard of care or targeted therapies, repopulate tumors during relapse, and contribute to distal metastases that eventually kill patients (66,229–231). Addressing rare cancer cell populations, as well as microenvironmental

infiltrates that modify prognosis, has become a necessity for better understanding cancer cell dynamics and devising more effective therapeutic strategies.

Until recently, results from single-cell analysis of epithelial cells have been skewed by the process of isolating individual cells from the native tissue context, which involves separating cells from the basement membrane and breaking cell-cell contacts (232). Cellular junction disruption perturbs the characteristic polarity of epithelial cells and subsequently alters native morphology and signaling, which results in substantial artifacts during downstream analysis (112,171,172). Our lab developed a technique, called DISSECT, to prevent these alterations by applying fixative to whole tissue to preserve cells in their native contexts prior to staining and dissociation. Single-cell suspensions from these preparations can be analyzed by mass cytometry (CyTOF), an advanced flow cytometry approach where heavy metal-tagged antibodies are utilized in place of fluorochrome-labeled ones to enable highly multiplexed measurements of protein expression (233). We have previously demonstrated the application of DISSECT-CyTOF on fresh samples and FFPE specimens (112,114). FFPE has been a standard practice in clinical pathological analysis of tissues for almost a century (234). Because its use in the long-term preservation of tissue morphologies has been widely demonstrated, large repositories of patient samples exist today. However, cryopreservation is now widely regarded as a superior method for tissue storage due to the preservation of sensitive antigens and nucleic acids that do not survive the process of formalin fixation, dehydration, and paraffinization. Here, we present detailed protocols for the application of DISSECT to fresh, FFPE, as well as cryopreserved tissue specimens. These

procedures will allow single-cell signaling analysis of epithelial tissue and enable new insights for epithelial-derived diseases and solid cancers.

Materials

2.1 Common reagents to all DISSECT procedures

1. 1X phosphate-buffered saline (1X PBS), without Ca^{+} and Mg^{+}.
2. Deionized water (DI H_2O).
3. 15 mL and 50 mL conical tubes.
4. 1 L containers.
5. 1.5 mL Eppendorf tubes.
6. Cytometry tubes with 35-µm cell strainer caps.
7. Water bath set at 37 °C.
8. Rocker to apply gentle motion to samples.
9. Vortex.
10. Desktop centrifuge.
11. Minifuge.
12. Flow Block- 2.5% donkey serum in 1X PBS: Add 1.25 mL of normal donkey serum [Jackson ImmunoResearch] into a 50 mL conical tube. Add 1X PBS to a final volume of 50 mL.
13. 1% Triton X-100 in 1X PBS: Add 500 µL of Triton-X 100 [Sigma; Cat: T8787] into a 50 mL conical tube. Add 1X PBS to a volume of 50 mL.

14. 1% Triton-X 100 in H_2O: Add 500 μL of Triton-X 100 into a 50 mL conical tube. Add DI H_2O to a final volume of 50 mL.
15. 10% Sodium Dodecyl Sulfate (SDS) in H_2O: Add 25 mL of 20% SDS to a 50 mL conical tube. Add DI H_2O to a volume of 50 mL.
16. XX Detergent-1% saponin, 0.05% Triton-X 100, and 0.01% SDS in 1X PBS: Weigh and add 0.5 g of saponin [Sigma] to a 50 mL conical tube. Add 2.5 mL of 1% Triton X-100 in 1X PBS and 50 μL of 10% SDS to the 50 mL conical tube. Add 1X PBS to a final volume of 50 mL.
17. 27.5 gage needles.
18. 1 mL syringes.
19. 0.5% Bovine Serum Albumin (BSA) in 1X PBS: Weigh and add 0.25 g of BSA into a 50 mL conical. Add 1X PBS to a final volume of 50 mL. Dissolve.
20. 4% Paraformaldehyde (PFA) stored at 4 °C.
21. 0.01% Triton-X 100 in 1X PBS: Add 10 mL of 1% Triton X-100 in 1X PBS into a 1 L container and add 1X PBS to a final volume of 1000 mL.
22. 0.003% Triton-X 100 in 1X PBS: Add 150 μL of 1% Triton X-100 in 1X PBS solution into a 50 mL conical tube and add 1X PBS to a volume of 50 mL.
23. 0.003% Triton-X 100 in DI H_2O: Add 10 mL of the 1% Triton X- 100 in DI H_2O into a 1L container and add DI H_2O to a volume of 1000 mL.
24. Dissociation solution-1 mg/mL of collagenase and dispase in 1X PBS: Collagenase [CalBio; Activity: 1260 U/mg] and dispase [Gibco; Activity: 1.73 U/mg] are each dissolved in DI H_2O at 100 mg/mL and frozen in 50 μL aliquots at –20 °C. (See **Note 1**) The day of the procedure, prepare the working solution by adding 2 μL of

both collagenase and dispase to the same 1.5 mL Eppendorf tube followed by 200 μL of 1X PBS. 200 μL of dissociation solution is necessary per sample therefore scale accordingly.

25. Hemocytometer.
26. Ir Intercalator: 1000X (125 μM) intercalator [Fluidigm; Cat: 201192A] is aliquoted at 25 μL each in 1.5mL Eppendorf tubes and stored at –20 °C. To prepare a 50X stock solution, add 500 μL of 1X PBS to a 25 μL aliquot. (See **Note 2).** The day of procedure, prepare a 1X working solution by adding 2 μL of the 50X stock solution to 100 μL of 1X PBS in a 1.5 mL Eppendorf tube. 100 μL of intercalator is necessary per sample, therefore, scale accordingly.
27. Normalization Beads: The day of the procedure, prepare a 1X bead solution by adding 1000 μL of a 10X stock solution of normalization bead [DVS; Cat: 201078] to a 15 mL conical tube. Add DI H_2O until a volume of 10 mL. This volume is used for 5-10 samples; therefore, adjust accordingly.
28. Antibodies: Refer to Table 4.1.
29. Mass cytometer (Fluidigm).
30. Data in this manuscript were analyzed using Cytobank (http://www.cytobank.org).

2.2 FFPE-DISSECT

1. Heat block at 65 °C.
2. Pressure cooker that has a warm and heat setting along with a timer [Cuisinart; Model: EPC-1200PC].

Tag	Target	Cat#	Clone
154Sm	CD45	3154001B	H130
156Gd	PDGFRb	3156018A	18A2
158Gd	CDH1 (E-CAD)	3158018B	DECMA-1
162Dy	Pan-Keratin	3162027A	C11
165Ho	ITGb3	3165010B	VI-PL2
167Er	CD11b	3167011B	ICRF44
168Er	Ki67	3168007B	B56
170Er	CK20	CS13063	D9Z1Z
174Yb	CK8/18	3174014A	C51

Table 4.1. Analytes measured in a human cryopreserved colon specimen for this study.

3. Histoclear [National Diagnostics; Cat:5989-27-5].
4. 100% ethanol (Histology grade).
5. 70% ethanol: Add 700 mL of 100% ethanol into a 1L glass jar and add DI H_2O to a final volume of 1000 mL.
6. 50% ethanol: Add 500 mL of 100% ethanol into a 1L glass jar and add DI H_2O to a final volume of 1000 mL.
7. 1X antigen retrieval buffer-1X DAKO solution: Prepare the day of the procedure, by adding 1mL of a 10X DAKO target retrieval solution (pH 6) [Agilent; Cat: S169984-2] into a 15 mL conical. Add DI H_2O to a final volume of 10 mL. 1.5 mL solution per sample is necessary therefore adjust accordingly.
8. 0.3% Triton X-100 in 1X PBS: Add 15 mL of the 1% Triton X-100 in 1X PBS solution into a 50 mL conical tube and add 1X PBS to a volume of 50 mL.

2.3 Cryo-DISSECT and DISSECT on fresh tissue

1. Acetone stored at –20 °C in a 50 mL conical.

Methods

For FFPE applications, standard procedures for FFPE embedding were assumed to be followed. In summary, resected tissue is immediately fixed in formalin overnight (16-24 h), followed by dehydration, clearing, and embedding in paraffin. For cryopreservation, resected tissue is immediately embedded in Optimal Cutting Temperature compound

(OCT) and stored at –80 °C in mold cassettes. For fresh tissue, follow the DISSECT protocol to 3.1.3, then switch to the Cryo-DISSECT protocol starting at *3.3.5.* For FFPE specimens, follow the FFPE-DISSECT protocol to 3.2.20, then switch to the Cryo-DISSECT protocol starting at *3.3.17*. For cryopreserved specimens, follow the Cryo-DISSECT protocol. An overview of the protocols is shown in Fig 4.1A. Be sure to process and analyze the samples in due time (*see* **Note 3**).

3.1 Starting DISSECT from fresh tissue

1. Isolate tissue and divide it into small (<1mm) portions.
2. Fix tissue in 4% PFA for 20 min at room temperature (RT).
3. Follow the ***Cryo-DISSECT protocol*** from *3.3.5.*

3.2 Starting DISSECT from FFPE tissue (FFPE-DISSECT)

1. Cut 2-5 50 μm curls using a microtome and put them into a 1.5 mL Eppendorf tube (will appear similar to Fig 4.1B) (*see* **Note 4**).
2. Incubate tubes of FFPE curls on heat block at 65 °C for 25 min.
3. Add 1 mL of histoclear to each pre-warmed tube. Vortex and check the tubes to determine if paraffin wax is melted (*see* **Note 5**). If paraffin wax is not melted, incubate tubes containing histoclear and curls for 8 min on the heat block at 65 °C. If paraffin wax is melted, incubate tubes containing histoclear and curls for 8 min at RT (*see* **Note 6**).

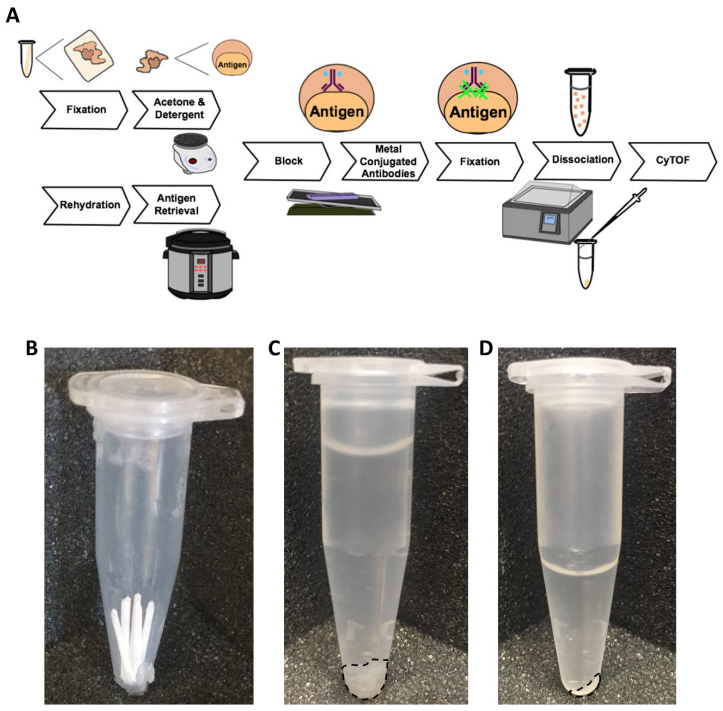

Fig 4.1. Overview of methodologies. (A) Cryopreserved or fresh tissue undergoes fixation followed by acetone and detergent incubation, while FFPE tissue initially undergoes rehydration and antigen retrieval. Both protocols merge for block, staining, signal fixation and dissociation. Under each step is the equipment used for performing the techniques, while tissue states are diagramed above the steps. Samples are normalized by: (B) number of curls before fixation, (C) tissue volume before dissociation, (D) and number of cells after dissociation prior to cytometry analysis.

4. Pellet tissue at 2000 xg for 2 min and remove supernatant. Repeat twice at RT (*see* **Note 7** prior to rehydration and antigen retrieval).
5. Suspend tissue in 1mL of 100% ethanol, vortex and incubate at RT for 8 min. Pellet tissue at 2000 xg for 2 min or allow it to settle and carefully remove supernatant. Repeat once.
6. Suspend tissue in 1 mL of 70% ethanol (see 2.2.5), vortex and incubate at RT for 8 min. Pellet tissue at 2000 xg for 2 min or allow it to settle and carefully remove supernatant. Repeat once.
7. Suspend tissue in 1 mL of 50% ethanol (see 2.2.6), vortex and incubate at RT for 8 min. Pellet tissue at 2000 Xg for 2 min or allow it to settle and carefully remove supernatant. Repeat once.
8. Suspend tissue in 1 mL 1X PBS.
9. Pellet tissue at 2000 xg for 2 min and remove supernatant. Repeat twice. If sample is greater than 300 μL when pelleted, split up sample into individual tubes.
10. While washing samples, make a 1X DAKO antigen retrieval buffer (see 2.2.7) and heat the solution with a loosened lid in pressure cooker on the “keep warm” setting.
11. Suspend tissue in 0.3% Triton X-100 (see 2.2.8). Incubate at RT for 10 min.
12. Pellet tissue at 2000 xg for 2 min and remove supernatant.
13. Suspend tissue in 1 mL 1X PBS.
14. Pellet tissue at 2000 xg for 2 min and remove supernatant.
15. Suspend tissue in 1mL of hot 1X antigen retrieval buffer. Place tubes with lids open in rack in pressure cooker, lock lid, and set for 4 min at high pressure. Leave tubes in pressure cooker for 20 min total.

16. Remove tubes from pressure cooker and allow 20 min to cool on the bench at room temperature. After this step, tissue should assume new appearance and be much easier to pellet because any agar will have melted away.
17. Pellet tissue at 2000 xg for 2 min and remove supernatant.
18. Suspend tissue in 1 mL 1X PBS and transfer to a new pre-labeled tube.
19. Pellet tissue at 2000 xg for 2 min and remove supernatant. Repeat twice. Tissue can be stored at 4 °C on 1X PBS until use.
20. Follow the ***Cryo-DISSECT protocol*** from *3.3.17*.

3.3 Starting DISSECT from frozen tissues (Cryo-DISSECT)

1. Store tissues at –80 °C until processing.
2. Cut 2-5 50 μm sections using a cryostat at –20 °C (Fig 4.1B) (*see* **Note 4**).
3. Place sections into a 1.5 mL Eppendorf tube and keep at –20 or –80 °C until needed.
4. If necessary, thaw samples into 4% PFA for 20 min at RT (*see* **Note 8)**.
5. Pellet tissue at 2000 xg for 2 min and remove supernatant *(for general advice, see* **Notes 9 and 10***)*.
6. Suspend tissue in 1 mL 1X PBS; incubate for 5 min.
7. Pellet tissue at 2000 xg for 2 min and remove supernatant. Repeat twice. Wash more times for longer periods if OCT remains in the sample (*see* **Note 6**).
8. If sample is greater than 300 μL when pelleted, split up sample.

9. Pellet tissue at 2000 xg for 2 min and remove supernatant (*see* **Notes 7 and 11** prior to acetone).
10. Vortex sample vigorously to ensure that the tissue does not remain pelleted.
11. Add 1 mL of acetone that was kept at –20 °C, vortex briefly, and immediately place the tube into a minifuge.
12. Spin for approximately 10-20 seconds at 2000 xg to pellet tissue.
13. Pour off acetone and let dry for approximately 30 seconds.
14. Suspend tissue in 1 mL of XX detergent solution (see 2.1.16).
15. Gently vortex or agitate for 30 min at RT.
16. Pellet tissue at 2000 xg for 2 min and remove supernatant. Add 1mL of 1X PBS. Repeat once. Tissue can be stored at this step at 4 °C in 1X PBS for a few days if needed.
17. Suspend tissue in 300 μL of Flow Block (see 2.1.12) (Fig 4.1C).
18. Incubate tubes upright for 30 min with gentle rocking.
19. Add 1mL of 1X PBS.
20. Pellet tissue at 2000 xg for 2 min and remove supernatant.
21. Suspend tissue in 100 μL of primary antibodies in Flow Block.
22. Incubate overnight, upright, covered (or in a dark room), with gentle rocking. Be sure to confirm that stain has penetrated by microscopy (Fig 4.2A) (*see* **Note 12**).
23. Add 1 mL of 1X PBS.
24. Pellet tissue at 2000 xg for 2 min and remove supernatant. Repeat twice.
25. If needed, suspend tissue in secondary antibody in 100-200 μL of Flow Block.
26. Incubate for 1 h covered with gentle rocking.

27. Add 1 mL of 1X PBS.
28. Pellet tissue at 2000 xg for 2 min and remove supernatant. Repeat twice.
29. To fix signals, suspend tissue in 4% PFA.
30. Incubate for 30 min with gentle rocking.
31. Add 1 mL of 1X PBS.
32. Pellet tissue at 2000 xg for 2 min and remove supernatant. Repeat twice.
33. Enzymatic dissociation: Suspend tissue in 200 μL dissociation solution (see 2.1.24) (*see* **Note 13**).
34. Incubate for 1 h in the 37 °C water bath. For FFPE tissue, incubate for 20 min.
35. Add 800 μL of 0.003% Triton X-100 in 1X PBS (see 2.1.22).
36. Mechanical dissociation: passage tissue through a 27.5 gage needle connected to a 1mL syringe 5-10 times until solution is cloudy and most the tissue is dissociated.
37. To remove large debris and undigested material, filter cells through a 35 μm-nylon mesh filter. This can be done with a tube cap filter (designed for a 5 mL flow cytometry tube) directly into a clean 1.5 mL Eppendorf tube (Fig 4.1D).
38. Pellet cells at 5000 xg for 5 min and remove supernatant.
39. Suspend cells in 100 μL of 0.5% BSA (see 2.1.29) in PBS overnight at 4 °C if not running immediately. If running immediately, go to next step.
40. Add 1 mL 0.003% Triton X-100 in 1X PBS. Single cells can be imaged via fluorescently labelled secondary antibodies to confirm staining (Fig 4.2B) (*see* **Note 12**).
41. Pellet cells at 5000 xg for 5 min and remove supernatant.

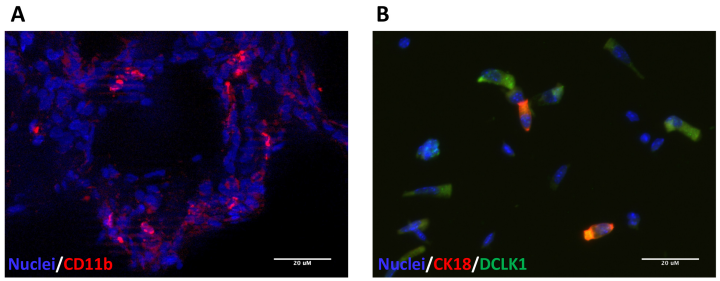

Fig 4.2. Immunofluorescence validation at different stages of processing. (A) Whole mount tissue staining before dissociation. (B) Single cell suspension after dissociation. Columnar epithelial morphologies are observed.

42. Suspend cells in 100 μL of intercalator (see 2.1.26).
43. Incubate for at least 20 min and at most 48 hh.
44. Add 1 mL of 0.003% Triton X-100 in 1X PBS.
45. Pellet cells at 5000 xg for 5 min and remove supernatant.
46. Add 1 mL of 0.003% Triton X-100 in DI H_2O (see 2.1.23).
47. Determine the number of cells in each sample by loading 10 μL onto a hemocytometer.
48. Pellet cells at 5000 xg for 5 min and remove supernatant. Leave samples on ice in the dark until they are ready to load.
49. Re-suspend cells in a volume of normalization bead solution (2.1.27) to achieve a concentration of 2.5-5 x 10^5 cells/mL, or, if cell density is insufficient, into the minimum sample volume for the instrument (usually 350-450 μL).
50. Transfer to a 5 mL filter top tube immediately before loading on the CyTOF. (Alternatively, fluorescent flow cytometry can be used with replacing the intercalator with a DNA dye such as Hoechst).
51. After samples are finished running on the CyTOF instrument, FSC data files can be uploaded to Cytobank.org for analysis. Optionally, these files can be normalized using elemental beads (235).
52. The intact cell population is determined through a bivariate plot comparing cell length and Ir intercalator (channel 193 or 191). Once the cell population is identified, elemental beads can be gated out via metals 151 and 175 (and others). The cell population can then be analyzed by bivariate plots for marker expression and further sub-population classification (Fig 4.3).

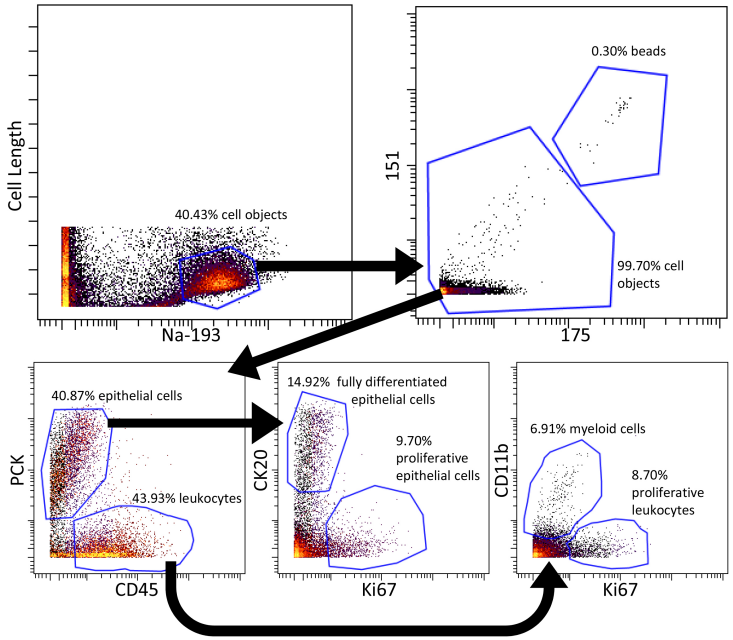

Fig 4.3. Bivariate plot strategies for analyzing cell populations from Cryo-DISSECT mass cytometry data of the human colon. Cells were gated as objects with positive staining of Ir intercalator and exceeding a certain ion cloud size. Elemental normalization beads were further excluded in the 155 and 175 channels from cell objects. Within the cell object population, epithelial cells were PCK-positive, while PCK-negative cells represented non-epithelial cells, a population of which was CD45+ leukocytes. Amongst epithelial cells, differentiated cells (on the luminal surface) were identified by CK20 expression while proliferative cells were marked by Ki67 expression. Amongst leukocytes, myeloid (monocyte and others) cells were marked by CD11b, while proliferative leukocytes were marked by Ki67.

53. Different cell populations can also be identified by t-distributed stochastic neighbor embedding (t-SNE) analysis, allowing the visualization of multidimensional data in 2-D space. Overlaying different markers on a t-SNE map allows for the identification of cell clusters by their properties (Fig 4.4). (see **Note 14**).

Notes

1. Once thawed, collagenase and dispase aliquots are good for at least a month stored at 4 °C.
2. The 50X Ir Intercalator stock solution is good for at least 6 months stored in the dark at 4 ˚C between uses.
3. Samples should be processed to completion within a week of thawing or de-paraffinization. As with any mass cytometry experiment, to avoid the possibility of cross-labeling between heavy metals and antibodies, run samples within 24 h of staining. DISSECT samples can be more prone to cross-labeling artifacts due to the level of processing required.
4. Under some circumstances, cutting 50 μm sections from FFPE- or cryo-blocks can present problems with crumbling. Weigh paper (or something similar) can be used to collect tissue fragments which do not remain in the curl and fall during cutting. Cutting can be made easier by trimming down the amount of embedded material with a razor blade. Too many curls in 1 tube during de-paraffinization can result in incomplete wax removal and rehydration. The initial melted or thawed embedding material should be less than 250 μL in volume. Samples can be pooled after

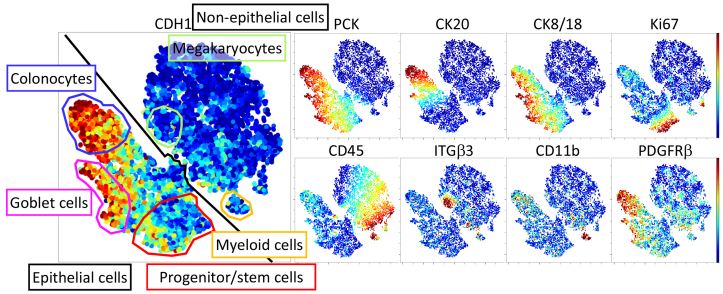

Fig 4.4. t-SNE analysis of cell populations from Cryo-DISSECT mass cytometry data of the human colon. Heat overlays (low to high) represent the Arcsinh-transformed expression level of indicated proteins determined by mass cytometry. Cell populations (color-coded gates) were manually identified on the t-SNE plot based on marker expression, as detailed in Fig 4.3.

retrieval if necessary.

5. Tissues in histoclear may refuse to settle and even swirl around in the tube in response to electrostatic charges from gloved fingers in near contact. This can make removal of solution without disturbing the tissue pellet difficult. There are a number of ways this could be overcome. For instance, biopsy bags have been used with some success, but they tend to wick and carry solutions over between washes, and it can be difficult to recover the tissue from the mesh (182). Larger volumes or different types of tubes may also help, though it's important to choose materials with respect to their resistance to histoclear. Even polypropylene tubes are somewhat damaged by histoclear, so it is helpful to change tubes after the tissue is hydrated. Furthermore, it is recommended to avoid spinning tissues faster than 5000 xg to prevent tissue from pelleting too densely or being damaged. If tissue is still not settling, carefully remove the histoclear, rotating and tilting the tube to allow for liquid to move away from tissue as it sticks to the side of the tube. If tissues are still difficult to pellet and aspirate before antigen retrieval, it is suggested to prepare excess antigen retrieval solution, and buffer exchange it onto the tissue (add a volume, carefully remove as much as possible, then add another volume). It may be helpful to repeat (with hot buffer) after antigen retrieval as well, as it is possible to still find wax precipitating in the cooling solution.
6. The first washes of both procedures are intended to remove the embedding matrix (paraffin for FFPE-DISSECT and OCT for Cryo-DISSECT), and subsequent staining is dependent on its complete removal. Because of this, users should normalize samples such that each tube contains a comparable amount of matrix,

and split any samples that may contain too much material. Washes can be lengthened or added to assist in removal of the embedding matrix. If possible, embedding material should be reduced prior to the cutting of sections by trimming the tissue block.

7. Before beginning antigen retrieval (FFPE-DISSECT) or acetone (Cryo-DISSECT) procedures, sample should be normalized such that each tube contains roughly the same pelleted volume of tissue. This can be done by splitting or pooling like samples, and ensures that all samples consistently experience the same concentration of reagents. Likewise, samples should be normalized by cell number (determined in 3.3.47) through dilution immediately before loading onto CyTOF for analysis.
8. For cryopreserved tissue, it is important to make a distinction between tissue which has or has not been fixed prior to freezing. It is recommended to fix tissue for no longer than 1 h if doing so prior to freezing. Curls cut from tissue that has never been fixed will need to be fixed gently in a large volume of 4% PFA while undergoing thawing for 20 min before further PBS washes. Users should follow cryopreservation guidelines concerning the use of sucrose and freezing speeds that are appropriate for their tissue of interest, and cut 5-10 µm sections for slides (in addition to thick sections for cytometry) to verify that morphology and cell integrity have been properly preserved.
9. Always check the lid and sides of tubes between washes for adherent tissue. If tissue is sticking to the side, adding Triton-X 100 or BSA to the 1X PBS may help to release it. It is advised to use Triton-X 100 below its critical micelle concentration

in a wash to reduce its capacity to damage lipids (236). Incubating tubes upright ensures the tissue remains submerged. Once hydrated in 1X PBS with Triton-X 100, tissues tend to pellet much easier.

10. If tissue is difficult to pellet, for any given incubation or wash, aspirate the most difficult samples first. This would leave a large residual volume for the first sample to avoid tissue loss. All other samples should be aspirated to that volume to normalize wash efficiency. Add an additional wash or two of the given buffer for all samples to compensate for the large residual volume at each step. This ensures that (a) samples are treated the same and (b) samples are given enough buffer exchanges to sufficiently wash the tissue.
11. The acetone and XX detergent wash sequence utilized for Cryo-DISSECT is somewhat time and temperature sensitive. To ensure that samples are handled consistently, prep them in batches of 4-6 samples maximum. It is crucial not to begin with too much tissue: a residual 1X PBS volume as little as 100 µL can dilute the acetone and prevent cells from pelleting properly, resulting in tissue loss or difficulty decanting.
12. Users with immunohistochemistry or immunofluorescent staining on FFPE and cryopreserved tissues are well-suited to perform these procedures, as many quality control steps involve imaging. It may be helpful for users to modify the buffers, antigen retrieval, and staining conditions to those where the staining can be visualized in imaging (either FFPE- or Cryo-DISSECT). Generally, antibodies that work in the respective imaging applications have a better chance of working in FFPE- or Cryo-DISSECT coupled to cytometry. Validation of antibodies should

occur before any experiment. Additionally, it is important and advantageous to validate the presence of signals at every step by checking a portion of the sample suspension on the microscope with a fluorescently-labeled secondary antibody (Fig 4.2).

13. The enzymatic and mechanical dissociation procedure may require optimization to accommodate different tissues, fixations, and antigen retrieval techniques. While a variety of tissues have been successfully processed using the dissociation solution described above, the duration has varied significantly. FFPE intestinal tissue, presumably due to the high level of processing, dissociates much faster (20 min dissociation) than the same tissue that has only been lightly fixed (1h dissociation time). FFPE tissue that has been hydrated, but not antigen retrieved, however, will not dissociate. To optimize dissociation, multiple digests of the same tissue should be set up and mechanical dissociated at selected time points to identify the best conditions. Tissues should mostly pass through the syringe after some light trituration (moving the plunger a short distance in and out 10-20 times quickly). For lightly fixed mouse intestinal tissue, the muscle normally does not dissociate and is filtered out. Samples should become cloudy with cells after 5-10 full-volume passages with a syringe, and mostly single cells bearing intact morphology should be observed under the microscope (Fig 4.2B). For some tissues, pipetting alone may be enough to separate cells.
14. The human colon tissue analyzed here has two major cell populations: epithelial and non-epithelial cells. Within epithelial cells, there are distinct absorptive, secretory, and progenitor cell populations, while in the non-epithelial cells myeloid

and megakaryocyte cell populations can be observed.

Chapter V

TUMOR STEM CELLS ARISING FROM A NON-STEM ORIGIN MAINTAIN A DIFFERENTIATED PHENOTYPE AND MODULATE T CELL ACTIVITY

Recreated from: **Scurrah CR**, Chen B, Markham N, Simmons AJ, Southard-Smith A, Macedonia MC, Washington K, Liu Q, Goettel JA, Coffey RJ, Lau KS. Tumor stem cells arising from a non-stem origin maintain a differentiated phenotype and modulate T cell activity (In preparation).

Introduction

Within the diversity of cell types in a tumor, tumor stem cells (TSCs) represent an important cell population for malignancy and patient prognosis (80,237). TSCs possess stem capacities to self-renew and maintain the diversity of cell types within the tumor (80). Various reports have also described additional properties of TSCs to resist cytotoxic therapy, repopulate the tumor, and metastasize to distal sites (83–85,231). Furthermore, recent large-scale data-driven efforts from The Cancer Genome Atlas (TCGA) have identified a stemness index associated with advanced tumor grade, metastasis, and an

altered immune microenvironment in various cancer types (86). An unanswered question critical to understanding the biology of TSCs is the origin of their stem-like properties.

Much effort of the cancer research field has been devoted to the prescription of cellular functions to genetic alterations (238,239). However, the diversity of functional cell state can also be determined by non-genetic factors (53). A specific context by which tumor stem-like properties can be prescribed is the tumor cell-of-origin. The tumor cell-of-origin is the original, normal cell where the tumor initiating event, such as an oncogenic mutation, occurred. All tumor cells, including TSCs, are progenies of the tumor cell-of-origin. Greater than 80% of sporadic colorectal cancer (CRC) cases develop when both alleles of *APC* are inactivated (72), and it is well-accepted that when such Wnt pathway perturbing events occur in stem cells, tumors can arise (67,74–77,240–242). However, there exists multiple gut epithelial cell populations that can be activated as fail-safe mechanisms for maintaining homeostasis under various damaging conditions. Lgr5-expressing crypt base columnar (CBC) stem cells actively proliferate and act as the source of continuous epithelial renewal. Upon different types of damage, various cell populations within the differentiation continuum can regain stem-like properties and serve as “facultative” stem cells (54,56–60,243,244). How each of these facultative stem cell populations differ from traditional stem cells in terms of proliferation rates, stem capacity, and biased differentiation towards certain lineages remains to be studied. Furthermore, their potential for tumorigenesis compared to traditional stem cells have not been elucidated.

Tumorigenesis from a non-stem cell route has been proposed, where neoplastic cells at upper parts of the crypts are observed to be genetically distinct from the non-neoplastic stem cells residing at the bottom of the crypts in human patients (245). There have also been elegant mouse studies that demonstrate tumorigenesis can indeed occur from non-CBCs (56,57,59,67,243). Since some cells in the tumor eventually regain stem-like properties, the route of non-stem cell tumorigenesis can be considered to be through a facultative stem cell pathway. What has not been shown previously is whether and how tumor cells, and specifically TSCs, arising from different cellular origins behave differently. To address this question, we initiated tumors in the murine colon from *Lrig1*-expressing stem cells and *Mist1*-expressing non-stem cells using the same genetic event - bi-allellic loss of function of *Apc*. We characterized TSCs of the resulting tumors from the different origins, revealing differences in stem capacity and antigen presentation ability, which contributed to a favorable immune microenvironment skewed towards active cytotoxic response and away from immune suppression in non-stem cell-driven tumors. These results suggest that the cell-of-origin of tumorigenesis provides a specific context by which TSCs are generated, which dictates their interactions with the tumor microenvironment.

Results

Mist1-expressing cells are non-stem cells that exhibit minimal stem capacity under damage

To examine whether *Mist1*-expressing cells exhibit stem capacity, we performed lineage tracing under homeostatic and damage conditions using *Mist1*$^{CreERT2/+}$*; Rosa26*$^{LSL-EYFP/+}$ mice, compared to *Lrig1*$^{CreERT2/+}$*; Rosa26*$^{LSL-EYFP/+}$ mice. Cre recombinase activity was induced with intraperitoneal injection of tamoxifen for 3 consecutive days to activate EYFP expression in Cre-expressing cells and all of its progenies (Fig 5.1A). Consistent with the well-documented characterization of *Lrig1*+ stem cells (240), individual crypt epithelial cells were labeled 24 hours after activation of lineage tracing in *Lrig1*-expressing cells (Fig 5.2A, and Fig 5.1B), and entire crypt labeling persisted long-term for up to 28 days (Fig 5.2A-B and Fig 5.1B), demonstrating the self-renewal capacity and multipotency of the labeled stem cells. Entire crypt labeling was not observed when the same experiment was performed in *Mist1*$^{CreERT2/+}$*; Rosa26*$^{LSL-EYFP/+}$ mice. While individual cells were initially labelled, these cells were completely lost from the epithelium at 28 days after induction (Fig 5.2A-B, and Fig 5.1B), signifying the turnover of non-stem cells during epithelial renewal. Cells in the lamina propria, most likely long-lasting plasma cells that express high levels of *Mist1*, still retained label after 28 days (refs. 29,30; Fig 5.2A, Fig 5.1B). To determine the stem capacity of *Mist1*-expressing cells in a damage context, we introduced 2.5% Dextran Sodium Sulfate (DSS) into drinking water after tamoxifen administration to exclude the possibility of inflammation- induced upregulation of *Mist1* in stem cells, and evaluated lineage tracing as a time course post-cessation of DSS (Fig 5.1A). Long-term lineage tracking was also not observed in this condition (Fig 5.2A-B, and Fig 5.1C). A previous report has documented lineage tracing from *Mist1*-expressing colonic epithelial cells using a mT/mG reporter upon DSS damage (151). Given the difference in lineage

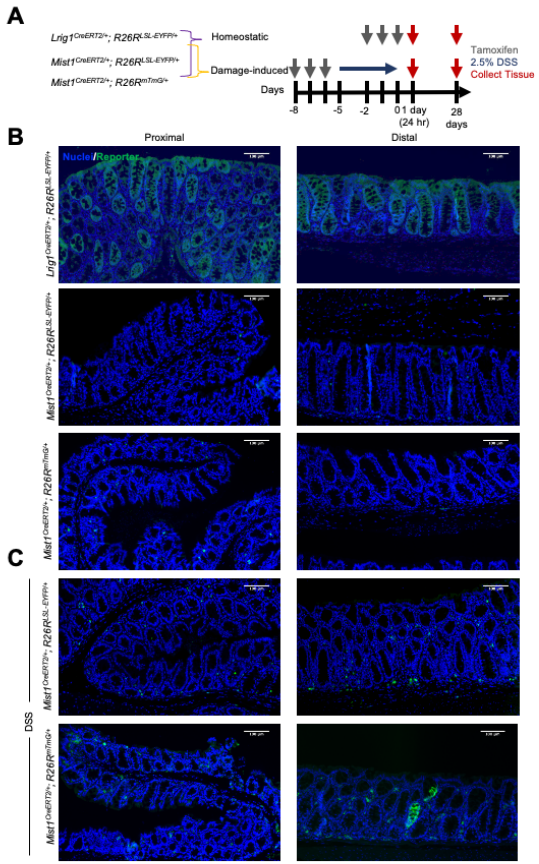

Fig 5.1: *Mist1*-expressing cells exhibit minimal stem capacity under homeostatic or damage conditions. (A) Experimental timelines of homeostatic and DSS damage-induced lineage tracing. (B-C) Representative IF images of long term (28 day) lineage tracing driven from stem (*Lrig1*^{CreERT2}) and non-stem (*Mist1*^{CreERT2}) cells with different reporters at (B) homeostasis and with (C) DSS damage.

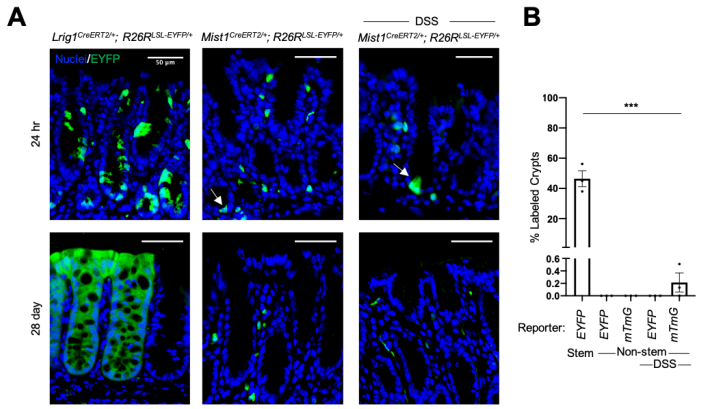

Fig 5.2. *Mist1*-expressing cells exhibit minimal stem capacity under homeostatic or damage conditions. (A) Representative IF images of short term and long term (rows: 24 hours and 28 days, respectively) lineage tracing in the colon using *Lrig1*$^{CreERT2/+}$; *R26R*$^{LSL-EYFP/+}$, *Mist1*$^{CreERT2/+}$; *R26R*$^{LSL-EYFP/+}$, and Mist1$^{CreERT2/+}$; *R26R*$^{LSL-EYFP/+}$ with DSS mouse models (columns). (B) Quantification of lineage traced glands at 28 days at homeostasis or with DSS-damage from stem (Lrig1) and non-stem (Mist1) cells using different reporters. Error bars represent SEM from n=3 animals for each condition, ***p-value< 0.001.

reporter performance due to differential epigenetic silencing (248–250), we repeated the damage-induced lineage tracing experiment in *Mist1*$^{CreERT2/+}$*; Rosa2*$^{mT/mG/+}$ mice (Fig 5.1A). A background level of crypts exhibited lineage tracing 28 days post DSS cessation, significantly lower than *Lrig1*-expressing cells even with a more favorable reporter (Fig 5.2B, and Fig 5.1C). Short term induction revealed that the reporter labelled a significant portion of epithelial cells in *Mist1*$^{CreERT2/+}$*; Rosa2*$^{mT/mG/+}$ mice (Fig 5.3A), demonstrating that the paucity of long-term labeled crypts was not due to the rarity of initially labelled cells. These results implicate that *Mist1*-expressing epithelial cells are non-stem cells during homeostasis, and their stem capacity as facultative stem cells is significantly lower than that of *Lrig1*-expressing stem cells.

***Mist1*-expressing cells are secretory progenitor cells in the colonic epithelium**

We next investigated the identity of colonic *Mist1*-expressing cells, which we have shown to be non-stem cells under homeostasis and have not been characterized in the colon. *Mist1* is an important *bHLH* transcription factor that modulates intracellular scaling of secretory cells throughout the body (251). Once cell fate is determined, *Mist1* expression leads to expansion of the endoplasmic reticulum for protein production, and machinery for secretory vesicular docking and release (252). Since *Mist1* expression is necessary for proper acinar, chief, and Paneth cell maturation in the gastrointestinal tract (252,253), we hypothesized that *Mist1*-expressing cells is also in the secretory lineage of the colon. To determine the identity of *Mist1*-expressing cells, we examined secretory cell marker co-expression with reporter by immunofluorescence in the colonic

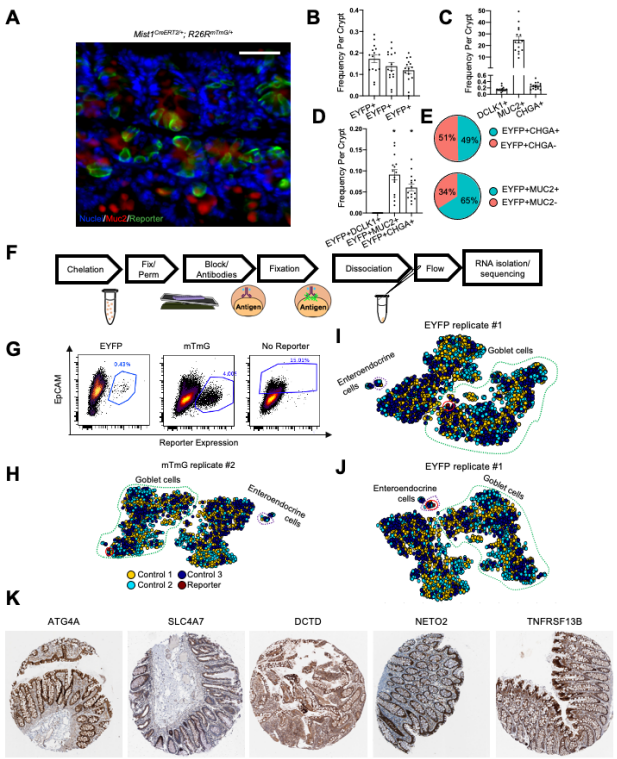

Fig 5.3: *Mist1*-expressing cells are secretory progenitors. (A) Representative IF image of reporter co-expression with Muc2 in *Mist1*$^{CreERT2/+}$*; R26R*$^{mTmG/+}$ 10 days after initiation of lineage tracing at homeostasis. Quantification of (B) EYFP reporter expressing cells, (C) different cells marked by cell type markers, and (D) double positive cells co-expressing reporter and marker, in *Mist1*$^{CreERT2/+}$*; R26R*$^{LSL\text{-}EYFP/+}$. Error bars represent SEM from n=3 animals, *p-value<0.05. Dots represent fields of view. (E) Proportion of reporter-expressing cells co-expressing secretory cell type markers. (F) Scheme of a modified DISSECT protocol for sorting fixed reporter expressing cells (G) Gating strategies for sorting reporter and non-reporter expressing cells for sequencing. (H-J) More biological replicates of Fig 5.4B. Combined t-SNE embedding of bulk RNA sequenced *Mist1* mTmG (H) and EYFP (I-J) expressing cells (solid circle in red) with n=3 reference murine colonic scRNA-seq dataset (colored dots from different mice). Goblet (green) and enteroendocrine (magenta) cell populations are delineated by dotted lines. (K) Protein expression of genes with non-specific expression in the colonic epithelium to match the differential gene expression analysis in Fig 5.4E (obtained via https://www.proteinatlas.org/). *Contribution from Chen B, Simmons AJ, Southard-Smith A, Lau KS*

epithelium of *Mist1*$^{CreERT2/+}$; *Rosa26*$^{LSL\text{-}EYFP/+}$ mice 24 hours post-induction, where individually labeled cells are detected. Reporter expression was found in MUC2 and CHGA-expressing goblet and enteroendocrine cells, respectively, but not in the DCLK1+ tuft cells (Fig 5.4A-B, and Fig 5.3B-E). Reporter was found to be co-expressed more often with CHGA than MUC2 (Fig 5.4A-B), suggesting a skewing towards the enteroendocrine fate. These results suggest that *Mist1*-expression may mark a common progenitor to enteroendocrine and goblet cells within the colonic secretory cell lineage.

To confirm their secretory identity in an unbiased manner, we conducted transcriptomic analysis of reporter-expressing cells in the colonic epithelium of *Mist1*$^{CreERT2/+}$; *Rosa26*$^{LSL\text{-}EYFP/+}$ and *Mist1*$^{CreERT2/+}$; *Rosa26*$^{mT/mG/+}$ mice 24 hours post-induction. We used a modified fixation-dissociation protocol (113) for intracellular staining to flow sort reporter-expressing cells and then prepared libraries using a modified MARIS (Method for analyzing RNA following intracellular sorting) protocol (254) for bulk RNA-sequencing of small numbers of fixed cells (Fig 5.3F-G). The bulk transcriptomes of reporter-expressing cells were then co-embedded with single-cell RNA-sequencing (scRNA-seq) data from the colonic epithelium where epithelial cell types can be resolved and annotated. Bootstrapped t-Distributed Stochastic Neighbor Embedding (t-SNE) revealed that reporter-expressing cells co-embed with *Chga*+ enteroendocrine and *Muc2*+ goblet cells at various frequencies, but not with other epithelial cell types (Fig 5.4C-D and Fig 5.3H-J). To further confirm the secretory identity of *Mist1*-expressing cells, we evaluated critical

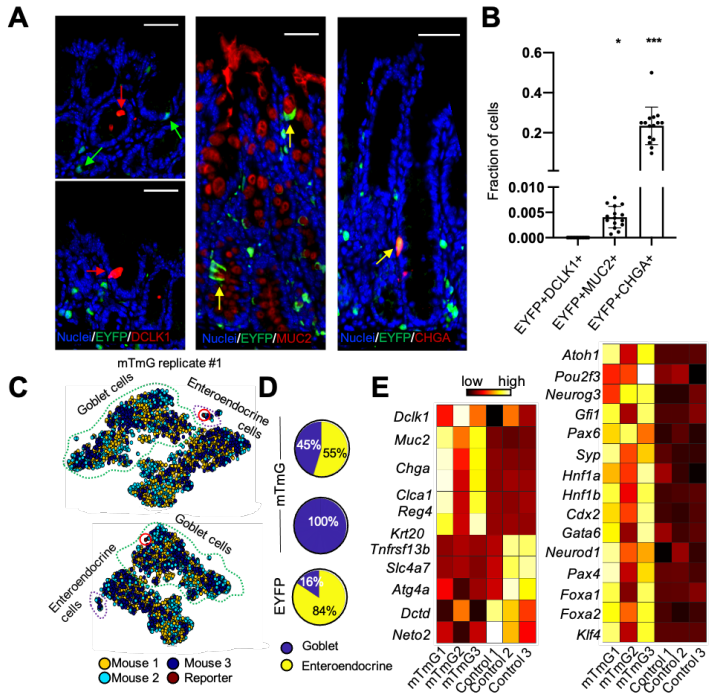

Fig 5.4. *Mist1*-expressing cells are secretory progenitors. (A) Representative IF images of reporter co-expression with cell type specific markers, DCLK1 for tuft cells, MUC2 for goblet cells, and CHGA for enteroendocrine cells, after 24 hours of lineage tracing in Mist1$^{CreERT2/+}$; *R26R*$^{LSL\text{-}EYFP/+}$ mouse colons. Arrows point to single positive (green/red) or double positive (yellow) cells. (B) Quantification of double positive cells compared to single positive cells for each marker. Each dot represents a field of view. Error bars represent SEM from n=3 animals, *p-value<0.05, and ***p-value<0.001. (C) Combined t-SNE embedding of bulk RNA sequenced *Mist1* reporter (mTmG)-expressing cells (solid circle in red) with n=3 reference murine colonic scRNA-seq dataset (colored dots from different mice). Goblet (green) and enteroendocrine (magenta) cell populations are delineated by dotted lines. (D) Quantification of *Mist1* reporter (EYFP or mTmG)-expressing cells co-embedding with different cell types using boot-strapped t-SNE runs. n=3 independent experiments. (E) Differential gene expression of cell type markers (left) and transcription factors (right) comparing reporter-expressing cells with non-expressing cells, both flow sorted for EPCAM. n=3 independent experiments. *Contribution from Chen B, Simmons AJ, Southard-Smith A, Lau KS*

cell type marker and transcription factor expression in *Mist1* reporter-expressing cells. There is a significant increase of *Muc2, Clca1, Chga*, and *Reg4*, and a moderate increase of *Dclk1*, all secretory cell type markers in the colon compared to unsorted epithelial cell controls (Fig 5.4E). *Krt20,* a marker of cellular differentiation, is also increased compared to controls (255), while *Tnfrsf13b, Slc4a7, Atg4a, Dctc,* and *Neto2*, known to be expressed indiscriminately in colonic epithelial cells (Fig 5.4E, and Fig 5.3K), are comparatively enriched in unsorted cells. There is an increase of the master secretory cell transcription factor *Atoh1* (47,256,257) in Mist1 reporter-expressing cells (Fig 5.4E). Consistent with expression of cell type markers, the tuft cell specific transcription factor *Pou2f3,* is moderately increased while enteroendocrine and goblet cells differentiation transcription factors *Neurog3 and Gfi1*, respectively, are significantly increased compared to controls (ref. 44; Fig 5.4E). Moreover, reporter expressing cells have increased expression of enteroendocrine specific transcription factors *Pax6, Syn, Hnf1a, Hnf1b, Cdx2, Gata6, Neurod1* and *Pax 4* (refs. 44–47; Fig 5.4E), transcription factors determining goblet cell and enteroendocrine fates *Foxa1* and *Foxa2,* and goblet cell-specific transcription factor *Klf4* (refs. 45,46; Fig 5.4E). These results reveal *Mist1* reporter-expressing cells to be secretory progenitor cells subsuming both goblet and enteroendocrine fates, but may be biased towards enteroendocrine differentiation.

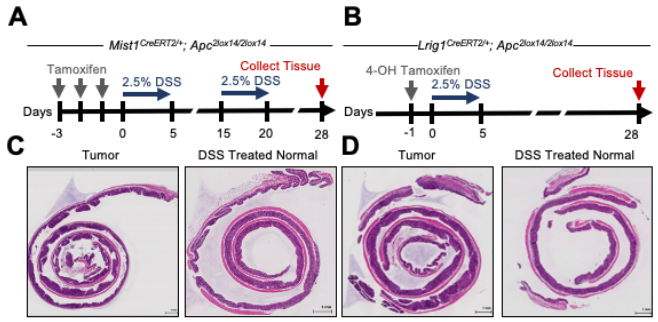

Fig 5.5: **Damage-induced non-stem cell and stem cell driven colonic tumors have similar histologies**. Experimental timelines of damage-induced tumor induction in (A) *Mist1*$^{CreERT2/+}$; *Apc*$^{2lox14/2lox14}$ and (B) *Lrig1*$^{CreERT2/+}$; *Apc*$^{2lox14/2lox14}$ models. (C-D) Swiss rolls depicting the entire colon of the two tumor models, respectively, and DSS treated control (same genotypes without induction). *Contribution from Markham N, TPSR, DHSR*

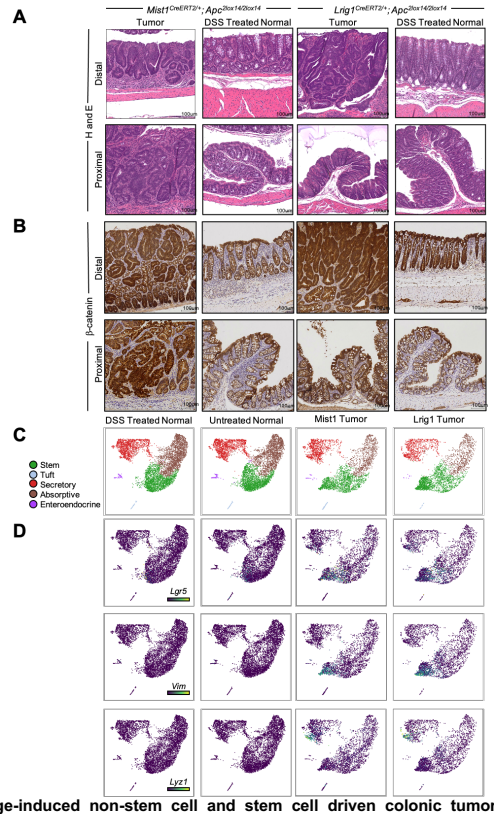

Fig 5.6. Damage-induced non-stem cell and stem cell driven colonic tumors have similar histologies but different cellular makeups. Representative H&E (A) and b-catenin IHC (B) of distal (top) and proximal (bottom) colons isolated from induced *Mist1*$^{CreERT2/+}$*; Apc*$^{2lox14/2lox14}$ mice (first column, n=4 animals; low grade dysplasia), uninduced *Mist1*$^{CreERT2/+}$*; Apc*$^{2lox14/2lox14}$ controls (second column, n=3; no dysplasia), induced *Lrig1*$^{CreERT2/+}$*; Apc*$^{2lox14/2lox14}$ mice (third column, n=4; advanced dysplasia), and uninduced *Lrig1*$^{CreERT2/+}$*; Apc*$^{2lox14/2lox14}$ controls (fourth column, n=3; no dysplasia), all 28 days after DSS. (C) Combined UMAP embedding of epithelial scRNA-seq data generated from colonic tissues, with each panel displaying data points from each condition (n=3 animals per condition – columns: control colons 28 days after DSS, untreated controls, Mist1 tumors, and Lrig1 tumors). Overlays indicate Leiden clustering labeled by cell populations. (D) Overlay of specific markers on UMAPs. *Contribution from Markham N, Chen B, Simmons AJ, Southard-Smith A, Lau KS, TPSR, DHSR*

Mist1-expressing and _Lrig1_-expressing cells both give rise to colonic tumors with biallelic recombination of _Apc_ in the presence of damage

Previous work has shown that committed secretory cells can serve as facultative stem cells upon damage and give rise to tumors (54,56,57,59,66,67). We showed that *Mist1*-expressing cells are likely committed secretory progenitors in the colon, and thus, we induced tumorigenesis using biallelic recombination of *Apc* (*Mist1*$^{CreERT2/+}$*; Apc*$^{2lox14/2lox14}$) followed by 2.5% DSS damage, with this model serving as a non-stem cell-of-origin tumor model (Fig 5.5A). In comparison, we induced the same genetic event in stem cells using *Lrig1*$^{CreERT2/+}$*; Apc*$^{2lox14/2lox14}$ mice via focal 4-hydroxytamoxifen delivery into the colon wall, followed by DSS damage (Fig 5.5B). Biallelic loss of function of the *Apc* gene coupled to DSS damage resulted in tumors from both stem (*Lrig1*+) and non-stem (*Mist1*+) cells-of-origin (Fig 5.6A-B, and Fig 5.5C-D). *Mist1*+ cell-derived tumors (Mist1 tumors) were observed in both the proximal and distal colon, while *Lrig1*+ cell-derived tumors (Lrig1 tumors) were observed only in the distal colon due to the focal induction (Fig 5.6A-B). Blind histological assessment of Mist1 and Lrig1 tumors collected after 28 days of induction revealed that Lrig1 tumors are high-grade dysplastic lesions while Mist1 tumors are classified as low grade (Table 5.1). These results demonstrate that while both *Mist1*-expressing non-stem cells and *Lrig1*-expressing stem cells can initiate tumors in the colon, Lrig1 tumors are more advanced in a shorter time frame.

Mist1 tumor cells have reduced stem capacity compared to Lrig1 tumor cells

While Mist1 tumors and Lrig1 tumors exhibit different grades, their gross histopathological features appear similar by eye. To identify cellular and molecular features differentiating the two tumor types, we applied scRNA-seq on harvested tumor tissues, along with two control conditions (colons after DSS recovery and untreated normal colons). Combined UMAP analysis of the epithelial compartment of the four conditions revealed that the cellular distributions of colons recovered from DSS largely overlap with those of untreated normal colons, consistent with full return to homeostasis after 28 days of recovery from DSS (Fig 5.6C-D, and Fig 5.7A-B). Tumors with only *Apc* loss-of-function mutations, including those in our study, are early stage adenomas, and they maintain a differentiation hierarchy with clear absorptive and secretory cell lineages (Fig 5.6C-D, and Fig 5.7A-B). Two salient cellular features differentiate tumor from normal epithelial tissues. First, tumor cells of the secretory lineage contain a unique subpopulation of Lysozyme (*Lyz1)*-expressing Paneth-like cells distinct from deep crypt secretory cells of the normal colon, consistent with lysozyme re-expression in neoplastic/metaplastic human colonic tissues (refs. 49–51; Fig 5.6D, and Fig 5.7B). Second, tumors possess distinct stem cell populations, which we term tumor stem cells (TSCs), with upregulated *Lgr5* expression and expression of *Vim* not found in normal colonic stem cells (Fig 5.6D). These results highlight the similarities and differences between epithelial cells of the normal colon and early neoplastic lesions driven by *Apc* mutation.

To characterize TSCs arising from Mist1 non-stem and Lrig1 stem cells, we performed p-Creode analysis on scRNA-seq data in order to evaluate the output of differentiated cells

Genotype	*Mist1*$^{CreERT2/+}$; *Apc*$^{2lox14/2lox14}$							*Lrig1*$^{CreERT2/+}$; *Apc*$^{2lox14/2lox14}$						
Mouse #	547	154	261	3134	3211	3212	3213	1978	1982	3468	3606	3455	3452	1985
Treatment	Tamoxifen; DSS				DSS			4OH Tamoxifen; DSS				PBS; DSS		
Grade of dysplasia	2	2	2	2	0	0	0	4	4	4	4	0	0	0

Table 5.1 Stem cell driven tumors are a higher grade than non-stem cell driven tumors. Histological scoring of tissues of multiple biological replicates of Mist1- and Lrig1- tumors along with uninduced controls. 0: none; 1: unicrypt; 2: low; 3: high, 4: advanced. *Contribution from Washington K*

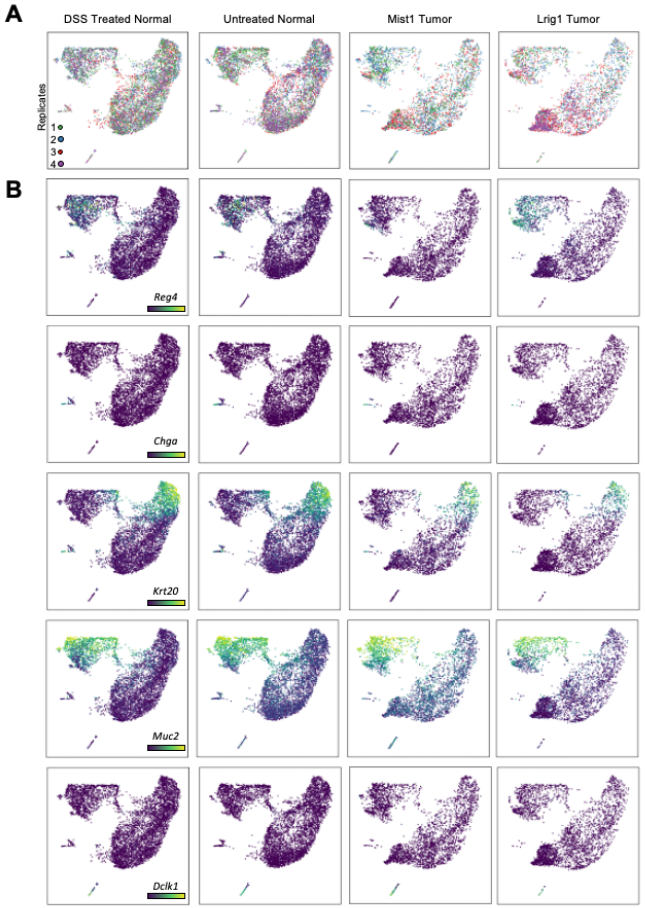

Fig 5.7 Damage-induced non-stem cell and stem cell driven colonic tumors have different cellular makeups. (A) Combined UMAP embedding of epithelial scRNA-seq data generated from colonic tissues, as in Fig 5.6C. Overlay represents different biological replicates (mice) to demonstrate minimal batch effects. (B) Overlay of cell type markers on UMAPs. *Contribution from Chen B, Simmons AJ, Southard-Smith A, Lau KS*

from the TSCs of the two tumor types. Comparative analysis between the two p-Creode maps showed that Lrig1 TSCs are highly represented compared to Mist1 TSCs, as denoted by the sizes of nodes representing comparative cell density (Fig 5.8A). In contrast, Mist1 TSCs have stronger secretory lineage outputs (tuft and goblet cells) compared to Lrig1 (Fig 5.8A). Paneth-like cells, which support stem cells (44,200) and can be directly differentiated from stem cells (243), are overrepresented in Lrig1 tumors (Fig 5.8A). We also performed a supervised cellular proportion analysis on Mist1 and Lrig1 tumors to confirm these quantitative results. K-means was used to partition the continuous cell state space into non-overlapping clusters, and the clusters were then grossly grouped into four groups based on canonical markers expression: secretory, absorptive, stem, or transitioning (Fig 5.9A). Within these groups, we calculated the proportion of clusters that are represented by Mist1 tumor cells versus Lrig1 tumor cells (Fig 5.9B). Transitioning, secretory, and absorptive groups are skewed towards Mist1 tumors, with 60%, 71%, and 60% of the clusters overrepresented by Mist1 tumor cells, respectively (Fig 5.8B). In contrast, the stem cell group was overwhelmingly represented by Lrig1 tumor clusters, with 100% of the clusters being Lrig1-skewed (Fig 5.8B). These results imply that Lrig1 TSCs have either increased stem cell maintenance capacity or proliferation, while Mist1 TSCs have increased propensity to differentiate. Intestinal and colonic stem cells differentiate by first transitioning into transit amplifying cells, which proliferate at higher rates (264). A larger portion of Mist1 TSCs express gene signatures of the cell cycle (Fig 5.9C), suggesting that the overrepresentation of Lrig1 TSCs is due to increased stem capacity and not proliferation. To evaluate the intrinsic stem capacity of the two TSC types from scRNA-seq data (265). CytoTRACE, when applied to normal

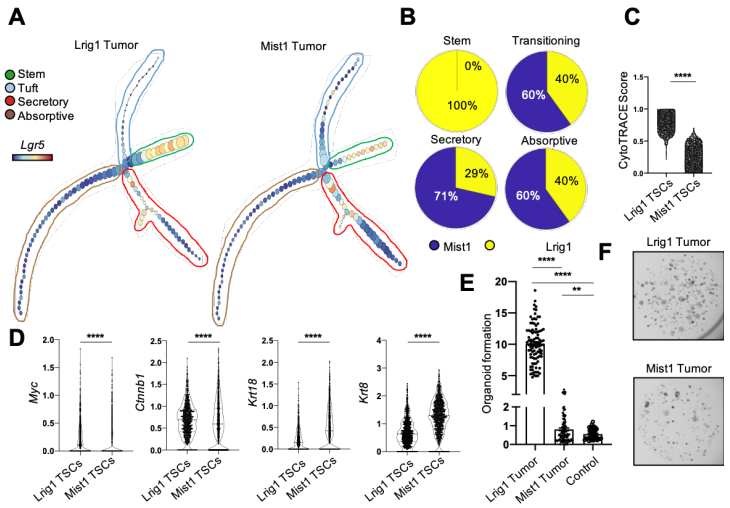

Fig 5.8. Stem cell driven tumors have additional stem capacity compared to non-stem cell driven tumors. (A) p-Creode trajectory map of Lrig1 (left) and Mist1 (right) tumors constructed from scRNA-seq data. Size of node corresponds to the comparative cellular density of that cell lineage between tumor types. n=3 scRNA-seq datasets for each condition. (B) The fraction of Lrig1 or Mist1 tumor cells within K-means clusters identified as stem, secretory, transitioning, or absorptive, generated from scRNA-seq. (C) CytoTRACE score, a measure of stemness, for Lrig1 and Mist1 TSCs calculated from scRNA-seq. ****p<0.0001. (D) Normalized gene expression of *Myc, Ctnnb1, Krt18*, and *Krt8* for Lrig1 and Mist1 TSCs from scRNA-seq. ****p<0.0001. (E) Normalized organoid formation efficiency of single cells isolated from Lrig1 tumors, Mist1 tumors, and control colons. Each dot represents a well of 24-well plate. Error bars represent SEM from n=4 animals per tumor, 2 for control, ****p<0.0001, **p<0.01. (F) Representative images of 1 well of organoid formation of single cells isolated from Lrig1 and Mist1 tumors. *Contribution from Chen B, Simmons AJ, Southard-Smith A, Lau KS*

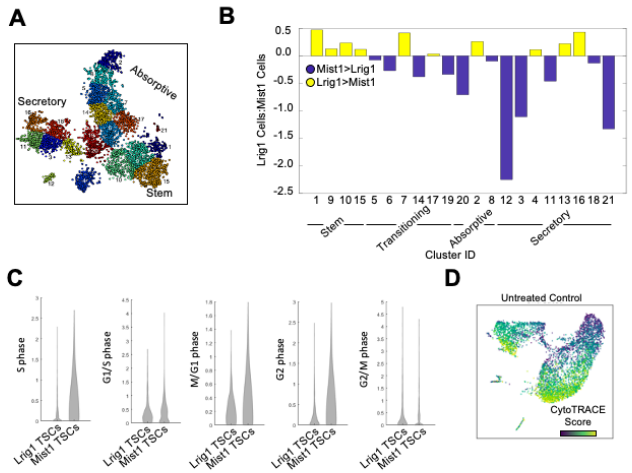

Fig 5.9: Stem cell driven tumor have increased stem capacity compared to non-stem cell driven tumors. (A) K-mean clustering displayed as a combined t-SNE embedding of epithelial cells from Lrig1 and Mist1 tumors. (B) The ratio of Lrig1 tumor cells to Mist1 tumor cells of each cluster (numbered) shown in A grouped by gross cell type classification. (C) Normalize metagenes for different cell cycle phases of Lrig1 and Mist1 TSCs. (D) CytoTRACE score overlay on UMAP of untreated control colonic epithelium to delineate stem cell capacity and differentiation. *Contribution from Chen B, Simmons AJ, Southard-Smith A, Lau KS*

colon data, is consistent with the expected view of epithelial differentiation, with stem cells having the highest CytoTRACE score, diminishing through transitioning cells towards colonocytes and goblet cells (Fig 5.9D). Lrig1 TSCs have a significantly higher CytoTRACE score than Mist1 TSCs, implicating that Lrig1 TSCs have higher stem capacity on a per cell basis (Fig 5.8C). We also evaluated individual genes that define the epithelial stem cell differentiation continuum. Stem cell associated genes, *Myc* and *Ctnnb1*, are upregulated in Lrig1 TSCs, while differentiated cell associated genes, *Krt8* and *Krt18,* are upregulated in Mist1 TSCs (Fig 5.8D). Taken together, these properties are consistent with the cell-of-origin of dictating TSC phenotype, with Lrig1 TSCs, derived from stem cells, having higher stem capacities, and Mist1 TSCs, derived from non-stem secretory cells, having more propensity for secretory differentiation.

To experimentally validate the difference in stem capacity of the two TSC types, we performed organoid formation assays from single tumor cells. Organoid forming culturing conditions enable cells with stem cell characteristics to continuously self-renew and differentiate, resulting in robust generation of organoids. Cells with less stem capacity must first meet the right conditions to revert back to a stem state, resulting in decreased organoid formation (60). Lrig1 tumor cells formed significant more organoids than Mist1 tumor cells (Fig 5.8E, and 8F). These results support our single-cell analysis and demonstrate the difference in stem capacity between TSCs derived from different origins.

Mist1 tumor stem cells exhibit increased ability to present antigens and activate T cells compared to Lrig1 tumor stem cells

Previous work has shown that *Lgr5*+ small intestinal stem cells can be classified into 3 subpopulations (ISCI, ISCII, ISCIII) that exist on a gradient of stem capacity. ISCII and ISCIII possess more differentiation characteristics and were found surprisingly to present antigens (35). Because TSCs from Mist1 tumors and Lrig1 tumors exhibit different stem capacity, we hypothesize that TSCs derived from different origins also have different abilities to present antigen, in turn, affecting the tumor microenvironment. We derived metagenes from the Biton *et al.* study and compared these signatures between Mist1 and Lrig1 TSCs. Lrig1 TSCs exhibit a higher ISCI score, while Mist1 TSCs exhibit a higher ISCII and ISCIII score, again reflecting differences in stem capacity and differentiation characteristics (Fig 5.10A). Gene set enrichment analysis comparing Mist1- with Lrig1-TSCs demonstrated significant enrichment of genes associated with immune-mediated processes expressed in Mist1 TSCs, with antigen presentation being one of the top hits (Fig 5.11A-B). Remarkably, Mist1 TSCs have an increased expression of MHC class II antigen presentation machinery, both at the metagene level and at the single-cell level, consistent with their classification into the ISCII/III subgroups (Fig 5.10B-C, and Fig 5.12A). Control and damage-recovered stem cells of the normal colon have higher MHCII and ISCII/III metagene scores than either TSC types, suggesting that suppression of antigen presentation may correlate with dysplastic progression (Fig 5.12B-C).

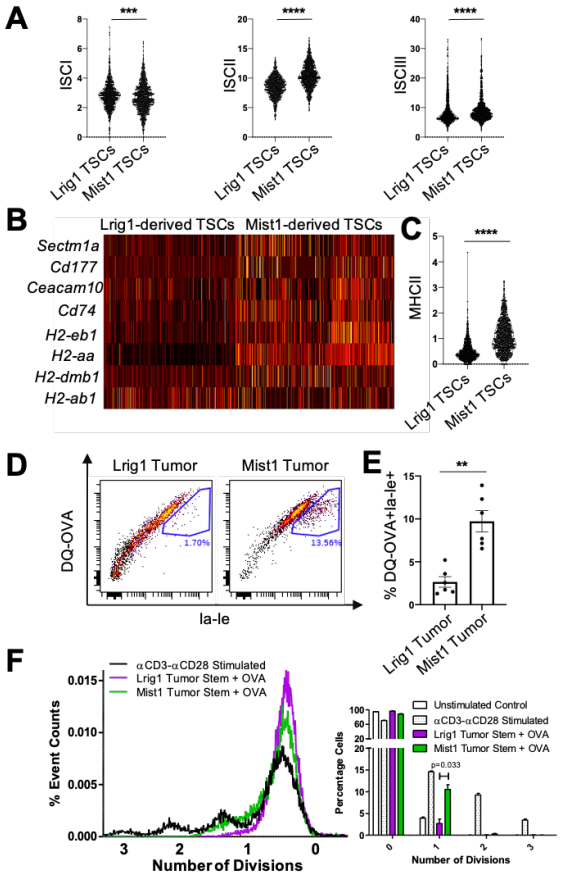

Fig 5.10. Mist1 TSCs express MHC II machinery and present antigens. (A) Normalized metagene expression of ISCI, ISCII, and ISCIII for Lrig1 and Mist1 TSCs derived from scRNA-seq. ****p<0.0001, ***p<0.001. (B) Individual MHCII gene expression at the single-cell level. (C) Normalized MHCII metagene expression for Lrig1 and Mist1 TSCs. ****p<0.0001. (D) Representative flow cytometry plots of DQ-OVA+Ia-Ie+ epithelial cells comparing antigen processing and presentation abilities between Lrig1- and Mist1- tumoroids. (E) Quantification of C. Error bars represent SEM from n=6 animals per condition, **p<0.01. *Contribution from Simmons AJ, Southard-Smith A, Goettel JA, Lau KS*

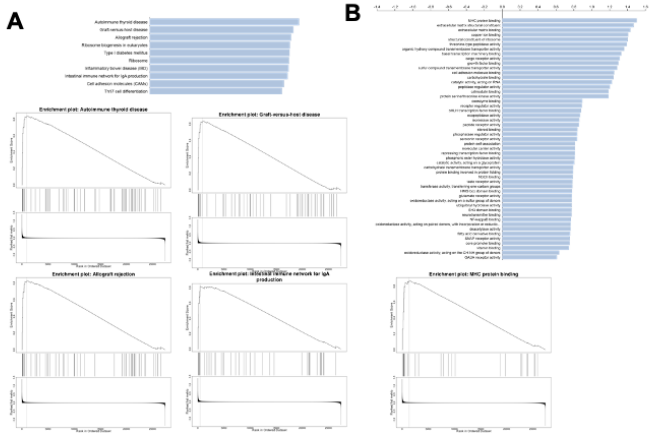

Fig 5.11: Mist1 TSCs have enrichment of genes associated with immune- mediated processes. GSEA top categories and selected enrichment plots generated using (A) KEGG or (B) Gene Ontology Molecular Function. *Contribution from Chen B, Simmons AJ, Southard-Smith A, Lau KS*

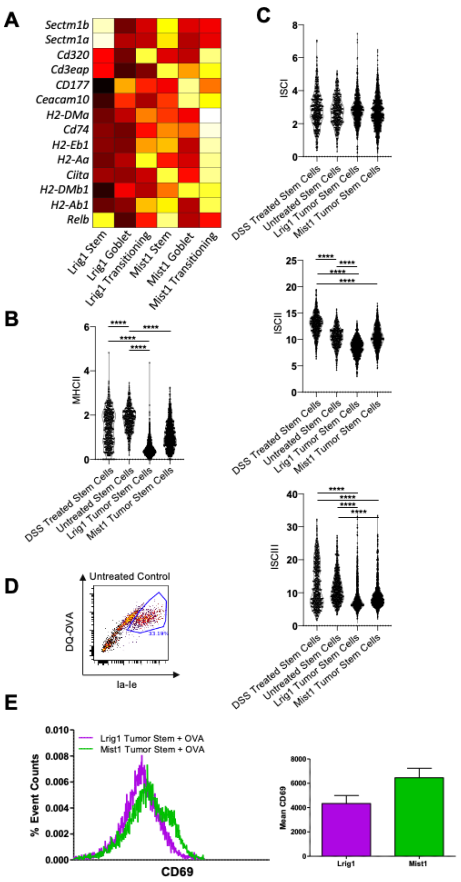

Fig 5.12: Mist1 TSCs exhibit more MHCII mediated antigen processing and presenting machinery. (A) Pseudo-bulk gene expression analysis of selected MHCII genes for Lrig1 and Mist1 TSCs, and goblet and transitioning cells from the respective tumors. Normalized metagene for (B) MHCII expression and (C) ISC categories of control colons 28 days after DSS, untreated controls, Mist1 tumors, and Lrig1 tumors. n=3 biological replicates per group, ****p<0.0001. (D) Representative flow cytometry plot of DQ-OVA+Ia-Ie+ cells from untreated control colonoids. *Contribution from Simmons AJ, Southard-Smith A, Goettel JA, Lau KS*

To demonstrate that expression of MHC class II machinery actually reflects function, we performed *in vitro* antigen processing and presentation assays in Lrig1- and Mist1- tumor derived organoids (tumoroids). Tumoroids were maintained in stem cell maintenance media and exposed to the MHCII antigen DQ-Ovalbumin (DQ-OVA). We assayed for the ability of cells to endocytose and proteolytically degrade the antigen, which results in green fluorescence. Additionally, the presentation of antigens at the cell surface can be evaluated by Ia/Ie surface staining. Using flow cytometric analysis, Mist1-driven tumoroids were shown to process and present more OVA antigens than Lrig1-driven tumoroids (Fig 5.10D-E, and Fig 5.12D). These results are consistent with MHCII gene expression of TSCs and suggests increased interaction of Mist1 TSCs with the immune system compared to Lrig1 TSCs.

To show that increased MHCII antigen presentation actually results in differential effects on T cells, we performed *in vitro* antigen-specific T cell activation assays. Mist1- or Lrig1-derived tumoroid cells were loaded with OVA peptide and then co-cultured with naïve OTII CD4+ T cells, which specifically recognize OVA peptide through a MHCII mechanism. T cells were then cytometrically assayed for proliferation through CellTrace violet, indicative of their activation states. OTII T cells co-cultured with Mist1-derived tumoroids showed higher proliferation than those co-cultured with Lrig1-driven tumoroids (Fig 5.10F, and Fig 5.12E). Taken together, these results demonstrate that TSCs derived from different origins have different abilities to process and present antigens, leading to differential T cell activation. In turn, increased antigen-specific T cell activation by Mist1 TSCs may present a more active, favorable immune microenvironment.

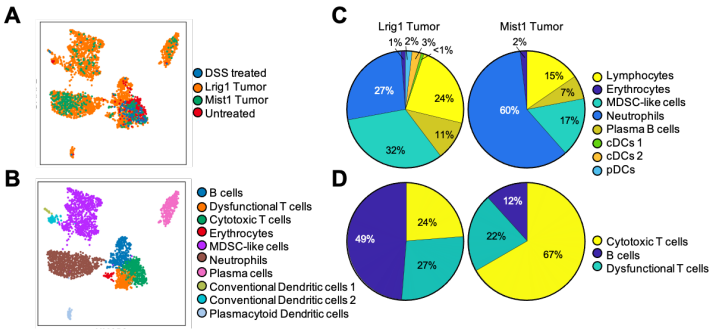

Fig 5.13. Mist1 tumors have a cytotoxic immune microenvironment while Lrig1 tumors are immunosuppressive. (A) Combined UMAP embedding of scRNA-seq data of immune cells generated from colonic tissues, with colored dots representing cells from different conditions. n=3 scRNA-seq datasets for each condition. (B) Overlays indicating Leiden clustering labeled by cell populations. Quantification of general immune cell types (C) and specific lymphocyte populations (D) within Lrig1 (left) and Mist1 (right) tumors. *Contribution from Chen B, Simmons AJ, Southard-Smith A, Lau KS*

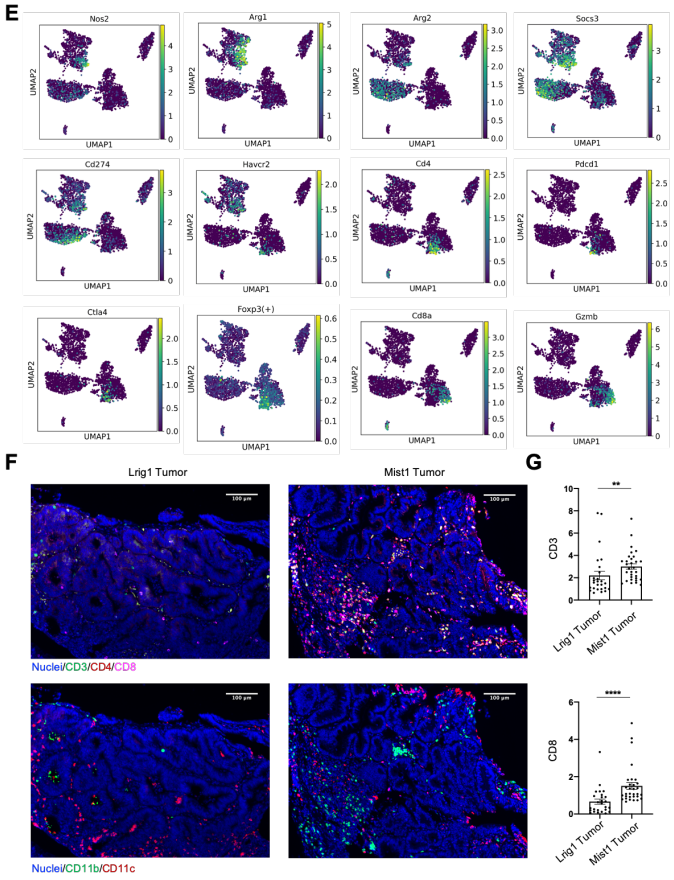

Fig 5.13. Continued (E) Overlay of specific markers on UMAPs delineating immunosuppression or cytotoxicity in myeloid and lymphoid cell lineages. (F) Representative MxIF images of Lrig1 (left) and Mist1 (right) tumors with markers delineating T cells (top) and myeloid cells (bottom). (G) Normalized quantification of CD3+ and CD3+CD8+ cells per tumor area in Lrig1 and Mist1 tumors. Each dot represents a field of view. Error bars represent SEM from n=3 animals per group, ****p<0.0001, **p<0.01. *Contribution from Chen B, Simmons AJ, Southard-Smith A, Macedonia MC, Lau KS*

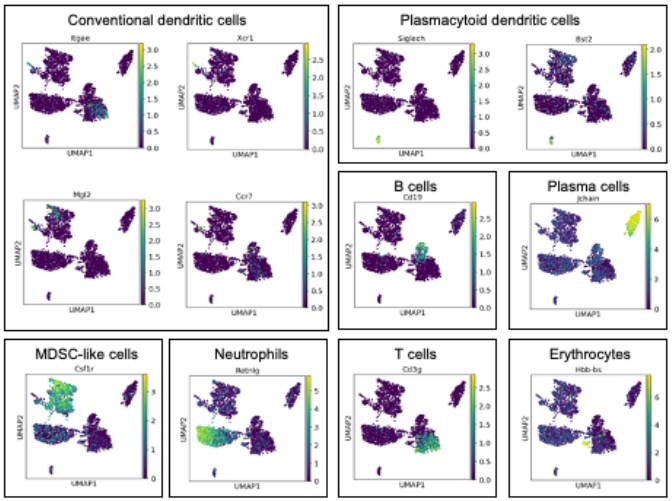

Fig 5.14: **Immune cell type specific markers.** Combined UMAP embedding of non-epithelial cells from Lrig1 and Mist1 tumors. Overlays are immune cell type specific markers. *Contribution from Chen B, Simmons AJ, Southard-Smith A, Lau KS*

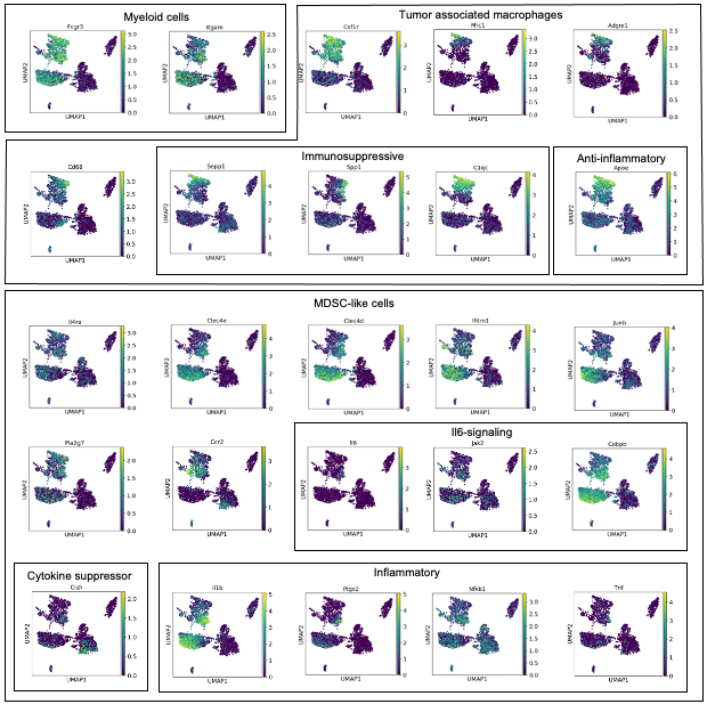

Fig 5.15: Tumor specific myeloid cell specific markers. Combined Lrig1 and Mist1 tumor Umaps showing selected gene expression. *Contribution from Chen B, Simmons AJ, Southard-Smith A, Lau KS*

The Mist1 tumor microenvironment is skewed towards anti-tumor, adaptive responses while Lrig1 tumors possess a suppressive myeloid environment

Antigen presentation is associated with a favorable cytotoxic immune microenvironment, as seen in tumors with high mutational loads. High MHCII antigen presentation can directly activate CD8 T cells through cross-presentation (266,267), as well as amplify cytotoxic response through CD4+ T helper cells (Th1; refs. 59–61). Because Mist1 TSCs have an increased ability to present antigens and activate T cells compared to Lrig1 TSCs, we surmised that Mist1 tumors should exhibit a more immuno-active microenvironment. From our scRNA-seq data, we observed that Lrig1 tumors are overrepresented by myeloid cells, defined by *Fcgr3 (CD16)* and *Itgam (CD11b)*, compared to Mist1 tumors (Fig 5.13A-D, and Fig 5.14-15). Lrig1 tumors have increased tumor associated macrophages (TAMs), known to promote tumor progression, and can be identified in our dataset by *Csf1r, Mrc1 (CD206), Adgre1 (F4/80),* and *Cd68* (ref. 62; Fig 5.13A-D, and Fig 5.15). These cells express markers of immune suppressive TAMs, as identified in recent human CRC studies, including *Sepp1* (272), *Spp1* (Osteopontin; refs. 64,65), *C1qc* (275), and anti-inflammatory *Apoe* (ref. 67; Fig 5.15). Furthermore, Lrig1 tumors have increased infiltration of myeloid cells that cannot be classically defined but resembled myeloid derived suppressive cells (MDSCs; Fig 5.13A-D, and Fig 5.14). MDSCs are specific to tumors, retain characteristics of macrophages, dendritic cells, and granulocytes, and suppress the function of immune cells to create a suppressive environment for the tumor to flourish (89). Monocytic MDSCs have been defined previously by scRNA-seq (277) and our MDSC-like cells express similar markers (*Il4ra, Clec4e, Clec4d, Ifitm1, Junb, Pla2g7, Ccr2, Spp1*; refs. 70,71; Fig 5.15). Specifically,

mixed expression of M1 (*Nos2* - iNos) and M2 (*Arg1, Arg2*) was detected in this subpopulation, characteristic of MDSCs (refs. 72,73; Fig 5.13E). MDSCs were thought to arise from chronic, dysregulated IL6 signaling that reinforces an immature state (89,282). Lrig1 tumor MDSC-like cells express components of the Il6 signaling pathway such as *Il6* and *Jak2, Cebpb (C/EBPbeta)* transcription factor downstream of cytokine signaling (283,284), as well as suppressors of cytokine signaling (*Socs3, Cish*) expressed as feedback mechanisms to active signaling (refs. 73,74; Fig 5.13E, and Fig 5.15). Consequently, inflammatory genes are also enriched in this population (*Il1b, Ptgs2 (Cox2), Nfkb1, Tnf*; ref. 68), as well as secreted factors (*Cxcl2, Vegfa*) shown previously to further promote immune suppression (refs. 66,77; Fig 5.15-S10). At last, this population also expresses classic immuno-suppressive markers such as (*Cd274, Havcr2, Prdm1, Id2, Nfil3; refs.* 1,78–81; Fig 5.13E, and Fig 5.16). On the granulocytic side, Lrig1 tumor neutrophils contain a subset that expresses *Cd274* (PDL1), which are absent in Mist1 tumors (ref. 82; Fig 5.13E). These expression profiles imply that Lrig1 tumors possess an immune environment skewed towards suppression characterized by higher representation of MDSC-like cells compared to Mist1 tumors. In line with the immune-suppressive environment, Lrig1 tumors include a population of dysfunctional T cells that is absent in Mist1 tumors. T cell dysfunction can result from anergy or exhaustion that ultimately results in immunosuppression (95,291–293). These cells are CD4+ T cells that express immunosuppressive markers, the most prominent being *Pdcd1* (PD1; ref. 80), *Ctla4* (294), *Prdm1* (295), and *Havcr2* (TIM3; ref. 89; Fig 5.13A-E, and Fig 5.16). Other markers that implicate a suppressed phenotype include *Socs3* and *Cish* downstream of JAK-STAT signaling and *Id2* downstream of TGFβ signaling (Fig 5.13E,

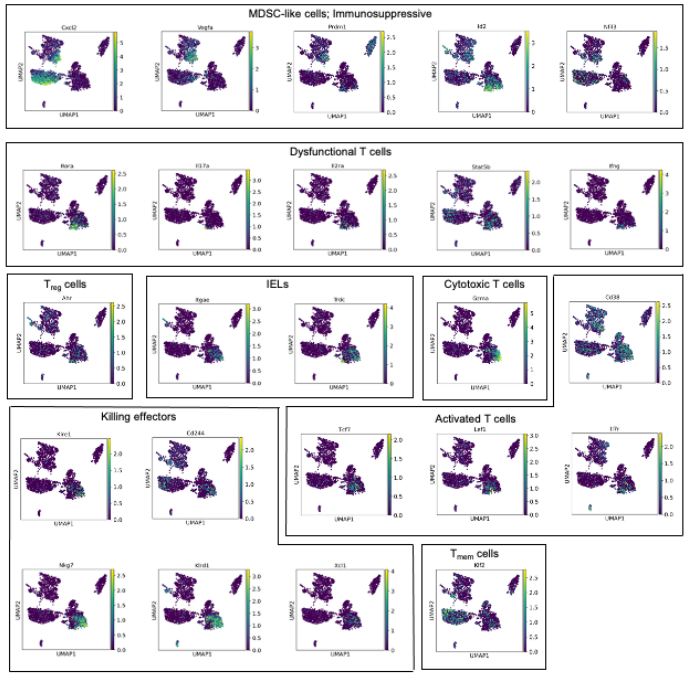

Fig 5.16: Immunosuppressive and T cell specific markers. Combined Lrig1 and Mist1 tumor Umaps showing selected gene expression. *Contribution from Chen B, Simmons AJ, Southard-Smith A, Lau KS*

and Fig 5.15-16). TGFβ and cytokine signaling can lead to RORα-dependent tumor-promoting inflammation, evident in this population by *Rora* and *Il17a* expression (ref. 86; Fig 5.16). Maintained *Il2ra* and *Stat5* expression during T cell dysfunction has also been reported while dysfunctional T cell *Ifng* secretion maintains a muted immune response (refs. 83–86; Fig 5.16). Furthermore, *Il2ra* and *Ahr*, markers for Tregs (272,298), and target genes part of the *Foxp3* regulon are upregulated in subpopulation, indicating immune suppression (Fig 5.13E, and Fig 5.16).

Conversely, Mist1 tumor T cells are overrepresented by CD8+ cytotoxic cells (Fig 5.13A-E). These cells cluster with intraepithelial lymphocytes (IEL) from control colons and express IEL markers *Itgae* and *Trdc* (TCRdelta; refs. 92,93; Fig 5.16); IELs exhibit cytotoxic functions against epithelial cells compromised by pathogens (301). These cells express *Gzma* and *Gzmb* that play key roles in cytotoxicity (Fig 5.13E, and Fig 5.16), markers of T cell activation (*Cd38, Tcf7, Lef1, Il7r*), and the killing effectors *Klre1* (302), *Cd244* (when expressed at the appropriate level; ref. 96), *Nkg7, Klrd1, and Xcl1* (ref. 63; Fig 5.16). *Klf2* expression is also detected in these active cells that regulate the homing and memory potential of CD8 T cells (ref. 97; Fig 5.16). These expression profiles implicate that these Mist1 tumor-enriched CD8+ T cells are active and primed for cytotoxicity.

Recent studies have shown the importance of spatial localization of immune cells in controlling tumor response (22). To validate scRNA-seq findings and to visualize the localization of these immune cells, we utilized multiplexed immunofluorescence imaging

to quantify lymphocytes and myeloid cells that infiltrated into the tumor and excluded those that reside in the peritumor space (Fig 5.17A). In Mist1 tumors compared to Lrig1 tumors, there is a significantly higher number of tumor-infiltrating cytotoxic T cells (CD3+/CD8+), but not helper T cells (CD3+/CD4+), leading to a higher overall CD3+ T cell count (Fig 5.13F-G, and Fig 5.17B). Conversely, Lrig1 tumors have a higher infiltration of B220+ B cells, consistent with scRNA-seq data, and their CD11b+ and CD11c+ myeloid cells also trend higher (Fig 5.13F-G, and Fig 5.17B). These results are consistent with scRNA-seq data and implicate that Mist1 tumors have an immune microenvironment skewed towards cytotoxicity, more similar to tumors with high mutational burden, while Lrig1 tumors have characteristics of myeloid suppression and T cell dysfunction.

Discussion

Here, we show that *Mist1*-expressing cells are secretory progenitor cells with minimal stem capacity under damage conditions compared to traditional colonic stem cells. Moreover, tumors derived from *Mist1*-expressing cells maintain characteristics of the cell-of-origin that are different from tumors derived from *Lrig1*-expressing cells. These differences are evident in TSC stem capacity and antigen presentation ability contributing to a favorable immune microenvironment skewed towards an active cytotoxic response and away from immune suppression in Mist1 tumors. We reveal *Mist1*-expressing cells to be a common secretory cell progenitor biased towards enteroendocrine cells. MIST1 (BHLHA15) is a transcription factor found in secretory cells in the GI, such as intestinal Paneth cells, pancreatic acinar cells, gastric chief cells, and plasma cells (148,150,305).

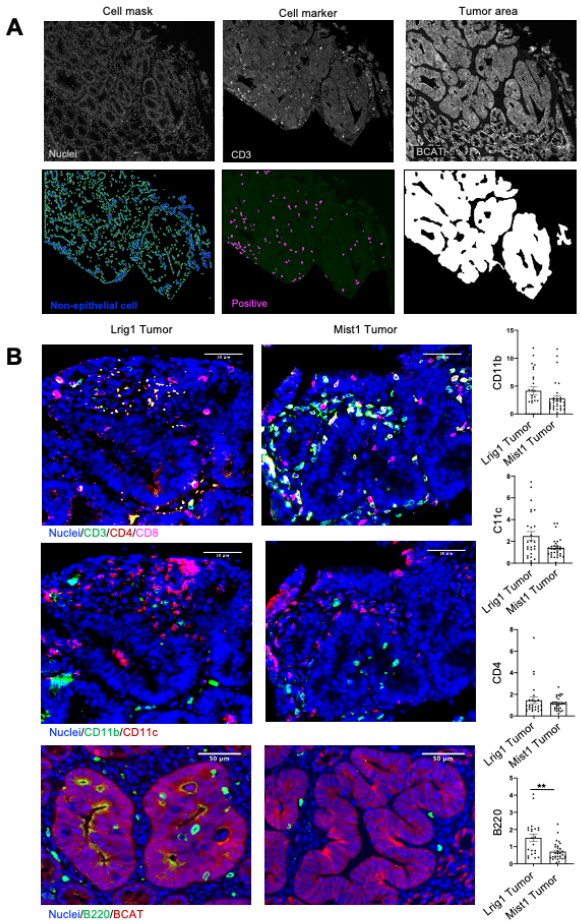

Fig 5.17: Lrig1 tumors are immunosuppressive. (A) Representative quantification of MxIF images using protein expression (top) to create masks (bottom) for image quantification. (B) Representative images for tumor infiltrating immune cells in Lrig1 versus Mist1 tumors. (C) Additional quantification of immune cells from MxIF. Error bars represent SEM from n=3 animals, **p-value<0.01. Dots represent fields of view. *Contribution from Macedonia MC, Lau KS*

Recognized as an endoplasmic reticulum scaling factor, MIST1 controls the expansion of the protein production and trafficking machinery in cells specialized in the secretion of protein products. (150,251). Our damage-induced lineage tracing demonstrates that *Mist1*-expressing cells have minimal stem capacity under damage conditions. These results are consistent with other facultative stem cells. Hayawaka *et al* utilized the *Mist1*-driver with the tdTomato reporter to obtain a ~1% traced colonic glands under DSS-damage conditions. Under irradiation damage, *Dll1*-expressing early secretory progenitors lineage trace approximately ~2% of duodenum crypts while Dclk1-expressing tuft cells exhibit lineage tracing in less than ~1% of small intestinal and colonic crypts after irradiation or DSS-mediated damage, respectively (69). Moreover, *Alpi*-expressing absorptive progenitors lineage trace ~0.5% duodenum crypts when *Lgr5*-expressing stem cells are ablated (20), while *Nkx2.2*-expressing enteroendocrine cells, rarely lineage traced under damage (68). While these frequencies are significantly less than the 41.07% lineage traced colonic crypts from stem cells similar to our results, there are reports where significant numbers of crypts are lineage traced, for example, from Paneth cells when the intestine is damaged by doxorubicin (58). These differences can be attributed to biological differences between small intestinal and colonic cell populations, as well as differential abilities of different types of damage to induce different cell populations to fulfill the facultative stem cell role.

A major question remains: are different facultative stem cell types identical to each other and to traditional stem cells? Comparative transcriptomic profiling suggests that facultative stem cell populations are distinct. For instance, *Alpi*-expressing cells that

acquire stem capacity upon damage still express absorptive-specific genes and have enrichment of apoptosis and damage protective genes (20). This suggests that while non-stem cells may acquire stem capacity and resemble traditional stem cells in some phenotypic behaviors, they retain some epigenetic identity of its origins (307). Does the identity of a facultative stem cell, then, affect the resultant tumor originating from it? Our work and others have shown that stem and non-stem cell-driven tumors are histologically indistinguishable (67,151). However, our study demonstrates that differences between TSCs from different cell-of-origins are molecularly distinct. Mist1 TSCs have decreased stem capacity and increased propensity for secretory cell differentiation compared to Lrig1 TSCs, demonstrating that a remnant signature of the cell-of-origin is maintained through tumorigenesis. Decreased stemness of TSCs correlates with increased MHCII-mediated antigen presentation capabilities, consistent with recent reports describing these properties in different healthy intestinal stem cell populations (35). What remains to be addressed is whether antigen presentation ability is an intrinsic quality related to TSC differentiation or an extrinsic quality dependent on differential regulation of the immune microenvironment that subsequently influences stem cells. While the most direct explanation is intrinsic regulation driven by stem cell state as suggested by Biton et al., the intestine is a dynamic organ under constant perturbations from microbes and damage that stimulate the local immune microenvironment to interact with epithelial cells. IFN gamma signaling is a major microenvironmental pathway that induces MHCII expression via a JAK/STAT transcriptional program in various cell types (308). This pathway can interact non-autonomously with TSCs to reinforce antigen presentation, given that the tumor microenvironment is inflammatory. Extrinsic vs intrinsic regulation of MHCII in TSC

warrants further study in experimental systems that separately examine tumor cells and the microenvironment. These include tumoroid systems that can exclude or reconstitute the microenvironment, or transplant of tumor cells into mice with defined immune systems.

MHC antigen presentation regulates tumor cell interaction with the immune system. Thus, we have also revealed that non-stem cell-driven tumors with antigen presenting TSCs have more cytotoxic immune microenvironments than stem cell-driven tumors, which have more immune suppressive microenvironments. We show that muted cytotoxic microenvironments found in stem cell-driven tumors are accompanied by an influx of myeloid derived suppressor cells (MDSCs). MDSCs result from persistent inflammatory stimuli commonly observed in tumors, and they are a heterogeneous myeloid cell population with characteristics of macrophages, dendritic cells, granulocytes, and immature monocytes. They release reactive oxygen and nitrogen species and anti-inflammatory cytokines that suppresses the immune microenvironment which leads to T cell dysfunction (88,89). Immunotherapy has recently been approved for a wide variety of cancers but their efficacy is optimal in tumors with an intact immune response (309). It was previously shown that CRCs that have high mutational loads and are microsatellite instable (MSI) have better prognoses due to active immune surveillance (21,310). Current clinical practices also preselect MSI CRC patients to be candidates for immunotherapy treatment (22). The rationale behind these clinical decisions is that a high mutational burden creates a large antigenic load. Large numbers of “non-self” antigens get presented to adaptive immune cells, which then act to eliminate tumor cells. However, a recent study

by the Galon group showed that the MSI status of CRC does not predict patient survival, but instead, the immunoscore – a quantitative metric for immune cell infiltration – is a better predictor (22). Moreover, autophagy has recently been identified as a mechanism to downregulate antigen presentation machinery, which in turn suppresses the cytotoxic tumor microenvironment and promote progression of pancreatic tumors (311). Thus, the level of neoantigens is not a sufficient correlate to a cytotoxic immune response; the quality of antigen presentation is also an important contributing factor. Our work reveals that the origin of tumorigenesis may provide an important context by which the antigen presentation machinery of TSCs can be regulated, and sheds light on the mechanism of adaptive immune response suppression in tumors.

Methods

Murine lineage tracing

For homeostatic lineage tracing studies, *Lrig1*$^{CreERT2/+}$;*Rosa26*$^{LSL\text{-}EYFP/+}$ mice were injected intraperitoneally (i.p.) for 3 consecutive days with 2.5 mg tamoxifen (Sigma; T5648) in corn oil, while *Mist1*$^{CreERT2/+}$;*Rosa26*$^{LSL\text{-}EYF/+P}$ were injected i.p. for 3 consecutive days with 5 mg tamoxifen. Mice were euthanized 24 h, 10 days, and 28 days later. For damage-induced lineage tracing, *Mist1*$^{CreERT2/+}$;*Rosa26*$^{LSL\text{-}EYFP/+}$ and *Mist1*$^{CreERT2/+}$;*Rosa26*$^{mT/mG/+}$ mice were injected i.p. for 3 consecutive days with 5 mg tamoxifen, and were then administered 2.5% DSS (TdB Consultancy; Batches DB001-37, DB001-42) in drinking water for the following 6 days. After cessation of DSS, mice were euthanized 24 h, and 28 days later.

Induction of tumorigenesis using different promoters

Mist1$^{CreERT2/+}$;*Apc*$^{2lox14/2lox14}$ were injected i.p. for 3 consecutive days with 5 mg tamoxifen in corn oil, and were then administered 2.5% DSS in drinking water for the following 6 days, prior to a 9-day rest period, followed by a second round of DSS. *Lrig1*$^{CreERT/+2}$;*Apc*$^{2lox14/2lox14}$ were injected with 0.01μM 4-hydroxytamoxfin (Sigma; H6278) through colonoscopy-guided orthotropic injections into the mucosal lining of the distal colon (312), and were then administered a 2.5% DSS solution in the drinking water for the following 6 days. Control mice received PBS injections followed by DSS. Mice were euthanized approximately 28 days following Cre induction.

Immunofluorescence and histological imaging

Upon euthanasia of an animal, colonic tissue was removed, washed with 1X DPBS, spread longitudinally onto Whatman paper and fixed in 4% PFA (Thermo Scientific; J19943K2) overnight. Fixed tissues were washed with 1X DPBS, swiss-rolled, and stored in 70% EtOH until processing and paraffin embedding. Tissues were sectioned at 5 mm thick onto glass slides. Slides were processed for deparaffinization, rehydration, and antigen retrieval using citrate buffer (pH 6.0) for 20 minutes in a pressure cooker at 105°C followed by a 20-minute bench cool down. Endogenous background signal was reduced by incubating slides in 1% H_2O_2 (Sigma, 216763) for 10 minutes, before blocking for 30 minutes in 2.5% Normal Donkey Seurm (NDS) in 1X DPBS prior to antibody staining. Primary antibodies against GFP (1:1000; Novus; NB600-308SS), MUC2 (1:100; Santa

Cruz; sc15334), CHGA (1:100; Santa Cruz; sc1488), and DCAMKL1 (1:100; Abcam; ab109029) were incubated on the slides in a humidity chamber overnight, followed by three washes in PBS, and 1 hour incubation in Hoechst 33342 (1:10000; Invitrogen; H3570), and compatible secondaries (1:500; Life Technologies) conjugated to AlexaFluor (AF)-48, or AF-647. Slides were washed in 1X DPBS, mounted in Prolong Gold (Invitrogen; P36930) and imaged using a Zeiss Axio Imager M2 microscope with Axiovision digital imaging system (Zeiss, Jena GmBH, Germany). Multiplexed imaging was performed by using a multiplex iterative staining and fluorescence-inactivation protocol, as previously described (McKinley *et al*, 2017, 2019), and imaged on an Olympus X81 inverted microscope (20X magnification) with a motorized stage. For multiplexed imaging, antibodies against CD3 (1:100; ThermoScientific; RM-9107-50), CD8 (1:100; Invitrogen; 14-0808-80), CD4 (1:100; Invitrogen;14-9766-80), CD11b-AF647 (1:100; Abcam; ab204471), CD11c (1:100; Biolegend; 117301), CD45/B220-AF647 (1:100; Biolegend), and β-Catenin- AF555 were used.

For histological analysis, slides were processed and stained for hematoxylin and eosin and β-catenin using standard approaches. Blind scoring was conducted by a pathologist (Dr. Kay Washington) using brightfield microscopy and a standard grading scale for dysplasia.

Image quantification

For lineage tracing, the number of fully labelled crypts against total number of crypts was quantified.

For cell type quantification, manual delineation of the colonic epithelium was performed to generate masks for specific markers. ImageJ was used to automatically count cells with single marker expression, and marker/reporter co-expression. These numbers were then normalized to the area occupied by a nuclear mask to generally mark the amount of tissue imaged.

Quantitative multiplexed image analysis was performed as described previously by epithelium masking, single-cell segmentation, and calculating median intensity for each marker with respect to the whole cell, plasma membrane, cytoplasm, and nucleus (51,313,314).

Single-cell dissociation

Tissue used for other studies were enriched for epithelium by chelating in 2 mM EDTA/EGTA, 0.5mM DTT in 1X DPBS at 4 degrees Celsius on a rotating shaker for 1 hour 15 min followed by 2 min of shaking in 1X DPBS. Tissues were then gently passaged through a syringe and then dissociated into single cells with a cold-activated protease (1 mg/mL) and DNase I (2.5 mg/mL) mixture in 1x DPBS for 25 min on a rocker at 4

degrees Celsius. Multiple washes with 1X DPBS were then conducted, and cell viability was determined by counting Trypan Blue positive cells.

Organoid formation assays

Cell number was normalized and plated onto 24 wells plates in Matrigel overlaid with Intesticult (Fisher scientific, NC0879988). After one week, the number of organoids was counted using The GelCount™ system by Oxford Optronix. The number of organoids formed in each well was normalized to the number of single cells plated to determine organoid formation.

Antigen processing and presentation assay and activation of T cells

Organoids were formed and cultured for one week in Matrigel and Intesticult. Then, organoids were collected and reseeded without Matrigel in 100 mg/mL DQ-Ovalbumin (Thermo Fisher Scientific, D12053) in Intesticult for approximately 24 hours. After 24 hours, organoids were fixed, stained overnight with antibodies against GFP and Ia/Ie-AF647 (1:100; Biolegend, 10760), and analyzed using a BD LSRII 5-laser flow cytometer. Flow data were analyzed using Cytobank (315). To analyze activation of naïve T cells, crypts were plated on 24 or 6 well plates in Matrigel discs overlaid with Intesticult. Approximately, one week later, organoids were collected, dissociated into single cells and reseeded without Matrigel in 100 ug/mL of Ovalbumin peptide (Anaspec, OVA323-339) in Intesticult for approximately 24 hours. Following 24 hours, naïve OTII T cells were

added to the tumor cell/Ova peptide mixture for 3 days or 5 days. T cells were sorted and analyzed through flow cytometry and cell trace violet. See Biton *et al.* for more detail.

MARIS bulk sequencing of reporter expressing cells

After chelation but prior to single-cell dissociation, tissue was processed with a modified fixation/dissociation protocol (254). Briefly, tissue was fixed for 15 min (0.1% Saponin in 4% PFA, RNAse-inhibitor), washed (0.1% Saponin in 1X DPBS RNAse-inhibitor), and stained overnight with primary antibodies against GFP and EPCAM (1:100; Santa Cruz Biotech; Sc-53532) in wash buffer. The following day, samples were washed with 1X DPBS, followed by an 1-hour incubation with compatible secondary antibodies in wash buffer. Samples were subsequently fixed followed by mechanical disassociation into single cells before flow sorting using BD FACSAria III.

After sorting, total RNA was isolated from the flow sorted cells using the RecoverAll Total Nucleic Acid Isolation kit (Ambion), starting at the protease digestion stage of the manufacturer-recommended protocol similarly to Hrvatin *et al* (254). The initial protease digest was scaled to the number of the cells post-sorting. Complementary DNA (cDNA) was generated from 160 ng of total RNA with Poly A priming using Maxima H minus reverse transcriptase (ThermoFisher). The poly A capture primers used were the identical to unconjugated primers used for inDrop scRNA-seq in order to generate cDNA libraries comparable to the reference scRNA-seq datasets for downstream integrative analysis (316). RNA-seq libraries were prepared as in *Southard-Smith et al.* (317) and sequenced

on the NextSeq 500 (Illumina) as described below. To integrate with scRNA-seq datasets, the resulting bulk RNA-seq dataset was treated as a single cell datapoint, and normalized and processed accordingly (318).

Single-cell RNA-sequencing

Single cells were encapsulated and barcoded using the inDrop platform (1CellBio) with an in vitro transcription library preparation protocol (316). Briefly, the CEL-Seq work flow entailed (1) reverse transcription (RT), (2) ExoI digestion, (3) SPRI purification (SPRIP), (4) Second strand synthesis, (5) T7 in vitro transcription linear Amplification, (7) SPRIP, (8) RNA Fragmentation, (9) SPRIP, (10) primer ligation, (11) RT, (12) SPRIP, (13) library enrichment PCR, and (14) SPRIP (47). Each sample was estimated to contain approximately 3,000 encapsulated cells. Following library preparation, the samples were sequenced using Nextseq 500 (Illumina) using a PE 75 sequencing kit in a customized sequencing run. After sequencing, reads were filtered, sorted by their barcode of origin, and aligned to the reference transcriptome using the inDrops pipeline. Mapped reads were quantified into UMI-filtered counts per gene, and barcodes that corresponded to cells were retrieved based on previously established methods (316).

Single-cell data analysis

Epithelial and non-epithelial cells were analyzed separately. Thus, the datasets of each condition were normalized and subsequently integrated using the Harmony algorithm. We

visualized the single-cell transcriptomic landscape using Uniform Manifold Approximation and Projection (UMAP). Cell clusters were determined through unsupervised Leiden clustering through the Scanpy python toolkit. To further analyze epithelial cell populations, k-means clustering was utilized via Matlab to separate the data into cell identity categories: stem/ tumor stem cells, transitioning, secretory, absorptive. Secretory cells were further separated into goblet, tuft, and *Reg4*+ clusters. The ratio of Mist1 and Lrig1 tumor cells per cluster were determined through Matlab. The stem/TSCs data were used for CytoTRACE (https://cytotrace.stanford.edu/), differential gene expression (*Myc, Ctnnb1, Krt18*, and *Krt8)*, gene ontology, and metagene analyses. Pseudo-bulk analysis was done by averaging the single cell data per cluster (combining biological replicates) and normalizing it per gene across datasets used. Immune cell populations were further subclustered using the Leiden algorithm. Lrig1 and Mist1 tumors were analyzed separately to determine the proportional representation of each of the observed immune cell populations.

Statistics

Unpaired t-tests, One-sample t-tests, Mann-Whitney U-tests, and 1-way ANOVA tests were performed using Prism (Graphpad).

Declaration of approval for animal experiments

All animal experiments were performed under protocols approved by the Vanderbilt University Animal Care and Use Committee and in accordance with NIH guidelines.

Chapter VI

SUMMARY AND FUTURE DIRECTIONS

Summary

Throughout this thesis, we investigated tissue heterogeneity on the single cell level in normal and disease states of human and mouse intestine. To do so we improved upon our previously published Disaggregation for Intracellular Signaling in Single Epithelial Cells from Tissue (DISSECT) technique by verifying the signals seen in (FFPE) murine and human tissues (112). We then applied this technique tissue to explore the cellular heterogeneity within human colorectal cancer (CRC). Moreover, utilizing other single cell technologies like single-cell RNA-seq and multiplexed imaging we investigated the tumor make up of non-stem and stem cell driven colon tumors.

In Chapter III we explored the signaling pathway heterogeneity seen within the intestine through protein multiplexing via DISSECT-CyTOF. Throughout this study. We first verified that native signaling pathways are consistent across methodologies by comparing fresh DISSECT to FFPE-DISSECT. Interestingly, we found that cell type and villi-specific signals of the intestinal epithelial are consistent across platforms, but crypt-specific signals are not. This is largely due to fresh- DISSECT being optimized for mucosal

scraping neglecting the crypts whereas FFPE-DISSECT utilized tissue sections so the whole villi-crypt cross section can be analyzed.

FFPE is the preferred method for preserving tissues in the clinic therefore we analyzed signaling and cellular composition of clinically-annotated colonic tissue samples from the Western Division of the Cooperative Human Tissue Network (CHTN), situated at the Vanderbilt University Medical Center. We focused on analysis of epithelial and cancer cells in a variety of differentiation states. Interestingly, terminally differentiated cells and their respective signaling proteins were significantly decreased in CRC compared to normal suggesting that differentiation and associated signaling is reduced in CRC. Moreover, utilizing t-SNE analysis, we observed a lack of distant organization of the signaling and cell types within CRC compared to normal colon samples. Furthermore, this organization was not preserved from CRC sample to sample suggesting not only intratumoral heterogeneity, but intertumoral heterogeneity. Lastly, we observed that genetic properties, such as microsatellite instability and mutations, but not pathologic details, such as grade and stage of the tumor, correlate with single-cell signaling phenotypes in CRC suggesting a multi-factor approach could better predict prognosis and therapeutic response.

In Chapter IV, we expanded on the DISSECT methodology to cater towards cryopreserved tissues which preserves more sensitive antigen and nucleic acids that perish during formalin fixation, dehydration, and paraffinization. We showed that both epithelial and non-epithelial cells can be resolved and analyzed using Cryo-DISSECT

from human tissue. We also created a detailed protocol for FFPE-, cryo- and fresh-DISSECT.

Lastly, in Chapter V, we investigated the different tumor composition and stem capacity of non-stem and stem cell driven tumors. Specifically, tumor stem cells (TSCs) contribute to cancer mortality via therapeutic resistance, tumor recurrence, and metastatic mechanisms. However, the origins of the stem capacity to TSCs remains in question, but all TSCs descend from the original tumor cell-of-origin where the first oncogenic event occurred. Tumors arising from different cells-of-origin are histologically identical, but it is unknown whether TSCs that arose from different origins are molecularly and functionally distinct. Using mouse models driving identical *Apc* mutations from *Lrig1*-expressing and *Mist1*-expressing cells, we characterized TSCs of tumors driven from stem and non-stem cells-of-origin using single cell RNA sequencing (scRNA-seq), organoids, and multiplexed imaging. We revealed reduced stem capacity but increased class II antigen presentation ability for non-stem cell (Mist1) driven TSCs compared with stem cell (Lrig1) driven TSCs, which resulted in a favorable immune microenvironment skewed towards active cytotoxic response in Mist1-driven tumors. These results suggest that the cell-of-origin of tumorigenesis provides a specific context by which TSCs are generated, dictating their interactions with the tumor microenvironment.

Overall, this thesis represents a holistic view on how normal and diseased colon can be analyzed on the single cell level. In doing so, we now have a more thorough understanding of normal and cancerous tissue that can be utilized in better diagnosis and

treatment of colorectal cancer. Cancer therapy regimes have horrendous side effects. Moreover, currently a patient can endure up to 3 different therapy regimes before finding the right therapy so not only can the tumor progress during this time, the patient experiences unnecessary therapy side effects. Therefore, although more work needs to be done before extensive implementation, utilization of single cell technologies discussed throughout this thesis including scRNA-Seq and DISSECT-CyTOF, at the time of cancer diagnosis is imperative. It will obliterate the trial-and-error approach currently taken in the clinics providing a personalized treatment regime that will target the cancer sooner and prevent unnecessary side effects the patient experiences. This in turn increases the quality of life of the patient while decreasing the morality rate of colorectal cancer and the overall cost to the health care system.

Future directions

Defining stem capacity of tumor stem cells

My thesis work establishes that tumor stem cells maintain a signature of the tumor cell-of-origin. Briefly, stem cell-driven tumors give rise to tumor stem cells (TSCs) that have more stem capacity and a more immune suppressive microenvironment. In contrast, non-stem cell-driven tumors contain TSCs that have less stem capacity, a cellular make up skewed toward secretory lineages, and a more cytotoxic immune microenvironment. Tumor-initiating cells (TICs) are defined as tumor cells that possess stem capacity to initiate novel tumors. Future work would address whether the TSCs within Mist1 and Lrig1 tumors are equivalent to TICs and, if so, whether the resultant secondary tumors

resemble the tumor cell-of-origin. This question can be addressed through orthotopic injection of Mist1- and Lrig1-derived tumoroids into recipient mice followed by assessment of secondary tumor formation that has already been presented in this work. We hypothesize that there are intrinsic characteristics of the tumor cell-of-origin maintained in the TSCs, and resultant TICs, such that Mist1- and Lrig1-driven tumoroids would successfully drive tumorigenesis. We hypothesize that the secondary tumors resulting from tumoroid implantation would resemble the primary tumors. Specifically, tumors derived from Mist1 tumoroids would have less stem capacity, but more antigen presentation than tumors derived from Lrig1 tumoroids. This would contribute to a cytotoxic immune microenvironment in secondary Mist1-derived tumors as seen in the primary Mist1- derived tumors. The null hypothesis would state that, regardless of whether Lrig1 or Mist1 tumoroids were implanted, the resultant secondary tumors would share similar characteristics to on another. Although we see differentiation tumoroid formation from primary tumors, this may not translate into secondary tumors. For the dynamic colonic epithelium to function correctly, it relies on a plethora of extrinsic factors like the immune microenvironment, which is absent in tumoroids (319,320). If this is the case, we will explore these avenues.

My thesis addresses cellular plasticity prior to tumor initiation, but there is increasing interest in the field to understand tumor cellular plasticity. An important unaddressed question is whether non-TSCs can become surrogate TSCs to help maintain and re-

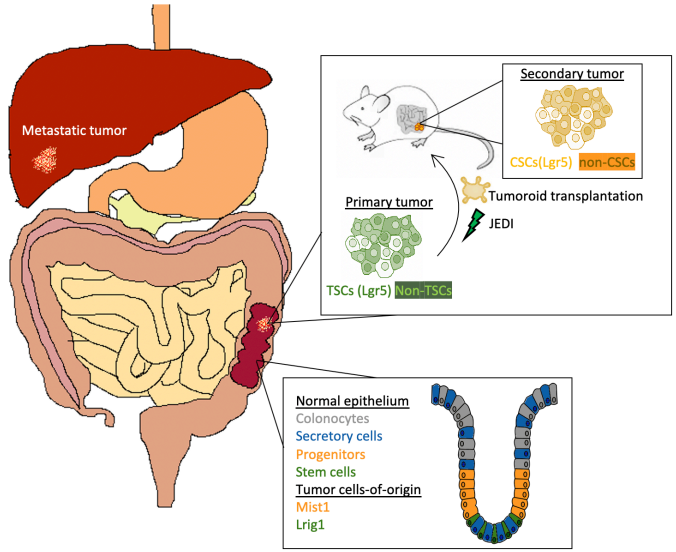

Fig 6.1. Primary, secondary, and metastatic tumors maintain a signature of the tumor cell-of-origin. Primary tumors are the original tumors initiated from Mist1 (non-stem) or Lrig1 (stem) expressing cells. These cells contain TSCs that maintain characteristics of the tumor cell-of-origin. Tumoroids can be established from primary tumors, genetically manipulated, and transplanted orthotopically into recipient mice to give rise to secondary tumors. Secondary tumors contain CSCs that we hypothesize maintain a signature of the tumor cell-of-origin. We anticipate that genetically manipulated tumoroids will result in metastatic tumors that also maintain a signature of the tumor cell-of-origin. Moreover, TSCs in primary tumors can be ablated through JEDI to probe plasticity. JEDI in addition to ICI can be used to probe primary tumor response to therapy.

establish tumors when the original TSCs are compromised. A tumor functions like a mini-organ and, therefore, ablation of TSCs can allow us to investigate tumor cell plasticity. We define TSCs as Lgr5 expressing cells within the tumors therefore can take advantage of just EGFP death inducing (JEDI) T cells to ablation TSCs.

The tumor models described in this work will be crossed with Lgr5-DTR-EGFP mice to enable ablation of EGFP-expressing TSCs upon adoptive transfer of just EGFP death inducing (JEDI) T cells (321). Due to the underlying plasticity in this system, we hypothesize that, despite the loss of TSCs, non-TSCs in both the Lrig1 and Mist1 models could regain stem capacity to re-establish and maintain tumors. These tumors would resemble the primary tumor because our overarching hypothesis states that tumor signatures are maintained throughout tumorigenesis. Alternatively, the tumors could be indistinguishable suggesting that the signature of the cell-of-origin may be lost as tumor cells differentiate from TSCs.

These experiments would also address whether cell-of-origin signatures are intrinsic or extrinsic. If the resulting tumor resemble original tumors, there are intrinsic properties to the maintenance of the cell of origin signature. If the resultant tumors are indistinguishable, then the immune microenvironment may play a role.

Defining antigen presentation abilities of tumor stem cells

My thesis work shows that Mist1 tumor derived TSCs have decreased stem capacity and increased propensity for secretory cell differentiation compared with Lrig1 tumor derived TSCs. Decreased stemness of TSCs correlates with increased MHCII-mediated antigen presentation, consistent with recent studies of different stem cell populations in the healthy intestine (35). What remains to be addressed is whether antigen presentation abilities of TSCs is an intrinsic quality related to TSC differentiation or an extrinsic quality, dependent on differential regulation of the immune microenvironment that subsequently influences stem cells. While the most direct explanation is intrinsic regulation driven by stem cell state as suggested by Biton et al., the intestine is a dynamic organ with constant perturbation from microbes and damage that stimulate the local immune microenvironment and its interaction with epithelial cells. To explore extrinsic vs. intrinsic regulation of TSC MHCII characteristics, Mist1 and Lrig1 tumoroids could be modulated by the addition of MHCII inhibitors and agonists or by immune cells isolated from their respective hosts and assayed for MHCII function. Furthermore, tumoroids could be transplanted into immunocompromised mice before assessing MHCII characteristics to determine the immune contribution to tumor formation and make. up. MHC class II knockout in Mist1 and Lrig1 tumor models could also be applied to determine the necessity of this machinery in tumor induction.

Tumor response to immunotherapy

A hallmark of successful immunotherapy is cytotoxic killing of tumor cells. Based on the robust immune environment observed in non-stem cell-driven tumors, we expect that the microenvironment will facilitate T cell-mediated killing. The JEDI system is engineered to enable CD8+ T cell-mediated killing of EGFP expressing cells. As explained previously, the tumor models described in this work will be crossed with Lgr5-DTR-EGFP mice to enable ablation of EGFP-expressing TSCs upon adoptive transfer of just EGFP death inducing (JEDI) T cells. Rather than assessing long term effects of TSC ablation, we would assess whether JEDI T cells can differentially ablate EGFP+ TSCs arising from stem or non-stem cells in the primary tumor. We hypothesize that there will be differential control of tumor growth and regression that is dependent on T cell killing of TSCs in the two tumor models. An alternative result may be that targeted T cell infiltration normalizes the immune microenvironment, in which case, we will then investigate the mechanisms that cause this effect.

Conversely, Lrig1-driven tumors express immunosuppressive markers *Pd1, Pdl1,* and *Ctla4*, that are targeted by checkpoint therapy. Immune checkpoint therapy sequesters these immunosuppressive molecules, re-stimulating a cytotoxic immune response, causing tumor regression (322). Therefore, we anticipate that Lrig1-dervied tumors would regress with immune checkpoint therapy. To test this, Lrig1-derived tumors would be treated with immune checkpoint therapy and assessed for growth and proliferation.

Defining characteristics of advanced lesions

Moreover, this work only addresses adenomas and not advanced lesions or metastasis. To address whether these processes are dictated by the tumor cell-of-origin, tumoroids could be generated form Mist1 and Lrig1 driven primary tumors as described in this work. CRISPR/Cas9 would be used on these tumoroids to further generate compound mutant tumoroids which could then be transplanted into mice. The tumors could be assessed in a similar manner as the primary tumors, through transcriptomic analysis and functional assays. Metastasis potential to the liver would be used as a hallmark of tumor aggressiveness given the propensity of colonic tumors to metastasize to that organ. We hypothesize that, due their more stem like and immune suppressive nature, stem cell-driven tumors metastasis far more rapidly compared to non-stem cell driven tumors. The alternative would be that there is no difference in metastatic rate or severity, meaning that metastasis is driven by factors agnostic to the original tumor cell-of-origin. These factors could include the number of antigens within the tumor, exhaustion of the immune microenvironment, or acquisition of mutations.

REFERECES

1. NIH National Cancer Institute. Cancer Facts & Figures 2020. CA Cancer J Clin [Internet]. 2020;1–76. Available from: https://www.cancer.org/cancer/bladder-cancer/detection-diagnosis-staging/survival-rates.html
2. Macrae FA, Bendell J. Clinical presentation, diagnosis, and staging of colorectal cancer. UpToDate ®. 2016;
3. Tabung FK, Brown LS, Fung TT. Dietary Patterns and Colorectal Cancer Risk: a Review of 17 Years of Evidence (2000–2016). Curr. Colorectal Cancer Rep. 2017.
4. Vogel JD, Eskicioglu C, Weiser MR, Feingold DL, Steele SR. The American society of colon and rectal surgeons clinical practice guidelines for the treatment of colon cancer. Dis Colon Rectum. 2017;
5. Davidson D, Coulombe Y, Martinez-Marignac VL, Amrein L, Grenier J, Hodkinson K, et al. Irinotecan and DNA-PKcs inhibitors synergize in killing of colon cancer cells. Invest New Drugs [Internet]. 2012;30:1248–56. Available from: http://link.springer.com/10.1007/s10637-010-9626-9
6. Longley DB, Harkin DP, Johnston PG. 5-Fluorouracil: Mechanisms of action and clinical strategies. Nat. Rev. Cancer. 2003.
7. PDQ Adult Treatment Editorial Board. Colon Cancer Treatment (PDQ®): Health Professional Version [Internet]. PDQ Cancer Inf. Summ. National Cancer Institute (US); 2002 [cited 2020 Jul 14]. Available from: http://www.ncbi.nlm.nih.gov/pubmed/26389297
8. Tabernero J. The role of VEGF and EGFR inhibition: Implications for combining Anti-VEGF and Anti-EGFR Agents. Mol. Cancer Res. 2007.
9. Chiang J-M. Role of K-ras mutations in colorectal carcinoma. Cancer Lett. 126:179–185.
10. De Roock W, Jonker DJ, Di Nicolantonio F, Sartore-Bianchi A, Tu D, Siena S, et al. Association of KRAS p.G13D mutation with outcome in patients with chemotherapy-refractory metastatic colorectal cancer treated with cetuximab. JAMA - J Am Med Assoc. 2010;
11. Custodio A, Feliu J. Prognostic and predictive biomarkers for epidermal growth factor receptor-targeted therapy in colorectal cancer: Beyond KRAS mutations. Crit. Rev. Oncol. Hematol. 2013.
12. Ribas A, Hersey P, Middleton MR, Gogas H, Flaherty KT, Sondak VK, et al. New challenges in endpoints for drug development in advanced melanoma. Clin. Cancer Res. 2012.
13. Ganesh K, Stadler ZK, Cercek A, Mendelsohn RB, Shia J, Segal NH, et al. Immunotherapy in colorectal cancer: rationale, challenges and potential. Nat. Rev. Gastroenterol. Hepatol. 2019.

14. Llosa NJ, Cruise M, Tam A, Wicks EC, Hechenbleikner EM, Taube JM, et al. The vigorous immune microenvironment of microsatellite instable colon cancer is balanced by multiple counter-inhibitory checkpoints. Cancer Discov. 2015;
15. Curtin K, Slattery ML, Samowitz WS. {CpG} Island Methylation in Colorectal Cancer: Past, Present and Future. Patholog Res Int. 2011;2011:902674.
16. Samowitz WS. The {CpG} island methylator phenotype in colorectal cancer. J Mol diagnostics {JMD}. 9:281–3.
17. Flavahan WA, Gaskell E, Bernstein BE. Epigenetic plasticity and the hallmarks of cancer [Internet]. Science (80-.). American Association for the Advancement of Science; 2017 [cited 2020 Jul 14]. Available from: /pmc/articles/PMC5940341/?report=abstract
18. Tong GJ, Zhang GY, Liu J, Zheng ZZ, Chen Y, Niu PP, et al. Comparison of the eighth version of the American joint committee on cancer manual to the seventh version for colorectal cancer: A retrospective review of our data. World J Clin Oncol. 2018;
19. Kikuchi T, Mimura K, Okayama H, Nakayama Y, Saito K, Yamada L, et al. A subset of patients with MSS/MSI-low-colorectal cancer showed increased CD8(+) TILs together with up-regulated IFN-γ. Oncol Lett. 2019;
20. Fearon EF, Vogelstein B. for Colorectal Tumorigenesis. Cell. 1989;61:759–67.
21. Smedt DL, Lemahieu J, Palmans S, Govaere O, Tousseyn T, Cutsem VE, et al. Microsatellite instable vs stable colon carcinomas: analysis of tumour heterogeneity, inflammation and angiogenesis. Br J Cancer [Internet]. Nature Publishing Group; 2015;113:500–9. Available from: http://www.nature.com/doifinder/10.1038/bjc.2015.213
22. Galon J, Mlecnik B, Bindea G, Angell HK, Berger A, Lagorce C, et al. Towards the introduction of the {'Immunoscore'} in the classification of malignant tumours. 2014;232:199–209.
23. Azzouz LL, Sharma S. Physiology, Large Intestine. StatPearls. 2018.
24. Lodish HF, Berk A, Zipursky SL, Matsudaira P, Baltimore D, James D. Molecular Cell Biology, 7th edition. Book. 2013.
25. van der Wath RC, Gardiner BS, Burgess AW, Smith DW. Cell Organisation in the Colonic Crypt: A Theoretical Comparison of the Pedigree and Niche Concepts. PLoS One. 2013;
26. Dalal J, Radhi M. Intestinal Stem Cells: Common Signal Pathways, Human Disease Correlation, and Implications for Therapies. ISRN Stem Cells [Internet]. 2012;2013:1–6. Available from: https://www.hindawi.com/archive/2013/372068/
27. Barker N, van de Wetering M, Clevers H. The intestinal stem cell. 2008;22:1856–64.
28. Marshman E, Booth C, Potten CS. The intestinal epithelial stem cell. 2002;24:91–8.
29. Kosinski C, Li VSW, Chan ASY, Zhang J, Ho C, Wai YT, et al. Gene expression patterns

of human colon tops and basal crypts and BMP antagonists as intestinal stem cell niche factors. Proc Natl Acad Sci U S A. 2007;

30. Vinson KE, George DC, Fender AW, Bertrand FE, Sigounas G. The Notch pathway in colorectal cancer. Int. J. Cancer. 2016.

31. Du H, Nie Q, Holmes WR. The Interplay between Wnt Mediated Expansion and Negative Regulation of Growth Promotes Robust Intestinal Crypt Structure and Homeostasis. PLoS Comput Biol. 2015;

32. Campos FGG, Figueiredo MN, Martinez CA. Colorectal cancer risk in hamartomatous polyposis syndromes. 2015;7:25–32.

33. Kozar S, Morrissey E, Nicholson AMM, van der Heijden M, Zecchini HII, Kemp R, et al. Continuous clonal labeling reveals small numbers of functional stem cells in intestinal crypts and adenomas. Cell Stem Cell [Internet]. 2013;13:626–33. Available from: http://linkinghub.elsevier.com/retrieve/pii/S1934590913003640

34. Cheng H, Leblond CP. Origin, differentiation and renewal of the four main epithelial cell types in the mouse small intestine. V. Unitarian Theory of the origin of the four epithelial cell types. Am J Anat. 1974;141:537–61.

35. Biton M, Haber AL, Rogel N, Burgin G, Beyaz S, Schnell A, et al. T Helper Cell Cytokines Modulate Intestinal Stem Cell Renewal and Differentiation. Cell. 2018;175:1307--1320.e22.

36. Takeda N, Jain R, MR L, Wang Q, Lu MM. Interconversion between intestinal stem cell populations in distinct niches. 2011;

37. Montgomery RK, Breault DT. Small intestinal stem cell markers. 2008;213:52–8.

38. Powell AE, Wang Y, Li Y, Poulin EJ, Means AL. The {pan-ErbB} negative regulator Lrig1 is an intestinal stem cell marker that functions as a tumor suppressor. 2012;

39. Poulin EJ, Powell AE, Wang Y, Li Y, Franklin JL, Coffey RJ. Using a new Lrig1 reporter mouse to assess differences between two Lrig1 antibodies in the intestine. Stem Cell Res [Internet]. Elsevier B.V.; 2014;13:422–30. Available from: http://dx.doi.org/10.1016/j.scr.2014.09.002

40. de Santa Barbara P, van den Brink GR, Roberts DJ, de Barbara SP, van den Brink GR, Roberts DJ. Development and differentiation of the intestinal epithelium. Cell Mol Life Sci [Internet]. 2003;60:1322–32. Available from: http://link.springer.com/10.1007/s00018-003-2289-3

41. Worthington JJ, Reimann F, Gribble FM. Enteroendocrine cells-sensory sentinels of the intestinal environment and orchestrators of mucosal immunity. Mucosal Immunol. 2017;11:3–20.

42. Altmann GG. Morphological observations on mucus-secreting nongoblet cells in the deep

crypts of the rat ascending colon. 1983;167:95–117.

43. Sasaki N, Sachs N, Wiebrands K, Ellenbroek SIJ, Fumagalli A, Lyubimova A, et al. Reg4+ deep crypt secretory cells function as epithelial niche for Lgr5+ stem cells in colon. 2016;113:E5399–407.

44. Rothenberg ME, Nusse Y, Kalisky T, Lee JJ, Dalerba P, Scheeren F, et al. Identification of a cKit+colonic crypt base secretory cell that supports Lgr5+stem cells in mice. Gastroenterology [Internet]. Elsevier Inc.; 2012;142:1195-1205.e6. Available from: http://dx.doi.org/10.1053/j.gastro.2012.02.006

45. Barker N, van Oudenaarden A, Clevers H. Identifying the stem cell of the intestinal crypt: strategies and pitfalls. Cell Stem Cell [Internet]. Elsevier Inc.; 2012;11:452–60. Available from: http://dx.doi.org/10.1016/j.stem.2012.09.009

46. Gerbe F, Brulin B, Makrini L, Legraverend C, Jay P. DCAMKL-1 Expression Identifies Tuft Cells Rather Than Stem Cells in the Adult Mouse Intestinal Epithelium. Gastroenterology. 2009.

47. Herring CA, Banerjee A, McKinley ET, Simmons AJ, Ping J, Roland JT, et al. Unsupervised Trajectory Analysis of Single-Cell RNA-Seq and Imaging Data Reveals Alternative Tuft Cell Origins in the Gut. Cell Syst [Internet]. 2018 [cited 2018 Mar 29];6:37-51.e9. Available from: http://www.ncbi.nlm.nih.gov/pubmed/29153838

48. Gerbe F, Sidot E, Smyth DJ, Ohmoto M, Matsumoto I, Dardalhon V, et al. Intestinal epithelial tuft cells initiate type 2 mucosal immunity to helminth parasites. 2016;529:226–30.

49. Howitt, M.R., Lavoie, S., Michaud, M., Blum, A.M., Tran, S.V., Weinstock, J.V., Gallini, C.A., Redding, K., Margolskee, R.F., Osborne, L.C. and Artis D, Howitt MR, Lavoie S, Michaud M, Blum AM, Tran S V, et al. Tuft cells, taste-chemosensory cells, orchestrate parasite type 2 immunity in the gut. Science (80-) [Internet]. 2016;351:1329–33. Available from: http://science.sciencemag.org/content/early/2016/02/03/science.aaf1648.full

50. von Moltke J, Ji M, Liang H-E, Locksley RM. Tuft-cell-derived {IL-25} regulates an intestinal {ILC2-epithelial} response circuit. 2015;529:221–5.

51. McKinley ET, Sui Y, Al-Kofahi Y, Millis BA, Tyska MJ, Roland JT, et al. Optimized multiplex immunofluorescence single-cell analysis reveals tuft cell heterogeneity. JCI insight [Internet]. NLM (Medline); 2017 [cited 2020 Jul 18];2. Available from: https://pubmed.ncbi.nlm.nih.gov/28570279/

52. Bjerknes M, Cheng H. Intestinal Epithelial Stem Cells and Progenitors. Methods Enzymol. 2006;419:337–83.

53. Ohnishi Y, Huber W, Tsumura A, Kang M, Xenopoulos P, Kurimoto K, et al. Cell-to-cell expression variability followed by signal reinforcement progressively segregates early

mouse lineages. Nat Cell Biol. 2013;16:27–37.

54. Tetteh PW, Basak O, Farin HF, Wiebrands K, Kretzschmar K, Begthel H, et al. Replacement of Lost {Lgr5-Positive} Stem Cells through Plasticity of Their {Enterocyte-Lineage} Daughters. Cell Stem Cell. 2016;18:203–13.

55. van Es JH, Sato T, van de Wetering M, Lyubimova A, Nee A, Gregorieff A, et al. Dll1+ secretory progenitor cells revert to stem cells upon crypt damage. Nat Cell Biol. 2012;14:1099.

56. Chandrakesan P, May R, Qu D, Weygant N, Taylor VE, Li JD, et al. Dclk1+ small intestinal epithelial tuft cells display the hallmarks of quiescence and self-renewal. Oncotarget. 2015;6:30876–86.

57. Westphalen BC, Asfaha S, Hayakawa Y, Takemoto Y, Lukin DJ, Nuber AH, et al. Long-lived intestinal tuft cells serve as colon cancer–initiating cells. J Clin Invest [Internet]. American Society for Clinical Investigation; 2014 [cited 2018 Feb 21];124:1283–95. Available from: https://www.jci.org/articles/view/73434

58. Jones JC, Brindley CD, Elder NH, Myers MG, Rajala MW, Dekaney CM, et al. Cellular Plasticity of Defa4Cre-Expressing Paneth Cells in Response to Notch Activation and Intestinal Injury. Cell Mol Gastroenterol Hepatol. 2018;7:533–54.

59. Ishibashi F, Shimizu H, Nakata T, Fujii S, Suzuki K, Kawamoto A, et al. Contribution of {ATOH1+} Cells to the Homeostasis, Repair, and Tumorigenesis of the Colonic Epithelium. Stem Cell Reports. 2018;10:27–42.

60. Yu S, Tong K, Zhao Y, Balasubramanian I, Yap GS, Ferraris RP, et al. Paneth Cell Multipotency Induced by Notch Activation following Injury. Cell Stem Cell. 2018;23:46--59.e5.

61. Yan KS, Chia LA, Li X, Ootani A, Su J, Lee JY, et al. The intestinal stem cell markers Bmi1 and Lgr5 identify two functionally distinct populations. Proc Natl Acad Sci U S A. 2012;

62. Yuan S, Norgard RJ, Stanger BZ. Cellular plasticity in cancer. Cancer Discov. 2019.

63. Goldenring JR, Nam KT, Wang TC, Mills JC, Wright NA. Spasmolytic Polypeptide-Expressing Metaplasia and Intestinal Metaplasia: Time for Reevaluation of Metaplasias and the Origins of Gastric Cancer. Gastroenterology [Internet]. 2010 [cited 2018 Mar 12];138:2207-2210.e1. Available from: http://linkinghub.elsevier.com/retrieve/pii/S0016508510005949

64. Mills JC, Goldenring JR. Metaplasia in the Stomach Arises From Gastric Chief Cells. CMGH. 2017.

65. Mills JC, Taghert PH. Scaling factors: Transcription factors regulating subcellular domains. BioEssays. 2012;

66. Shimokawa M, Ohta Y, Nishikori S, Matano M, Takano A, Fujii M, et al. Visualization and targeting of {LGR5+} human colon cancer stem cells. Nature. 2017;545:187–92.

67. Schwitalla S, Fingerle A a., Cammareri P, Nebelsiek T, Göktuna SI, Ziegler PK, et al. Intestinal tumorigenesis initiated by dedifferentiation and acquisition of stem-cell-like properties. Cell. 2013;152:25–38.

68. Gross S, Balderes D, Liu J, Asfaha S, Gu G, Wang TC, et al. Nkx2.2 is expressed in a subset of enteroendocrine cells with expanded lineage potential. Am J Physiol - Gastrointest Liver Physiol. 2015;

69. Nakanishi Y, Seno H, Fukuoka A, Ueo T, Yamaga Y, Maruno T, et al. Dclk1 distinguishes between tumor and normal stem cells in the intestine. Nat Genet [Internet]. Nature Publishing Group; 2013 [cited 2015 Nov 20];45:98–103. Available from: http://dx.doi.org/10.1038/ng.2481

70. Murata K, Jadhav U, Madha S, van Es J, Dean J, Cavazza A, et al. Ascl2-Dependent Cell Dedifferentiation Drives Regeneration of Ablated Intestinal Stem Cells. Cell Stem Cell. 2020;

71. Fearon ER, Hamilton SR, Vogelstein B. Clonal analysis of human colorectal tumors. 1987;238:193–7.

72. Fearon ER. Molecular Genetics of Colorectal Cancer. Annu Rev Pathol Mech Dis [Internet]. Annual Reviews ; 2011 [cited 2018 Feb 28];6:479–507. Available from: http://www.annualreviews.org/doi/10.1146/annurev-pathol-011110-130235

73. Barker N, Ridgway RA, Van Es JH, van de Wetering M, Begthel H, Van Den Born M, et al. Crypt stem cells as the cells-of-origin of intestinal cancer. Nature. 2009;457:608–11.

74. Metcalfe C, Kljavin NM, Ybarra R, de Sauvage FJ. Lgr5+ stem cells are indispensable for radiation-induced intestinal regeneration. Cell Stem Cell. 2014;14:149–59.

75. Sangiorgi E, Capecchi MR. Bmi1 is expressed in vivo in intestinal stem cells. Nat Genet. 2008;40:915–20.

76. Giroux V, Stephan J, Chatterji P, Rhoades B, Wileyto EP, Klein-Szanto AJ, et al. Mouse Intestinal Krt15+ Crypt Cells Are Radio-Resistant and Tumor Initiating. Stem cell reports. 2018;

77. Buczacki SJA, Zecchini H, Nicholson AM, Russell R, Vermeulen L, Kemp R, et al. Intestinal label-retaining cells are secretory precursors expressing Lgr5. Nature. 2013;495:nature11965.

78. Vermeulen L, Snippert HJ. Stem cell dynamics in homeostasis and cancer of the intestine. Nat Rev Cancer. 2014;14:468–80.

79. Vermeulen L, Morrissey E, Heijden M van der, Nicholson AM, Sottoriva A, Buczacki S, et al. Defining Stem Cell Dynamics in Models of Intestinal Tumor Initiation. Science (80-).

2013;342:995–8.

80. Anderson EC, Hessman C, Levin TG, Monroe MM, Wong MH. The role of colorectal cancer stem cells in metastatic disease and therapeutic response. Cancers (Basel). 2011;3:319–39.

81. Huang J, Kalderon D. Coupling of Hedgehog and Hippo pathways promotes stem cell maintenance by stimulating proliferation. 2014;205:325–38.

82. Singh A, Settleman J. {EMT,} cancer stem cells and drug resistance: an emerging axis of evil in the war on cancer. Oncogene. 2010;29:4741–51.

83. Chen J, Li Y, Yu T-SS, M MR, Burns DK, Kernie SG, et al. A restricted cell population propagates glioblastoma growth after chemotherapy. Nature. 2012;488:522–6.

84. Gao M-QQ, Choi Y-PP, Kang S, Youn JH, Cho N-HH. CD24+ cells from hierarchically organized ovarian cancer are enriched in cancer stem cells. Oncogene. 2010;29:2672–80.

85. Dembinski JL, Krauss S. Characterization and functional analysis of a slow cycling stem cell-like subpopulation in pancreas adenocarcinoma. Clin Exp Metastasis. 2009;26:611–23.

86. Malta TM, Sokolov A, Gentles AJ, Burzykowski T, Poisson L, Weinstein JN, et al. Machine Learning Identifies Stemness Features Associated with Oncogenic Dedifferentiation. Cell. 2018;173:338--354.e15.

87. Janeway C. immunobiology, 5th ed. Elsevier. 2012.

88. Bruno A, Mortara L, Baci D, Noonan DM, Albini A. Myeloid Derived Suppressor Cells Interactions With Natural Killer Cells and Pro-angiogenic Activities: Roles in Tumor Progression. Front Immunol. 2019;10:771.

89. Trikha P, Carson WE. Signaling pathways involved in MDSC regulation. Biochim Biophys Acta - Rev Cancer. 2014;1846:55–65.

90. Nadafi R, Gago de Graça C, Keuning ED, Koning JJ, de Kivit S, Konijn T, et al. Lymph Node Stromal Cells Generate Antigen-Specific Regulatory T Cells and Control Autoreactive T and B Cell Responses. Cell Rep. 2020;

91. Wei SC, Levine JH, Cogdill AP, Zhao Y, Anang N-A, Andrews MC, et al. Distinct Cellular Mechanisms Underlie {Anti-CTLA-4} and {Anti-PD-1} Checkpoint Blockade. Cell. 2017;170:1120-1133.e17.

92. Wherry EJ, Kurachi M. Molecular and cellular insights into T cell exhaustion. Nat. Rev. Immunol. 2015.

93. Leone RD, Powell JD. Metabolism of immune cells in cancer. Nat. Rev. Cancer. 2020.

94. Crespo J, Sun H, Welling TH, Tian Z, Zou W. T cell anergy, exhaustion, senescence, and stemness in the tumor microenvironment. Curr. Opin. Immunol. 2013.

95. Schwartz RH. T C ELL A NERGY. Annu Rev Immunol. 2003;21:305–34.

96. Schietinger A, Greenberg PD. Tolerance and exhaustion: Defining mechanisms of T cell dysfunction. Trends Immunol. 2014.

97. Galon J, Costes A, Fatima S-C, Kirilovsky A, Mlecnik B, Christine L-P, et al. Type, Density, and Location of Immune Cells Within Human Colorectal Tumors Predict Clinical Outcome. Science (80-). 2006;313:1960–4.

98. Mlecnik B, Tosolini M, Kirilovsky A, Berger A, Bindea G, Meatchi T, et al. Histopathologic-based prognostic factors of colorectal cancers are associated with the state of the local immune reaction. J Clin Oncol. 2011;29:610–8.

99. Galon J, Bruni D. Approaches to treat immune hot, altered and cold tumours with combination immunotherapies. Nat. Rev. Drug Discov. 2019.

100. Camus M, Tosolini M, Mlecnik B, Pages F, Kirilovsky A, Berger A, et al. Coordination of intratumoral immune reaction and human colorectal cancer recurrence. Cancer Res. 2009;

101. Hegde PS, Karanikas V, Evers S. The where, the when, and the how of immune monitoring for cancer immunotherapies in the era of checkpoint inhibition. Clin Cancer Res. 2016;

102. Leko V, Rosenberg SA. Identifying and Targeting Human Tumor Antigens for T Cell-Based Immunotherapy of Solid Tumors. Cancer Cell [Internet]. Elsevier BV; 2020 [cited 2020 Sep 2];0. Available from: http://www.cell.com.proxy.library.vanderbilt.edu/article/S1535610820303743/fulltext

103. Hanahan D, Weinberg RA. Hallmarks of cancer: the next generation. Cell [Internet]. Elsevier Inc.; 2011;144:646–74. Available from: http://dx.doi.org/10.1016/j.cell.2011.02.013

104. Thibodeau J, Bourgeois-Daigneault M-C, Lapointe R. Targeting the MHC Class II antigen presentation pathway in cancer immunotherapy. Oncoimmunology. 2012;1:908–16.

105. Leinwand J, Miller G. Regulation and modulation of antitumor immunity in pancreatic cancer. Nat. Immunol. 2020.

106. Thibodeau J, Bourgeois-Daigneault MC, Lapointe R. Targeting the MHC Class II antigen presentation pathway in cancer immunotherapy. Oncoimmunology. 2012;

107. Grun D, Lyubimova A, Kester L, Wiebrands K, Basak O, Sasaki N, et al. Single-cell messenger {RNA} sequencing reveals rare intestinal cell types. Nature. 2015;525:251–5.

108. Jaitin DA, Kenigsberg E, Keren-Shaul H, Elefant N, Paul F, Zaretsky I, et al. Massively parallel single-cell RNA-seq for marker-free decomposition of tissues into cell types. Science (80-). 2014;

109. Klein AM, Mazutis L, Akartuna I, Tallapragada N, Veres A, Li V, et al. Droplet barcoding for single-cell transcriptomics applied to embryonic stem cells. Cell [Internet]. Cell Press; 2015 [cited 2020 Jul 18];161:1187–201. Available from: https://pubmed.ncbi.nlm.nih.gov/26000487/

110. Werner J. Introduction to flow cytometry. Introd. to Flow Cytom. 2019.

111. Bendall SC, Simonds EF, Qiu P, Amir ED, Krutzik PO, Finck R, et al. Single-Cell Mass Cytometry of Differential. Science (80-). 2011;332:687–95.

112. Simmons AJ, Banerjee A, McKinley ET, Scurrah CR, Herring CA, Gewin LS, et al. Cytometry-based single-cell analysis of intact epithelial signaling reveals MAPK activation divergent from TNF-α-induced apoptosis in vivo. Mol Syst Biol. 2015;11.

113. Scurrah CR, Simmons AJ, Lau KS. Cancer Immunosurveillance, Methods and Protocols. Methods Mol Biol. 2018;1884:215–29.

114. Simmons AJJ, Scurrah CRR, ET M, Herring CAA, Irish JMM, Washington MKK, et al. Impaired coordination between signaling pathways is revealed in human colorectal cancer using single-cell mass cytometry of archival tissue blocks. Sci Signal. 2016;9:rs11–rs11.

115. Gerdes MJ, Sevinsky CJ, Sood A, Adak S, Bello MO, Bordwell A, et al. Highly multiplexed single-cell analysis of formalin-fixed, paraffin-embedded cancer tissue. Proc Natl Acad Sci {USA}. 2013;110:11982–7.

116. Van Der Maaten LJP, Hinton GE. Visualizing high-dimensional data using t-sne. J Mach Learn Res [Internet]. 2008;9:2579–605. Available from: https://lvdmaaten.github.io/publications/papers/JMLR_2008.pdf%0Ahttp://www.ncbi.nlm.nih.gov/entrez/query.fcgi?db=pubmed&cmd=Retrieve&dopt=AbstractPlus&list_uids=7911431479148734548related:VOiAgwMNy20J

117. Becht E, McInnes L, Healy J, Dutertre CA, Kwok IWH, Ng LG, et al. Dimensionality reduction for visualizing single-cell data using UMAP. Nat Biotechnol. 2019;

118. Qiu P, Simonds EF, Bendall SC, Gibbs KD, Bruggner R V., Linderman MD, et al. Extracting a cellular hierarchy from high-dimensional cytometry data with SPADE. Nat Biotechnol. 2011;

119. Lancaster MA, Knoblich JA. Organogenesisin a dish: Modeling development and disease using organoid technologies. Science (80-.). 2014.

120. Takahashi K, Yamanaka S. Induction of pluripotent stem cells from mouse embryonic and adult fibroblast cultures by defined factors. 2006;126:663–76.

121. Sato T, Vries RG, Snippert HJ, van de Wetering M, Barker N, Stange DE, et al. Single Lgr5 stem cells build crypt-villus structures in vitro without a mesenchymal niche. Nature [Internet]. Macmillan Publishers Limited. All rights reserved; 2009 [cited 2014 Jul 10];459:262–5. Available from: http://dx.doi.org/10.1038/nature07935

122. Stelzner M, Helmrath M, Dunn JCY, Henning SJ, Houchen CW, Kuo C, et al. A nomenclature for intestinal in vitro cultures. Am J Physiol - Gastrointest Liver Physiol. 2012;

123. Behjati S, Huch M, Van Boxtel R, Karthaus W, Wedge DC, Tamuri AU, et al. Genome sequencing of normal cells reveals developmental lineages and mutational processes. Nature. 2014;

124. Sato T, Clevers H. Growing self-organizing mini-guts from a single intestinal stem cell: Mechanism and applications. Science (80-.). 2013.

125. Zachos NC, Kovbasnjuk O, Foulke-Abel J, In J, Blutt SE, De Jonge HR, et al. Human enteroids/colonoids and intestinal organoids functionally recapitulate normal intestinal physiology and pathophysiology. J. Biol. Chem. 2016.

126. Drost J, Clevers H. Translational applications of adult stem cell-derived organoids. Dev. 2017;

127. Foulke-Abel J, In J, Kovbasnjuk O, Zachos NC, Ettayebi K, Blutt SE, et al. Human enteroids as an ex-vivo model of host–pathogen interactions in the gastrointestinal tract. Exp Biol Med. 2014;

128. Kovbasnjuk O, Zachos NC, In J, Foulke-Abel J, Ettayebi K, Hyser JM, et al. Human enteroids: Preclinical models of non-inflammatory diarrhea. Stem Cell Res. Ther. 2013.

129. In JG, Foulke-Abel J, Estes MK, Zachos NC, Kovbasnjuk O, Donowitz M. Human mini-guts: New insights into intestinal physiology and host-pathogen interactions. Nat. Rev. Gastroenterol. Hepatol. 2016.

130. Gracz AD, Williamson IA, Roche KC, Johnston MJ, Wang F, Wang Y, et al. A high-throughput platform for stem cell niche co-cultures and downstream gene expression analysis. Nat Cell Biol. 2015;17:340–9.

131. Crespo M, Vilar E, Tsai S-Y, Chang K, Amin S, Srinivasan T, et al. Colonic organoids derived from human induced pluripotent stem cells for modeling colorectal cancer and drug testing. Nat Med. 2017;23:878–84.

132. Pauli C, Hopkins BD, Prandi D, Shaw R, Fedrizzi T, Sboner A, et al. Personalized in vitro and in vivo cancer models to guide precision medicine. Cancer Discov. 2017;

133. Drost J, Van Boxtel R, Blokzijl F, Mizutani T, Sasaki N, Sasselli V, et al. Use of CRISPR-modified human stem cell organoids to study the origin of mutational signatures in cancer. Science (80-). 2017;

134. Drost J, Van Jaarsveld RH, Ponsioen B, Zimberlin C, Van Boxtel R, Buijs A, et al. Sequential cancer mutations in cultured human intestinal stem cells. Nature. 2015;

135. Matano M, Date S, Shimokawa M, Takano A, Fujii M, Ohta Y, et al. Modeling colorectal cancer using CRISPR-Cas9-mediated engineering of human intestinal organoids. Nat

Med [Internet]. Nature Publishing Group; 2015;21:256–62. Available from: http://dx.doi.org/10.1038/nm.3802

136. Slattery ML, Pellatt DF, Mullany LE, Wolff RK. Differential Gene Expression in Colon Tissue Associated With Diet, Lifestyle, and Related Oxidative Stress. 2015;10:e0134406.

137. Lyons J, Herring CA, Banerjee A, Simmons AJ, Lau KS. Multiscale analysis of the murine intestine for modeling human diseases. Integr Biol [Internet]. Royal Society of Chemistry; 2015;7:740–757. Available from: http://xlink.rsc.org/?DOI=C5IB00030K

138. Keller DS, Windsor A, Cohen R, Chand M. Colorectal cancer in inflammatory bowel disease: review of the evidence. Tech. Coloproctol. 2019.

139. Kontoyiannis D, Pasparakis M, Pizarro TT, Cominelli F, Kollias G. Impaired on/off regulation of TNF biosynthesis in mice lacking TNF AU-rich elements: implications for joint and gut-associated immunopathologies. Immunity. 1999;10:387–98.

140. Parang B, Barrett CW, Williams CS. AOM/DSS Model of Colitis-Associated Cancer. Methods Mol Biol. 2016;

141. Chassaing B, Aitken JD, Malleshappa M, Vijay-Kumar M. Dextran sulfate sodium (DSS)-induced colitis in mice. Curr Protoc Immunol. 2014;

142. Laroui H, Ingersoll SA, Liu HC, Baker MT, Ayyadurai S, Charania MA, et al. Dextran sodium sulfate (dss) induces colitis in mice by forming nano-lipocomplexes with medium-chain-length fatty acids in the colon. PLoS One. 2012;

143. Whittem CG, Williams AD, Williams CS. Murine Colitis modeling using Dextran Sulfate Sodium (DSS). J Vis Exp. 2010;

144. Biton IE, Stettner N, Brener O, Erez A, Harmelin A, Garbow JR. Assessing Mucosal Inflammation in a DSS-Induced Colitis Mouse Model by MR Colonography. Tomogr (Ann Arbor, Mich). 2018;

145. Howard AM, Lafever KS, Fenix AM, Scurrah CR, Lau KS, Burnette DT, et al. DSS-induced damage to basement membranes is repaired by matrix replacement and crosslinking. J Cell Sci. 2019;

146. Vogt W. Gestaltungsanalyse am Amphibienkeim mit Örtlicher Vitalfärbung - II. Teil. Gastrulation und Mesodermbildung bei Urodelen und Anuren. Wilhelm Roux Arch Entwickl Mech Org. 1929;

147. Schepers AG, Snippert HJ, Stange DE, van den Born M, van Es JH, van de Wetering M, et al. Lineage Tracing Reveals Lgr5{<}sup{>}+{<}/sup{>} Stem Cell Activity in Mouse Intestinal Adenomas. Science (80-). 2012;337:730–5.

148. Pin CL, Bonvissuto AC, Konieczny SF. Mist1 expression is a common link among serous exocrine cells exhibiting regulated exocytosis. 2000;259:157–67.

149. Krapp A, Knöfler M, Ledermann B, Bürki K, Berney C, Zoerkler N, et al. The bHLH protein

PTF1-p48 is essential for the formation of the exocrine and the correct spatial organization of the endocrine pancreas. Genes Dev. 1998;

150. Pin CL, Rukstalis MJ, Johnson C, Konieczny SF. The {bHLH} transcription factor Mist1 is required to maintain exocrine pancreas cell organization and acinar cell identity. 2001;155:519–30.

151. Hayakawa Y, Tsuboi M, Asfaha S, Kinoshita H, Niikura R, Konishi M, et al. BHLHA15-positive Secretory Precursor Cells Can Give Rise to Tumors in Intestine and Colon in Mice. Gastroenterology. 2018;

152. Suzuki Y, Sato N, Tohyama M, Wanaka A, Takagi T. {cDNA} Cloning of a novel membrane glycoprotein that is expressed specifically in glial cells in the mouse brain {LIG-1,} a protein with leucine-rich repeats and immunoglobulin-like domains. 1996;271:22522–7.

153. Laederich MB, Funes-Duran M, Yen L, Ingalla E, Wu X, Carraway KL, et al. The leucine-rich repeat protein LRIG1 is a negative regulator of ErbB family receptor tyrosine kinases. J Biol Chem [Internet]. 2004 [cited 2016 Jan 28];279:47050–6. Available from: http://www.jbc.org/content/279/45/47050.long

154. Jensen KB, Collins CA, Nascimento E, Tan DW, Frye M, Itami S, et al. Lrig1 Expression Defines a Distinct Multipotent Stem Cell Population in Mammalian Epidermis. Cell Stem Cell. 2009;

155. Jensen KB, Watt FM. Single-cell expression profiling of human epidermal stem and transit-amplifying cells: Lrig1 is a regular of stem cell quiescence. Proc Natl Acad Sci U S A. 2006;

156. Wang Y, Poulin EJ, Coffey RJ. {LRIG1} is a triple threat: {ERBB} negative regulator, intestinal stem cell marker and tumour suppressor. 2013;108:1765–70.

157. Byrd KM, Piehl NC, Patel JH, Huh WJ, Sequeira I, Lough KJ, et al. Heterogeneity within Stratified Epithelial Stem Cell Populations Maintains the Oral Mucosa in Response to Physiological Stress. Cell Stem Cell. 2019;

158. Cleary AS, Leonard TL, Gestl SA, Gunther EJ. Tumour cell heterogeneity maintained by cooperating subclones in Wnt-driven mammary cancers. Nature. Nature Publishing Group; 2014;508:113–7.

159. Marusyk A, Tabassum DP, Altrock PM, Almendro V, Michor F, Polyak K. Non-cell-autonomous driving of tumour growth supports sub-clonal heterogeneity. Nature. Nature Publishing Group; 2014;6:54–8.

160. Wagenblast E, Soto M, Gutiérrez-Ángel S, Hartl CA, Gable AL, Maceli AR, et al. A model of breast cancer heterogeneity reveals vascular mimicry as a driver of metastasis. Nature. 2015;520:358–62.

161. Dalerba P, Kalisky T, Sahoo D, Rajendran PS, Rothenberg ME, Leyrat A a, et al. Single-

cell dissection of transcriptional heterogeneity in human colon tumors. Nat Biotechnol. Nature Publishing Group; 2011;29:1120–7.

162. Kreso A, O'Brien C a, van Galen P, Gan OI, Notta F, Brown AMK, et al. Variable clonal repopulation dynamics influence chemotherapy response in colorectal cancer. Science. 2013;339:543–8.

163. Dalerba P, Dylla SJ, Park I-K, Liu R, Wang X, Cho RW, et al. Phenotypic characterization of human colorectal cancer stem cells. 2007;104:10158–63.

164. Scheel C, Weinberg RA. Cancer stem cells and epithelial-mesenchymal transition: concepts and molecular links. Semin Cancer Biol. Elsevier Ltd; 2012;22:396–403.

165. Fabrizi E. Therapeutic implications of colon cancer stem cells. World J Gastroenterol. 2010;16:3871.

166. Colak S, Medema JP. Cancer stem cells; important players in tumor therapy resistance. FEBS J. 2014;

167. Dean M, Fojo T, Bates S. Tumour stem cells and drug resistance. Nat Rev Cancer. 2005;5:275–84.

168. Del Vecchio CA, Feng Y, Sokol ES, Tillman EJ, Sanduja S, Reinhardt F, et al. De-differentiation confers multidrug resistance via noncanonical PERK-Nrf2 signaling. PLoS Biol. 2014;12:e1001945.

169. Irish JM, Doxie DB. High-dimensional single-cell cancer biology. Curr Top Microbiol Immunol. 2014;377:1–21.

170. Irish JM, Kotecha N, Nolan GP. Mapping normal and cancer cell signalling networks: towards single-cell proteomics. Nat Rev Cancer. 2006;6:146–55.

171. Abrahamsen I, Lorens JB. Evaluating extracellular matrix influence on adherent cell signaling by cold trypsin phosphorylation-specific flow cytometry. {BMC} Cell Biol. 2013;14:36.

172. Zeng J, Mohammadreza A, Gao W, Merza S, Smith D, Kelbauskas L, et al. A minimally invasive method for retrieving single adherent cells of different types from cultures. Sci Rep. 2014;4:5424.

173. Kokkat TJ, Patel MS, McGarvey D, LiVolsi VA, Baloch ZW. Archived formalin-fixed paraffin-embedded (FFPE) blocks: A valuable underexploited resource for extraction of DNA, RNA, and protein. Biopreserv Biobank. 2013;11:101–6.

174. Li P, Conley A, Zhang H, Kim HL. Whole-Transcriptome profiling of formalin-fixed, paraffin-embedded renal cell carcinoma by RNA-seq. BMC Genomics. 2014;15:1087.

175. Hedegaard J, Thorsen K, Lund MK, Hein A-MK, Hamilton-Dutoit SJ, Vang S, et al. Next-generation sequencing of RNA and DNA isolated from paired fresh-frozen and formalin-fixed paraffin-embedded samples of human cancer and normal tissue. PLoS One. 2014;9:e98187.

176. Lin J-R, Fallahi-Sichani M, Sorger PK. Highly multiplexed imaging of single cells using CycIF, a high-throughput cyclic immunofluorescence method. Cmpct. Nature Publishing Group; 2015;6:1–7.

177. Zrazhevskiy P, Gao X. Quantum dot imaging platform for single-cell molecular profiling. Nat Commun. Nature Publishing Group; 2013;4:1619.

178. Riordan DP, Varma S, West RB, Brown PO. Automated analysis and classification of histological tissue features by multi-dimensional microscopic molecular profiling. PLoS One. 2015;10:1–18.

179. Angelo M, Bendall SC, Finck R, Hale MB, Hitzman C, Borowsky AD, et al. Multiplexed ion beam imaging of human breast tumors. Nat Med. Nature Publishing Group; 2014;20:436–42.

180. Giesen C, Wang HAO, Schapiro D, Zivanovic N, Jacobs A, Hattendorf B, et al. Highly multiplexed imaging of tumor tissues with subcellular resolution by mass cytometry. 2014;11:417–22.

181. Schüffler PJ, Schapiro D, Giesen C, Wang HAO, Bodenmiller B, Buhmann JM. Automatic single cell segmentation on highly multiplexed tissue images. Cytometry A. 2015;87:936–42.

182. Corver WE, ter Haar NT. High-resolution multiparameter {DNA} flow cytometry for the detection and sorting of tumor and stromal subpopulations from paraffin-embedded tissues. Curr Protoc Cytom. 2011;Chapter 7:Unit 7.37.

183. Lau KS, Cortez-Retamozo V, Philips SR, Pittet MJ, Lauffenburger DA, Haigis KM. Multi-scale in vivo systems analysis reveals the influence of immune cells on TNF-α-induced apoptosis in the intestinal epithelium. PLoS Biol. 2012;10:e1001393.

184. Lau KS, Juchheim AM, Cavaliere KR, Philips SR, Lauffenburger DA, Haigis KM. In vivo systems analysis identifies spatial and temporal aspects of the modulation of TNF-α-induced apoptosis and proliferation by MAPKs. Sci Signal. 2011;4:ra16.

185. Pinhel IF, Macneill FA, Hills MJ, Salter J, Detre S, A'hern R, et al. Extreme loss of immunoreactive p-Akt and p-Erk1/2 during routine fixation of primary breast cancer. Breast Cancer Res. 2010;12:R76.

186. Lau KS, Schrier SB, Gierut J, Lyons J, Lauffenburger DA, Haigis KM. Network analysis of differential Ras isoform mutation effects on intestinal epithelial responses to {TNF-α}. Integr Biol [Internet]. 2013;5:1355–65. Available from: http://xlink.rsc.org/?DOI=c3ib40062j

187. Lau KS, Haigis KM. Non-redundancy within the RAS oncogene family: insights into mutational disparities in cancer. Mol Cells. 2009;28:315–20.

188. Haigis KM, Kendall KR, Wang Y, Cheung A, Haigis MC, Glickman JN, et al. Differential effects of oncogenic K-Ras and N-Ras on proliferation, differentiation and tumor progression in the colon. Nat Genet. 2008;40:600–8.

189. Wang Y, Velho S, Vakiani E, Peng S, Bass AJ, Chu GC, et al. Mutant N-RAS protects colorectal cancer cells from stress-induced apoptosis and contributes to cancer development and progression. Cancer Discov. 2013;3:294–307.

190. Feng Y, Bommer GT, Zhao J, Green M, Sands E, Zhai Y, et al. Mutant kras promotes hyperplasia and alters differentiation in the colon epithelium but does not expand the presumptive stem cell pool. Gastroenterology. Elsevier Inc.; 2011;141:1003-1013.e10.

191. Cagnol S, Rivard N. Oncogenic KRAS and BRAF activation of the MEK/ERK signaling pathway promotes expression of dual-specificity phosphatase 4 (DUSP4/MKP2) resulting in nuclear ERK1/2 inhibition. Oncogene. 2013;32:564–76.

192. Galili T. dendextend: an R package for visualizing, adjusting and comparing trees of hierarchical clustering. Bioinformatics. 2015;31:3718–20.

193. Baker FB. Stability of Two Hierarchical Grouping Techniques Case 1: Sensitivity to Data Errors. J Am Stat Assoc. 1974;69:440–5.

194. Zhang B, Wang J, Wang X, Zhu J, Liu Q, Shi Z, et al. Proteogenomic characterization of human colon and rectal cancer. 2014;513:382–7.

195. Xie R, Chung J-Y, Ylaya K, Williams RL, Guerrero N, Nakatsuka N, et al. Factors influencing the degradation of archival formalin-fixed paraffin-embedded tissue sections. J Histochem Cytochem. 2011;59:356–65.

196. Bruggner R V, Bodenmiller B, Dill DL, Tibshirani RJ, Nolan GP. Automated identification of stratifying signatures in cellular subpopulations. 2014;111:E2770–7.

197. Macosko EZ, Basu A, Satija R, Nemesh J, Shekhar K, Goldman M, et al. Highly Parallel Genome-wide Expression Profiling of Individual Cells Using Nanoliter Droplets. Cell [Internet]. Cell Press; 2015 [cited 2018 Mar 7];161:1202–14. Available from: https://www.sciencedirect.com/science/article/pii/S0092867415005498?via%3Dihub

198. Ciaccio MF, Wagner JP, Chuu C-P, Lauffenburger D a, Jones RB. Systems analysis of EGF receptor signaling dynamics with microwestern arrays. Nat Methods. Nature Publishing Group; 2010;7:148–55.

199. Rimm DL, Camp RL, Charette LA, Olsen DA, Provost E. Amplification of tissue by construction of tissue microarrays. Exp Mol Pathol. 2001;70:255–64.

200. Sato T, van Es JH, Snippert HJ, Stange DE, Vries RG, van den Born M, et al. Paneth cells constitute the niche for Lgr5 stem cells in intestinal crypts. Nature [Internet]. Nature Publishing Group; 2010;469:415–8. Available from: http://dx.doi.org/10.1038/nature09637

201. Heuberger J, Kosel F, Qi J, Grossmann KS, Rajewsky K, Birchmeier W. Shp2/MAPK signaling controls goblet/paneth cell fate decisions in the intestine. Proc Natl Acad Sci. 2014;111:3472–7.

202. de Jong PR, Taniguchi K, Harris AR, Bertin S, Takahashi N, Duong J, et al. ERK5 signalling rescues intestinal epithelial turnover and tumour cell proliferation upon ERK1/2 abrogation. Nat Commun. Nature Publishing Group; 2016;7:11551.

203. Kalluri R, Weinberg RA. Review series The basics of epithelial-mesenchymal transition. 2009;119.

204. Vogelstein B, Fearon ER, Hamilton SR, Kern SE, Preisinger AC, Leppert M, et al. Genetic alterations during colorectal-tumor development. 1988;319:525–32.

205. The Cancer Genome Atlas Network. Comprehensive molecular characterization of human colon and rectal cancer. Nature. Nature Publishing Group; 2012;487:330–7.

206. Barras D. BRAF Mutation in Colorectal Cancer: An Update. Biomark Cancer. 2015;7:9–12.

207. Karapetis CS, Khambata-Ford S, Jonker DJ, O'Callaghan CJ, Tu D, Tebbutt NC, et al. K-ras mutations and benefit from cetuximab in advanced colorectal cancer. N Engl J Med. 2008;359:1757–65.

208. Pietrantonio F, Petrelli F, Coinu A, Di Bartolomeo M, Borgonovo K, Maggi C, et al. Predictive role of BRAF mutations in patients with advanced colorectal cancer receiving cetuximab and panitumumab: a meta-analysis. Eur J Cancer. 2015;51:587–94.

209. Friday BB, Adjei AA. Advances in targeting the Ras/Raf/MEK/Erk mitogen-activated protein kinase cascade with MEK inhibitors for cancer therapy. Clin Cancer Res. 2008;14:342–6.

210. Adjei AA, Cohen RB, Franklin W, Morris C, Wilson D, Molina JR, et al. Phase I pharmacokinetic and pharmacodynamic study of the oral, small-molecule mitogen-activated protein kinase kinase 1/2 inhibitor AZD6244 (ARRY-142886) in patients with advanced cancers. J Clin Oncol. 2008;26:2139–46.

211. Sun C, Hobor S, Bertotti A, Zecchin D, Huang S, Galimi F, et al. Intrinsic resistance to MEK inhibition in KRAS mutant lung and colon cancer through transcriptional induction of ERBB3. Cell Rep. 2014;7:86–93.

212. Corcoran RB, Dias-Santagata D, Bergethon K, Iafrate AJ, Settleman J, Engelman JA. BRAF gene amplification can promote acquired resistance to MEK inhibitors in cancer cells harboring the BRAF V600E mutation. Sci Signal. 2010;3:ra84.

213. Pratilas CA, Taylor BS, Ye Q, Viale A, Sander C, Solit DB, et al. (V600E)BRAF is associated with disabled feedback inhibition of RAF-MEK signaling and elevated transcriptional output of the pathway. Proc Natl Acad Sci U S A. 2009;106:4519–24.

214. Yeh JJ, Routh ED, Rubinas T, Peacock J, Martin TD, Shen XJ, et al. KRAS/BRAF

mutation status and ERK1/2 activation as biomarkers for MEK1/2 inhibitor therapy in colorectal cancer. Mol Cancer Ther. 2009;8:834–43.

215. Sahin IH, Kazmi SMA, Yorio JT, Bhadkamkar NA, Kee BK, Garrett CR. Rare Though Not Mutually Exclusive: A Report of Three Cases of Concomitant KRAS and BRAF Mutation and a Review of the Literature. J Cancer. 2013;4:320–2.

216. Weisenberger DJ, Siegmund KD, Campan M, Young J, Long TI, Faasse MA, et al. CpG island methylator phenotype underlies sporadic microsatellite instability and is tightly associated with BRAF mutation in colorectal cancer. Nat Genet. 2006;38:787–93.

217. Morkel M, Riemer P, Bläker H, Sers C, Markus Morkel PRHBCS. Similar but different: distinct roles for KRAS and BRAF oncogenes in colorectal cancer development and therapy resistance. Oncotarget. 2015;6:20785–800.

218. French AJ, Sargent DJ, Burgart LJ, Foster NR, Kabat BF, Goldberg R, et al. Prognostic significance of defective mismatch repair and BRAF V600E in patients with colon cancer. Clin Cancer Res. 2008;14:3408–15.

219. Lochhead P, Kuchiba A, Imamura Y, Liao X, Yamauchi M, Nishihara R, et al. Microsatellite instability and BRAF mutation testing in colorectal cancer prognostication. J Natl Cancer Inst. 2013;105:1151–6.

220. Fransén K, Klintenäs M, Osterström A, Dimberg J, Monstein H-J, Söderkvist P. Mutation analysis of the BRAF, ARAF and RAF-1 genes in human colorectal adenocarcinomas. Carcinogenesis. 2004;25:527–33.

221. Xiao Y, Freeman GJ. The Microsatellite Instable Subset of Colorectal Cancer Is a Particularly Good Candidate for Checkpoint Blockade Immunotherapy. Cancer Discov [Internet]. 2015;5:16–8. Available from: http://cancerdiscovery.aacrjournals.org/cgi/doi/10.1158/2159-8290.CD-14-1397

222. Tran B, Kopetz S, Tie J, Gibbs P, Jiang Z-Q, Lieu CH, et al. Impact of BRAF mutation and microsatellite instability on the pattern of metastatic spread and prognosis in metastatic colorectal cancer. Cancer. 2011;117:4623–32.

223. Kim JH, Rhee Y-Y, Bae JM, Cho N-Y, Kang GH. Loss of CDX2/CK20 expression is associated with poorly differentiated carcinoma, the CpG island methylator phenotype, and adverse prognosis in microsatellite-unstable colorectal cancer. Am J Surg Pathol. 2013;37:1532–41.

224. Nicholas KJ, Greenplate AR, Flaherty DK, Matlock BK, Juan JS, Smith RM, et al. Multiparameter analysis of stimulated human peripheral blood mononuclear cells: A comparison of mass and fluorescence cytometry. Cytometry A. 2016;89:271–80.

225. Leelatian N, Diggins KE, Irish JM. Characterizing Phenotypes and Signaling Networks of Single Human Cells by Mass Cytometry. springerlink; 2015.

226. Amir E, Davis KL, Tadmor MD, Simonds EF, Levine JH, Bendall SC, et al. {viSNE}

enables visualization of high dimensional single-cell data and reveals phenotypic heterogeneity of leukemia. 2013;31:545–52.

227. Diggins KE, Ferrell PB, Irish JM. Methods for discovery and characterization of cell subsets in high dimensional mass cytometry data. Methods. Elsevier Inc.; 2015;82:55–63.

228. Saeys Y, Gassen S, Lambrecht BN. Computational flow cytometry: helping to make sense of high-dimensional immunology data. 2016;16:449–62.

229. Shukla S, Meeran SM. Epigenetics of cancer stem cells: Pathways and therapeutics. Biochim Biophys Acta [Internet]. Elsevier B.V.; 2014;1840:3494–502. Available from: http://www.ncbi.nlm.nih.gov/pubmed/25240776

230. de Sousa e Melo F, Kurtova A V, Harnoss JM, Kljavin N, Hoeck JD, Hung J, et al. A distinct role for Lgr5(+) stem cells in primary and metastatic colon cancer. Nature. 2017;543:676–80.

231. Singh A, Settleman J. {EMT,} cancer stem cells and drug resistance: an emerging axis of evil in the war on cancer. Oncogene. 2010;29:4741–51.

232. Simmons AJ, Lau KS. Deciphering tumor heterogeneity from {FFPE} tissues: Its promise and challenges. Mol Cell Oncol. 2017;4:e1260191.

233. Bendall SC, Davis KL, Amir E-AAD l-A, Tadmor MD, Simonds EF, Chen TJ, et al. Single-cell trajectory detection uncovers progression and regulatory coordination in human B cell development. Cell [Internet]. Elsevier; 2014;157:714–25. Available from: http://dx.doi.org/10.1016/j.cell.2014.04.005

234. Kokkat TJ, Patel MS, Diane M, A LV, Baloch ZW. Archived formalin-fixed paraffin-embedded {(FFPE)} blocks: A valuable underexploited resource for extraction of {DNA,} {RNA,} and protein. Biopreserv Biobank. 2013;11:101–6.

235. Finck R, Simonds EF, Jager A, Krishnaswamy S, Sachs K, Fantl W, et al. Normalization of mass cytometry data with bead standards. Cytom Part A. 2013;

236. Koley D, Bard AJ. Triton X-100 concentration effects on membrane permeability of a single {HeLa} cell by scanning electrochemical microscopy {(SECM)}. Proc Natl Acad Sci. 2010;107:16783–7.

237. Glinka A, Dolde C, Kirsch N, Huang Y, Kazanskaya O, Ingelfinger D, et al. {LGR4} and {LGR5} are R-spondin receptors mediating Wnt/β-catenin and {Wnt/PCP} signalling. 2011;12:1055–61.

238. Hoadley KA, Yau C, Wolf DM, Cherniack AD, Tamborero D, Ng S, et al. Multiplatform Analysis of 12 Cancer Types Reveals Molecular Classification within and across Tissues of Origin. Cell. 2014;158:929–44.

239. Guinney J, Dienstmann R, Wang X, de Reyniès A, Schlicker A, Soneson C, et al. The

consensus molecular subtypes of colorectal cancer. Nat Med. 2015;21:1350–6.

240. Powell AE, Wang Y, Li Y, Poulin EJ, Means AL, Washington MK, et al. The pan-ErbB negative regulator lrig1 is an intestinal stem cell marker that functions as a tumor suppressor. Cell [Internet]. Elsevier Inc.; 2012;149:146–58. Available from: http://dx.doi.org/10.1016/j.cell.2012.02.042

241. Barker N, Ridgway RA, van Es JH, van de Wetering M, Begthel H, van den Born M, et al. Crypt stem cells as the cells-of-origin of intestinal cancer. Nature. 2009;457:608–11.

242. Vermeulen L, Morrissey E, Heijden M van der, Nicholson AM, Sottoriva A, Buczacki S, et al. Defining stem cell dynamics in models of intestinal tumor initiation. Science (80-). 2013;342:995–8.

243. van Es JH, Sato T, van de Wetering M, Lyubimova A, Nee A, Gregorieff A, et al. Dll1+ secretory progenitor cells revert to stem cells upon crypt damage. Nat Cell Biol. 2012;14:1099–104.

244. Yan KS, Gevaert O, Zheng GXY, Anchang B, Probert CS, Larkin KA, et al. Intestinal Enteroendocrine Lineage Cells Possess Homeostatic and Injury-Inducible Stem Cell Activity. Cell Stem Cell. 2017;21:78--90.e6.

245. Shih I-MM, Wang T-LL, Traverso G, Romans K, Hamilton SR, Ben-Sasson S, et al. Top-down morphogenesis of colorectal tumors. Proc Natl Acad Sci. 2001;98:2640–5.

246. Lightman SM, Utley A, Lee KP. Survival of Long-Lived Plasma Cells (LLPC): Piecing Together the Puzzle. Front Immunol. 2019;10:965.

247. Capoccia BJ, Lennerz JKM, Bredemeyer AJ, Klco JM, Frater JL, Mills JC. Transcription factor MIST1 in terminal differentiation of mouse and human plasma cells. Physiol Genomics [Internet]. 2010 [cited 2018 Mar 12];43:174–86. Available from: http://www.physiology.org/doi/10.1152/physiolgenomics.00084.2010

248. Liu J, Willet SG, Bankaitis ED, Xu Y, Wright CVE, Gu G. Non-parallel recombination limits Cre-LoxP-based reporters as precise indicators of conditional genetic manipulation. Genesis. 2013;51:436–42.

249. Álvarez-Aznar A, Martínez-Corral I, Daubel N, Betsholtz C, Mäkinen T, Gaengel K. Tamoxifen-independent recombination of reporter genes limits lineage tracing and mosaic analysis using CreERT2 lines. Transgenic Res. 2019;29:53–68.

250. Vooijs M, Jonkers J, Berns A. A highly efficient ligand-regulated Cre recombinase mouse line shows that LoxP recombination is position dependent. EMBO Rep. 2001;2:292–7.

251. Lo H-YG, Jin RU, Sibbel G, Liu D, Karki A, Joens MS, et al. A single transcription factor is sufficient to induce and maintain secretory cell architecture. Genes Dev. 2017;31:154–71.

252. Johnson CL, Kowalik AS, Rajakumar N, Pin CL. Mist1 is necessary for the establishment of granule organization in serous exocrine cells of the gastrointestinal tract. Mech Dev.

2004;121:261–72.

253. Dekaney CM, King S, Sheahan B, Cortes J. Mist1 Expression is Required for Paneth Cell Maturation. Cell Mol Gastroenterol Hepatol. 2019;

254. Hrvatin S, Deng F, O'Donnell CW, Gifford DK, Melton DA. MARIS: Method for Analyzing RNA following Intracellular Sorting. PLoS One. 2014;9:e89459.

255. Moll R, Schiller DL, Franke WW. Identification of protein IT of the intestinal cytoskeleton as a novel type I cytokeratin with unusual properties and expression patterns. J Cell Biol. 1990;111:567–80.

256. Eliot M, Sui Y, Yousef A-K, Millis B, Tyska M, Roland J, et al. Optimized multiplex immunofluorescence single-cell analysis reveals tuft cell heterogeneity. Jci Insight. 2017;2:e93487.

257. Gerbe F, Jay P. Intestinal tuft cells: epithelial sentinels linking luminal cues to the immune system. 2016;9:1353–9.

258. Ye DZ, Kaestner KH. Foxa1 and Foxa2 Control the Differentiation of Goblet and Enteroendocrine L- and D-Cells in Mice. Gastroenterology. 2009;137:2052–62.

259. Shroyer NF, Wallis D, Venken KJT, Bellen HJ, Zoghbi HY. Gfi1 functions downstream of Math1 to control intestinal secretory cell subtype allocation and differentiation. Genes Dev. 2005;19:2412–7.

260. Haber AL, Biton M, Rogel N, Herbst RH, Shekhar K, Smillie C, et al. A single-cell survey of the small intestinal epithelium. Nature. 2017;551:333–9.

261. Bansal M, Fenoglio CM, Robboy SJ, King DW. Are metaplasias in colorectal adenomas truly metaplasias? Am J Pathol. 1984;115:253–65.

262. Nihed A, Soumaya M, Atika B, Ilhem BJ, Atef BA, Fehmi H, et al. Paneth cell adenocarcinoma of the colon: A rare entity. Int J Surg Case Rep. 2019;65:313–6.

263. Feng Y, Sentani K, Wiese A, Sands E, Green M, Bommer GT, et al. Sox9 induction, ectopic Paneth cells, and mitotic spindle axis defects in mouse colon adenomatous epithelium arising from conditional biallelic Apc inactivation. Am J Pathol. 2013;183:493–503.

264. van der Flier LG, Clevers H. Stem Cells, {Self-Renewal,} and Differentiation in the Intestinal Epithelium. 2009;71:241–60.

265. Gulati GS, Sikandar SS, Wesche DJ, Manjunath A, Bharadwaj A, Berger MJ, et al. Single-cell transcriptional diversity is a hallmark of developmental potential. Science (80-). 2020;367:405–11.

266. Pearce EL, Shedlock DJ, Shen H. Functional Characterization of MHC Class II-Restricted CD8 + CD4 − and CD8 − CD4 − T Cell Responses to Infection in CD4 −/− Mice. J Immunol. 2004;173:2494–9.

267. Tyznik AJ, Sun JC, Bevan MJ. The CD8 Population in CD4-deficient Mice Is Heavily Contaminated with MHC Class II–restricted T Cells. J Exp Med. 2004;199:559–65.

268. Doyle C, Strominger JL. Interaction between CD4 and class II MHC molecules mediates cell adhesion. Nature. 1987;330:256–9.

269. Gay D, Maddon P, Sekaly R, Talle MA, Godfrey M, Long E, et al. Functional interaction between human T-cell protein CD4 and the major histocompatibility complex HLA-DR antigen. Nature. 1987;328:626–9.

270. Keene J-A, Forman J. Helper activity is required for the in vivo generation of cytotoxic T lymphocytes. J Exp Med. 1982;155:768–82.

271. Bronte V, Brandau S, Chen S-H, Colombo MP, Frey AB, Greten TF, et al. Recommendations for myeloid-derived suppressor cell nomenclature and characterization standards. Nat Commun. 2016;7:12150.

272. Lee H-O, Hong Y, Etlioglu HE, Cho YB, Pomella V, Bosch B Van den, et al. Lineage-dependent gene expression programs influence the immune landscape of colorectal cancer. Nat Genet. 2020;52:594–603.

273. Castello LM, Raineri D, Salmi L, Clemente N, Vaschetto R, Quaglia M, et al. Osteopontin at the Crossroads of Inflammation and Tumor Progression. Mediators Inflamm. 2017;2017:4049098.

274. Wang KX, Denhardt DT. Osteopontin: role in immune regulation and stress responses. Cytokine Growth Factor Rev. 2008;19:333–45.

275. Zhang L, Li Z, Skrzypczynska KM, Fang Q, Zhang W, O'Brien SA, et al. Single-Cell Analyses Inform Mechanisms of Myeloid-Targeted Therapies in Colon Cancer. Cell. 2020;181:442--459.e29.

276. Baitsch D, Bock HH, Engel T, Telgmann R, Müller-Tidow C, Varga G, et al. Apolipoprotein E Induces Antiinflammatory Phenotype in Macrophages. Arterioscler Thromb Vasc Biol. 2011;31:1160–8.

277. Codina A, Renauer PA, Wang G, Chow RD, Park JJ, Ye H, et al. Convergent Identification and Interrogation of Tumor-Intrinsic Factors that Modulate Cancer Immunity In Vivo. Cell Syst. 2019;8:136--151.e7.

278. Alshetaiwi H, Pervolarakis N, McIntyre LL, Ma D, Nguyen Q, Rath JA, et al. Defining the emergence of myeloid-derived suppressor cells in breast cancer using single-cell transcriptomics. Sci Immunol. 2020;5:eaay6017.

279. Lesokhin AM, Hohl TM, Kitano S, Cortez C, Hirschhorn-Cymerman D, Avogadri F, et al. Monocytic CCR2(+) myeloid-derived suppressor cells promote immune escape by limiting activated CD8 T-cell infiltration into the tumor microenvironment. Cancer Res. 2011;72:876–86.

280. Movahedi K, Guilliams M, Bossche J Van den, Bergh R Van den, Gysemans C, Beschin A, et al. Identification of discrete tumor-induced myeloid-derived suppressor cell subpopulations with distinct T cell-suppressive activity. Blood. 2008;111:4233–44.

281. Youn J-I, Nagaraj S, Collazo M, Gabrilovich DI. Subsets of Myeloid-Derived Suppressor Cells in Tumor-Bearing Mice. J Immunol. 2008;181:5791–802.

282. Jiang M, Chen J, Zhang W, Zhang R, Ye Y, Liu P, et al. Interleukin-6 Trans-Signaling Pathway Promotes Immunosuppressive Myeloid-Derived Suppressor Cells via Suppression of Suppressor of Cytokine Signaling 3 in Breast Cancer. Front Immunol. 2017;8:1840.

283. Marigo I, Bosio E, Solito S, Mesa C, Fernandez A, Dolcetti L, et al. Tumor-Induced Tolerance and Immune Suppression Depend on the C/EBPβ Transcription Factor. Immunity. 2010;32:790–802.

284. Nagata DE de A, Chiang EY, Jhunjhunwala S, Caplazi P, Arumugam V, Modrusan Z, et al. Regulation of Tumor-Associated Myeloid Cell Activity by CBP/EP300 Bromodomain Modulation of H3K27 Acetylation. Cell Rep. 2019;27:269--281.e4.

285. Xin H, Zhang C, Herrmann A, Du Y, Figlin R, Yu H. Sunitinib Inhibition of Stat3 Induces Renal Cell Carcinoma Tumor Cell Apoptosis and Reduces Immunosuppressive Cells. Cancer Res. 2009;69:2506–13.

286. Zhu C, Sakuishi K, Xiao S, Sun Z, Zaghouani S, Gu G, et al. An IL-27/NFIL3 signalling axis drives Tim-3 and IL-10 expression and T-cell dysfunction. Nat Commun. 2015;6:6072.

287. Hwang S-M, Sharma G, Verma R, Byun S, Rudra D, Im S-H. Inflammation-induced Id2 promotes plasticity in regulatory T cells. Nat Commun. 2018;9:4736.

288. Fife BT, Pauken KE, Eagar TN, Obu T, Wu J, Tang Q, et al. Interactions between PD-1 and PD-L1 promote tolerance by blocking the TCR-induced stop signal. Nat Immunol. 2009;10:1185–92.

289. Duckworth CA, Clyde D, Worthley DL, Wang TC, Varro A, Pritchard DM. Progastrin-induced secretion of insulin-like growth factor 2 from colonic myofibroblasts stimulates colonic epithelial proliferation in mice. 2013;145:197–208, e3.

290. Ballbach M, Dannert A, Singh A, Siegmund DM, Handgretinger R, Piali L, et al. Expression of checkpoint molecules on myeloid-derived suppressor cells. Immunol Lett. 2017;192:1–6.

291. Wells AD, Walsh MC, Sankaran D, Turka LA. T Cell Effector Function and Anergy Avoidance Are Quantitatively Linked to Cell Division. J Immunol. 2000;165:2432–43.

292. Utting O, Teh S-J, Teh H-S. A Population of In Vivo Anergized T Cells with a Lower Activation Threshold for the Induction of CD25 Exhibit Differential Requirements in Mobilization of Intracellular Calcium and Mitogen-Activated Protein Kinase Activation. J

Immunol. 2000;164:2881–9.

293. Carlin LM, Yanagi K, Verhoef A, Hoen ENMN-'t, Yates J, Gardner L, et al. Secretion of IFN-γ and not IL-2 by anergic human T cells correlates with assembly of an immature immune synapse. Blood. 2005;106:3874–9.

294. Greenwald RJ, Boussiotis VA, Lorsbach RB, Abbas AK, Sharpe AH. CTLA-4 regulates induction of anergy in vivo. Immunity. 2001;

295. Duckworth A, Glenn M, Slupsky JR, Packham G, Kalakonda N. Variable induction of PRDM1 and differentiation in chronic lymphocytic leukemia is associated with anergy. Blood. 2014;123:3277–85.

296. Anderson AC, Joller N, Kuchroo VK. Lag-3, Tim-3, and TIGIT: Co-inhibitory Receptors with Specialized Functions in Immune Regulation. Immunity. 2016;44:989–1004.

297. Yang XO, Pappu BP, Nurieva R, Akimzhanov A, Kang HS, Chung Y, et al. T Helper 17 Lineage Differentiation Is Programmed by Orphan Nuclear Receptors RORα and RORγ. Immunity. 2008;28:29–39.

298. Moon YW, Hajjar J, Hwu P, Naing A. Targeting the indoleamine 2,3-dioxygenase pathway in cancer. J Immunother Cancer. 2015;3:51.

299. Bonneville M, Janeway CA, Ito K, Haser W, Ishida I, Nakanishit N, et al. Intestinal intraepithelial lymphocytes are a distinct set of γδ T cells. Nature. 1988;336:479–81.

300. Schön MP, Arya A, Murphy EA, Adams CM, Strauch UG, Agace WW, et al. Mucosal T lymphocyte numbers are selectively reduced in integrin alpha E (CD103)-deficient mice. J Immunol. 1999;162:6641–9.

301. McDonald BD, Jabri B, Bendelac A. Diverse developmental pathways of intestinal intraepithelial lymphocytes. Nat Rev Immunol. 2018;18:1.

302. Joshi NS, Cui W, Chandele A, Lee HK, Urso DR, Hagman J, et al. Inflammation Directs Memory Precursor and Short-Lived Effector CD8+ T Cell Fates via the Graded Expression of T-bet Transcription Factor. Immunity. 2007;27:281–95.

303. Blackburn SD, Shin H, Haining WN, Zou T, Workman CJ, Polley A, et al. Coregulation of CD8+ T cell exhaustion by multiple inhibitory receptors during chronic viral infection. Nat Immunol. 2008;10:29–37.

304. Yamada T, Park CS, Mamonkin M, Lacorazza HD. Transcription factor ELF4 controls the proliferation and homing of CD8+ T cells via the Krüppel-like factors KLF4 and KLF2. Nat Immunol. 2009;10:618–26.

305. Lukjanenko L, Jung JM, Hegde N, Claire P-C, Migliavacca E, Rozo M, et al. Loss of fibronectin from the aged stem cell niche affects the regenerative capacity of skeletal muscle in mice. 2016;22:897–905.

306. Tetteh PW, Basak O, Farin HF, Wiebrands K, Kretzschmar K, Begthel H, et al.

Replacement of Lost Lgr5-Positive Stem Cells through Plasticity of Their Enterocyte-Lineage Daughters. Cell Stem Cell. 2016;18:203–13.

307. Lister R, Pelizzola M, Kida YS, Hawkins RD, Nery JR, Hon G, et al. Hotspots of aberrant epigenomic reprogramming in human induced pluripotent stem cells. Nature. 2011;

308. Castro F, Cardoso AP, Gonçalves RM, Serre K, Oliveira MJ. Interferon-gamma at the crossroads of tumor immune surveillance or evasion. Front. Immunol. 2018.

309. Wu Y, Xu J, Du C, Wu Y, Xia D, Lv W, et al. The Predictive Value of Tumor Mutation Burden on Efficacy of Immune Checkpoint Inhibitors in Cancers: A Systematic Review and Meta-Analysis. Front. Oncol. 2019.

310. Llosa NJ, Cruise M, Tam A, Wicks EC, Hechenbleikner EM, Taube JM, et al. The Vigorous Immune Microenvironment of Microsatellite Instable Colon Cancer Is Balanced by Multiple {Counter-Inhibitory} Checkpoints. Cancer Discov. 2015;5:43–51.

311. Yamamoto K, Venida A, Yano J, Biancur DE, Kakiuchi M, Gupta S, et al. Autophagy promotes immune evasion of pancreatic cancer by degrading MHC-I. Nature. 2020;

312. Roper J, Tammela T, Cetinbas N, Akkad A, Roghanian A, Rickelt S, et al. In vivo genome editing and organoid transplantation models of colorectal cancer and metastasis. 2017;35:569–76.

313. Maseda D, Banerjee A, Johnson EM, Washington MK, Kim H, Lau KS, et al. mPGES-1-Mediated Production of PGE2 and EP4 Receptor Sensing Regulate T Cell Colonic Inflammation. Front Immunol [Internet]. NLM (Medline); 2018 [cited 2020 Jul 18];9:2954. Available from: https://pubmed.ncbi.nlm.nih.gov/30619314/

314. McKinley ET, Roland JT, Franklin JL, Macedonia MC, Vega PN, Shin S, et al. Machine and deep learning single-cell segmentation and quantification of multi-dimensional tissue images. bioRxiv. 2019.

315. Kotecha N, Krutzik PO, Irish JM. Web-based analysis and publication of flow cytometry experiments [Internet]. Curr. Protoc. Cytom. Curr Protoc Cytom; 2010 [cited 2020 Jul 18]. Available from: https://pubmed.ncbi.nlm.nih.gov/20578106/

316. Klein AM, Mazutis L, Akartuna I, Tallapragada N, Veres A, Li V, et al. Droplet barcoding for single-cell transcriptomics applied to embryonic stem cells. Cell [Internet]. Elsevier Inc.; 2015;161:1187–201. Available from: http://dx.doi.org/10.1016/j.cell.2015.04.044

317. Southard-Smith AN, Simmons AJ, Chen B, Jones AL, Ramirez Solano MA, Vega PN, et al. Dual indexed library design enables compatibility of in-Drop single-cell RNA-sequencing with exAMP chemistry sequencing platforms. BMC Genomics [Internet]. NLM (Medline); 2020 [cited 2020 Jul 18];21:456. Available from: https://pubmed.ncbi.nlm.nih.gov/32616006/

318. Heiser CN, Lau KS. A Quantitative Framework for Evaluating Single-Cell Data Structure Preservation by Dimensionality Reduction Techniques. Cell Rep. Elsevier B.V.;

2020;31:107576.

319. Yissachar N, Zhou Y, Ung L, Lai N, Mohan J, Ehrlicher A, et al. An Intestinal Organ Culture System Uncovers a Role for the Nervous System in {Microbe-Immune} Crosstalk. Cell. 2017;168:1135-1148.e12.

320. Sato T, Vries RG, Snippert HJ, Wetering M van de, Barker N, Stange DE, et al. Single Lgr5 stem cells build crypt–villus structures in vitro without a mesenchymal niche. Nature [Internet]. Macmillan Publishers Limited. All rights reserved; 2009 [cited 2014 Jul 10];459:262. Available from: http://dx.doi.org/10.1038/nature07935

321. Agudo J, Ruzo A, Park ES, Sweeney R, Kana V, Wu M, et al. JEDI T-cells enable targeted cell depletion and investigation of T-cell interactions with virtually any cell population HHS Public Access Author manuscript. Nat Biotechnol. 2015;

322. Shipman L. Tumour immunology: Interrogating intratumoral Tregcells. Nat Rev Immunol [Internet]. Nature Publishing Group; 2017;17:4–5. Available from: http://dx.doi.org/10.1038/nri.2016.137